International Hydrological Programme

Oceanography Basics

-The Textbook for Sixteenth IHP Training Course in 2006-

Edited by Akihiko Morimoto

Hydorospheric Atmospheric Research Center, Nagoya University

United Nations Educational Scientific and Cultural Organization

International Hydrological Programme

Oceanography Basics

-The Textbook for Sixteenth IHP Training Course in 2006-

Edited by Akihiko Morimoto

Hydorospheric Atmospheric Research Center, Nagoya University

United Nations Educational Scientific and Cultural Organization

Prepared for the Sixteenth IHP Training Course on Oceanography Basics, 26 November – 9 December, 2006, Nagoya, Mie and Ehime, Japan

Working Group for IHP Training Course,
Sub-Committee for IHP,

Japan National Commission for UNESCO
Chairperson: Prof. H. Uyeda, Nagoya University

Secretariat:
Mr. K. Akiyama, Ministry of Education, Culture, Sports, Science and Technology
Mr. T. Minami, Ministry of Education, Culture, Sports, Science and Technology
Ms. H. Hino, Ministry of Education, Culture, Sports, Science and Technology
Mr. A. Yamamoto, Nagoya University

Members:
Prof. K. Takeuchi, Yamanashi University
Prof. Y. Fukushima, Research Institute for Humanity and Nature
Mr. M. Kunitomo, Ministry of Land Infrastructure and Transport
Dr. M. Sugi, Japan Meteorological Agency
Dr. K. Nakane, National Research Institute for Earth Science and Disaster Prevention
Dr. N. Horikawa, National Institute for Rural Engineering
Prof. T. Yanagi, Kyushu University
Prof. K. Nakamura, Nagoya University
Prof. K. Tsuboki, Nagoya University
Prof. T. Hiyama, Nagoya University
Prof. A. Morimoto, Nagoya University

Published in 2007 by the Hydrospheric Atmospheric Research Center (HyARC), Nagoya University, and United Nations Educational Scientific and Cultural Organization (UNESCO)

Printed by Nagoya University COOP
ISBN: 978-4-9980619-7-7
Cover: Training vessel Sei-Sui Maru of Mie University

Preface

The general aim of the 16th IHP Training Course is to help participants develop their basic knowledge of oceanography in the solution of current global environmental problems, which are now crucial in many countries. The course is part of UNESCO International Hydrological Programme (IHP) and is held every Japanese fiscal year that starts in April. The participants mainly from Asia-Pacific regions are given a series of lectures and practical trainings for about two weeks. Until 1996, the course was mainly focused on general hydrology and later concentrated on specified themes such as: snow hydrology (1998), remote sensing (1999), limnology (1999), hydrology related to head water management (2000), hydrogen and oxygen isotopes in hydrology (2002), precipitation and water resources (2003), effect of air-pollutants on the atmospheric environments and climate changes (2004) and water and carbon cycles in terrestrial ecosystems (2005).

This year, the Sixteenth IHP Training Course with a theme of "Oceanography Basics" will be held from 26 November to 9 December, 2006 at Nagoya and Ehime with many lectures and practices. This IHP short course will focus on understanding basic knowledge of oceanography relating to global change. A series of lectures would show how the land, oceans, and atmosphere are interacting, how the water and materials cycles are coupled, what the driving forces of materials cycling in the ocean are, and what the causes of its variation are. Participants would acquire new view from this short course that even the local environmental problems relating to hydrological cycle change on a regional scale are resulting from a part of global cycles of water and materials including oceans.

The Sixteenth course will be conducted by contributions from professionals/experts in universities and research institutes led by Prof. Akihiko Morimoto, Prof. Toshiro Saino, Prof. J. Ishizaka, Nagasaki University, Prof T. Takeoka, Prof. A. Kaneda, Ehime University, Prof. Y. Sekine, Mie University, Capt. M. Uchida, Sei-Sui Maru of Mie University, Prof. Y. Tanimoto, Hokkaido University, Prof. T. Suga, Tohoku University, Prof. S. Uye, Hiroshima University, Prof. T. Yanagi, Kyushu University, H. Sugisaki, National Research Institute of Fisheries Science, Prof. Y. Fukushima, Research Institute of Humanity and Nature, Dr. Y. Koizumi, Ehime Prefectural Fisheries Experiment Station, Dr. K. Sasaoka, Japan Agency for Marine-Earth Science and Technology.

The course would not have been possible to conduct without management supports. Dr. Giuseppe Arduino and his staff in UNESCO Jakarta Office worked for the arrangement for the participants. The IHP Training Course is under continuous support from the Ministry of Education, Culture, Sports, Science, and Technology.

20 November, 2006

Hiroshi Uyeda
Chairperson of Working Group for IHP Training Course
Director, Hydrospheric Atmospheric Research Center,
Nagoya University

List of the contributors

Lectures

Chapter 1 Land and Oceans
Y. Fukushima

Chapter 2 Oceans and Atmosphere
Y. Tanimoto

Chapter 3 Ocean Circulation
T. Suga

Chapter 4 Phytoplankton in the Ocean
J. Ishizaka

Chapter 5 Zooplankton in the Ocean
S. Uye

Chapter 6 Material Dynamics in Coastal Seas
A. Morimoto

Chapter 7 Biogeochemical Cycles in the Ocean
T. Saino

Chapter 8 Change in Biogeochemical Cycles in the Ocean
H. Sugisaki

Chapter 9 Role of Coastal Seas in Climate System
T. Yanagi

Practice Sessions

P1 Field Observation in Ise Bay
Y. Sekine and **A. Morimoto**

P2 Analysis of Satellite Ocean Color Data
K. Sasaoka

Technical Tours

T1 Auto-Monitoring System of Water Quality in the Bungo Channel, Ehime University
H. Takeoka and **A. Kaneda**

T2 Aquaculture and Monitoring System in the Bungo Channel, Ehime Prefectural Fisheries Experimental Station
Y. Koizumi

Acknowledgements

I would like to express my sincere thanks to all the authors for their immense contribution to this textbook. It would not have been published without their considerable efforts. Thanks are extended to Prof. Hiroshi Uyeda, the chairperson of the working group of the IHP Training Course and Director of the Hydrospheric Atmospheric Research Center (HyARC), Nagoya University, Japan.

The support from the Japan National Commission for UNESCO, sub-committee of IHP led by Prof. Kuniyoshi Takeuchi from Yamanashi University, and the working group of IHP Training Course is highly acknowledged. Thanks are also extended to Mr. Kazuo Akiyama and Mr. Tetsuhito Minami from the Ministry of Education, Culture, Sports, Science and Technology of Japan, Mr. Akihiro Yamamoto from Nagoya University, Japan for sharing the role of secretariat, and the staff (Prof. Yoshihisa Mino, Ms. Tsuyako Mizuno, Ms. Saori Haga, Ms. Yuko Ozeki, and Ms. Mariko Kayaba) of HyARC, Nagoya University, Japan for their local arrangements and technical editing of this textbook.

28 February, 2007

Akihiko Morimoto
Hydrospheric Atmospheric Research Center,
Nagoya University

Editor

Current address of the contributors (alphabetical order)

Y. Fukushima……Research Institute for Humanity and Nature, Inter-University Research Institute Corporation National Institutes for the Humanities
e-mail: yoshi@chikyu.ac.jp

J. Ishizaka……Faculty of Fisheries, Nagasaki University
e-mail: ishizaka@nagasaki-u.ac.jp

A. Morimoto……Hydrospheric Atmospheric Research Center, Nagoya University
e-mail: amorimoto@hyarc.nagoya-u.ac.jp

T. Saino……Hydrospheric Atmospheric Research Center, Nagoya University
e-mail: tsaino@hyarc.nagoya-u.ac.jp

K. Sasaoka……Frontier Research Center for Global Change, Japan Agency for Marine-Earth Science and Technology
e-mail: sasaoka@jamstec.go.jp

T. Suga……Graduate School of Science, Tohoku University
e-mail: suga@pol.geophys.tohoku.ac.jp

H. Sugisaki……National Research Institute of Fisheries Science, Fisheries Research Agency
e-mail: sugisaki@affrc.go.jp

Y. Tanimoto……Graduate School of Environmental Science, Hokkaido University
e-mail: tanimoto@ees.hokudai.ac.jp

S. Uye……Graduate School of Biosphere Sciences, Hiroshima University
e-mail: suye@hiroshima-u.ac.jp

T. Yanagi……Research Institute for Applied Mechanics, Kyushu University
e-mail: tyanagi@riam.kyushu-u.ac.jp

Contents

Part I

Textbook

Chapter 1

The Role of Forest on Hydrology of Headwaters

Yoshihiro Fukushima
Research Institute for Humanity and Nature(RIHN)
Inter-University Research Institute Corporation National Institutes for the Humanities
457-4 Motoyama Kamigamo, Kyoto 603-8047, JAPAN
e-mail:yoshi@chikyu.ac.jp

1.1 Introduction

Whether a headwater area is wet or dry is determined by the climatic condition between precipitation and evaporation. Potential evaporation means evaporation from shallow open water or wet grassland without trees. Generally, the factors controlling evaporation are energy balance, air temperature, water vapor, wind velocity and the physiology of the vegetation. Its amount corresponds to the value that the resistance of the land surface is zero by Penman-Monteith's equation shown in Section 1.5 since energy balance and air temperature have a tendency to decrease more in the regions of high rather than low latitude.

In Japan, the most headwater wetlands are located at the rather high altitudes in mountainous areas. A special feature of wetlands in Japan is their abundance of rare species of grasses, insects and animals. Migratory birds are sometimes seen in remote areas far from human habitation. Some of these areas are now endangered due to the invasion of humans who find them readily adaptable to be changed to agricultural use by reclamation and drainage. In this chapter, the hydrological role of headwater is examined by a comparison between forested and devastated headwaters.

1.2 Sediment yield

1.2.1 General remarks

Headwaters are thought to be important and essential areas for providing a safe and stable water supply not only for irrigation but also as a source of drinking water for people living downstream. Recently, we have discovered that such areas have the additional value of maintaining the diversity of the biosphere, a value of which the public is becoming increasingly aware. Developed countries

paid no attention to the value of headwaters until the end of the 18th century, and developing countries are only now beginning to understand the significance. However, the rapid growth in human population and the pressure to increase food production have made the situation difficult. Nevertheless, the environment of headwaters has to be maintained by natural vegetation survived for long time on eco-hydrological aspect.

1.2.2 Sediment yield in a devastated headwater area

Lake Biwa, located in central Japan, is the country's largest lake with an area of 670km^2. To its south lies Mount Tanakami, which in 19th century, this area was devastated by thoughtless exploitation as a supply area for wood, fuel and fertilizer provided by forests close to villages. Adding to the devastation is the fact that Mount Tanakami is underlain by weathered granite and its soil easily disturbed due to its rather small and loose particles. As a great volume of sediment was transported downstream, disasters due to flood and sediment deposits devastated downstream villages. Since the early of 20th century, headwater conservation works have been undertaken in the source area of large rivers with major cities downstream. Since the river water from Lake Biwa flows down to the cities of Osaka, Kyoto and Kobe, Mount Tanakami became the logical site for conservation projects, which are generally of two kinds. One is hillslope conservation aimed at fixation of the soil by reforestation mainly with pine tree species mixed with other plant species able to fix air nitrogen in the soil as fertilizer. The other is constructing check-dams on a river bed in order to prevent scoring of the riverbed. To evaluate such conservation projects, various investigations and observations were carried out in Mount Tanakami.

1.2.3 Formation system of sediment production and transportation

Generally, sediment yield has been observed by

1) peg method on slopes
2) trap method on slopes and in the source area

Figure 1.1 clearly shows that annual sediment yields on bare slopes are roughly in the range of 5,000 to10,000 $m^3km^{-1}yr^{-1}$ regardless of the method used, and that the sediment yields on reforested slopes are about 10 $m^3km^{-1}yr^{-1}$, a volume equals to two to three orders less than that on bare slopes. Furthermore, sediment yields of headwaters when enough time has elapsed after reforestation range from 5.0 to 0.1 $m^3km^{-1}yr^{-1}$, which is equal to one to two orders less than that on reforested slopes. The stabilization of the riverbed by the construction of check-dams seemed to have been effective in bringing about this change.

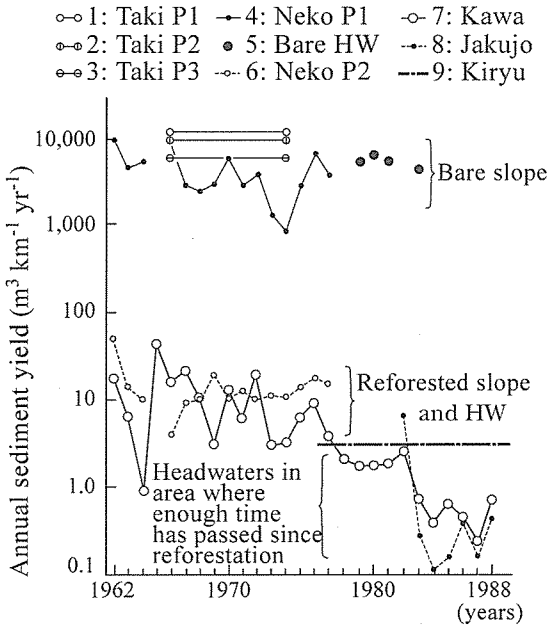

Figure 1.1 Annual change of sediment yields between bare and reforested area observed by the different methods in Mount Tanakami, where is underlain by granite and located in central Japan (Suzuki and Fukushima, 1989)

Why have such big differences in sediment yields occurred among the variation of land-cover? Individual investigations and observations of the erosion processes confirmed that movable soil material was produced on bare slopes by weathering and frost action, and that those materials were transported downstream by the tractive force on hydraulics in each flood event (Seno *et al.*, 1981: Takei *et al.*, 1981).

Figure 1.2 shows an example of a flood event with two very heavy rainfalls (exceeding 10mm/10min a day) at adjacent plots, one with bare and the other with reforested slopes at Neko, established in Mount Tanakami. The hydrograph at the bare plot registered peak-flows of over 40 mm/hr during rainfalls, whereas the hydrograph at the reforested plot showed a peak-flow of only 1mm/hr during both. This confirms that the reforestation caused a peak-flow decrease of a fortieth. This remarkable decrease is plotted in Figure 1.2

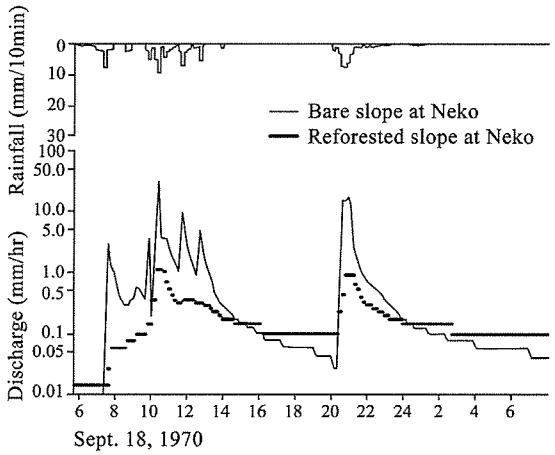

Figure 1.2 Comparison of the flood hydrograph measurements at both the bare and reforested plots at Neko, Mount Tanakami, Japan (Takei *et al.*, 1981)

Now we can recognize that sediment yield has close relationship with flood discharge. Quantitatively, which relationship provides an adequate explanation? Mayer-Peter and Müller(1948) developed sediment hydraulics with the aim of applying it to mountain torrents. Their equation is written as follows:

$$\frac{q_b}{\sqrt{(\delta/\rho-1)gd^3}} = 8\left[\frac{U_*^{\,2}}{(\delta/\rho-1)gd}k-\Psi_c\right]^{3/2} \tag{1.1}$$

where q_b is the bed-load rate in volume per unit time and unit width, δ and ρ are the specific weights of sand and water, respectively, g is the gravitational constant, d is the mean diameter of the bed-load materials, U_* is the shear velocity [$=(gHS)^{1/2}$], H is the depth of water, S is the channel slope, k is the ratio of effective energy, and Ψ_c is the critical tractive force (Ψ_c=0.047).

On the other hand, the regime theory of a river system on geomorphology between the flow rate, Q(m^3/sec), and the width of a cross section of river, B (m), has been estimated by investigations as follows:

$$B = \alpha\sqrt{Q} \tag{1.2}$$

where α is a parameter. Manning's roughness, n, is assumed to be n=0.02 by the particle diameter of bed-load materials and the α value is assumed to be 0.4.

Finally, the relationships between the river discharge and the sediment concentrations on the slopes and in the torrents of Mount Tanakami are displayed in Figure 1.3, which shows that the amount of sediment transport is basically controlled by the flow rate and slope angle in both riverbeds and slopes with the same particle size. Whether a riverbed is scoured or deposited is determined by this relationship. It is particularly important to recognize that the angle of a slope or riverbed, S=0.4, shows a high sediment concentration (almost five percent) when the flow rate

exceeds $10^{-3}m^3$/sec.

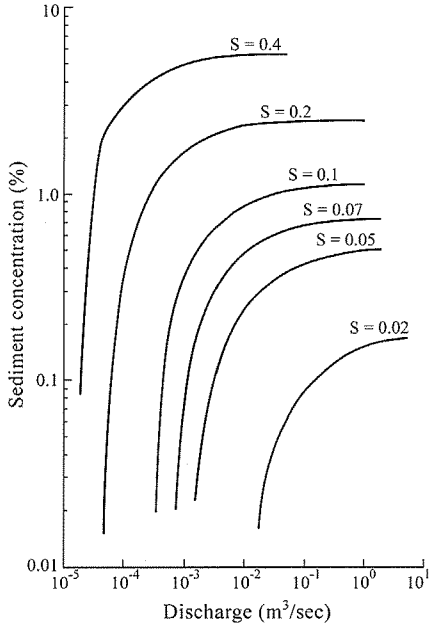

Figure 1.3 Relationships between river discharge and sediment concentrations in Mount Tanakami (*S*: angle) (Seno *et al.* 1981)

1.3 Flood flow and forest cover

1.3.1 Separation of flood runoff

Though sediment transport was verified to be controlled by flood runoff in Section 1.2.3, it is necessary to determine that what kinds of factors affect the formation of flood runoff.

Basically, rainfall impacting a headwaters area becomes either infiltrated water or surface flow. The infiltration rate is generally low on a bare surface and high on a land surface covered by vegetation. Some of the infiltrated water turns into a sub-surface flow along A and A_0 layers of the soil. Deeply percolated water reaches the bottom layer of soil which is in contact with the bedrock surface. Such water usually flows down to an open-channel along the slope as ground water flow. Though some of the ground water percolates vertically along seams in the rock, the amount is usually negligible in mountainous areas composed of old sedimentary rock such as the Paleozoic type except of limestone and plutonic rocks such as granite. The entire headwater area can be categorized into two systems, i.e., a slope system and an open-channel system. Both surface and sub-surface flows in a slope system are known as direct runoff or quick flow, while the runoff component is an open-channel system is known as base flow or delayed flow.

Flood runoff is defined as the component of the upper region separated by a straight line from the rising point to the arrival point, and displays the same constant recession curve on a hydrograph in

each headwater basin. Although Hewlett and Hibbert (1967) have proposed a separation method by which the base flow is thought to increase at a constant ratio from the rising point on a hydrograph by statistical analysis, their method is not commonly accepted among headwater hydrologists. Though the separation method seems simple if samples are gathered from comparatively large floods with a single peak, it poses a more difficult task in any flood event involving weak rainfall intensity or double peaks. Nevertheless, the separation of the direct runoff component seems possible if many flood events are examined. In order to accurately interpret flood hydrographs, the effective rainfall intensity should be defined. To accomplish this, two basic ideas have been proposed. One is Horton's infiltration theory (Horton,1933, 1939) and the other is the concept of a variable source area (Dunne *et al.*, 1975). The author, not wishing to become involved in the ongoing controversy it in this section, has suggested the possibility of estimating the effective rainfall intensity from the relationships between the cumulative rainfall amount and the estimated direct runoff shown in Figure 1.4, where the dotted line shows an example of a typical separation. The ratio of the direct runoff component clearly seems to increase with the rainfall amount.

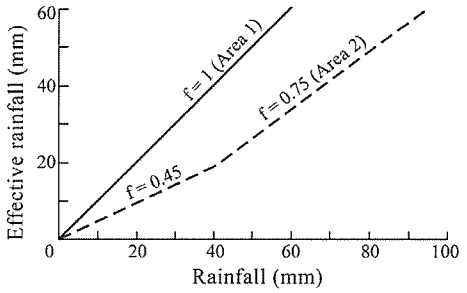

Figure 1.4 Relationship between rainfall amount and effective rainfall (=direct runoff) (Fukushima, 1981)

1.3.2 Formation system of hydrographs in headwater areas

Most flood hydrographs seem to change in their shape according to the basin scale, slope, and torrent gradient except for differences in forest cover. By using the kinematic wave method, the topographical differences of all headwaters might be explained by the differences between the slope length and its gradient and channel length and its gradient, as shown in Figure 1.5

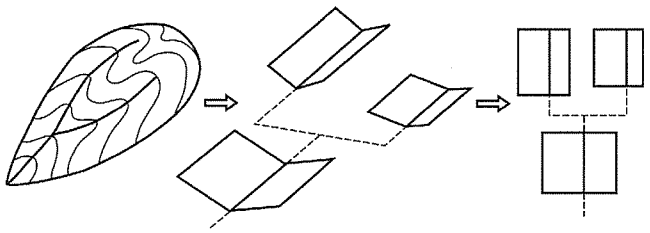

Figure 1.5 Topographical modeling based on the kinematic wave method (Fukushima, 1981)

How can we generally recognize the differences of the hydrograph in both bare and reforested slopes shown in Figure 1.2 The parallel-slopes model developed by Fukushima (1981) shown in Figure 1.6 attempts to do that by defining all slopes as composed of two types. One is an impermeable slope without soil, and the other is a permeable slope with forest soil. The first is designated as Area 1 and the second as Area 2. As the ratio of Area 1 is defined as *C*, the ratio of Area 2 is *1-C* in the entire headwater area shown in Figure 1.6 The vertical axis in Figure 1.4 shows direct runoff that is now assumed to be a traces of effective rainfall in time series, and the difference in basin scale can be explained by the difference between the channel length and its gradient as shown for example in Figure 1.7

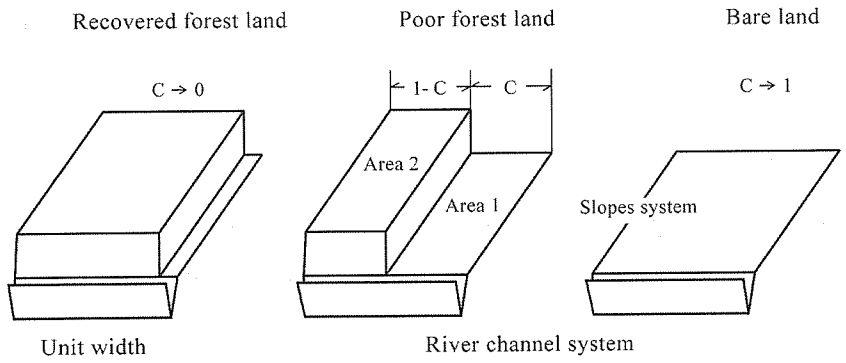

Figure 1.6 The schema of the parallel-slopes model developed by Y.Fukushima (1981)

This proposed model is based on the fact that a recovered forest is rich in forest soil whereas a devastated mountain is practically devoid of it. Such differences will emerge first in the relationships between the rainfall amount and direct runoff shown in Figure 1.4, and secondly in the rapidity of rainwater movement, as expressed by the following equations:

On a slope system,

$$\frac{\partial h_1}{\partial t} + \frac{\partial q_1}{\partial x} = \omega r_{e1} \qquad (1.3)$$

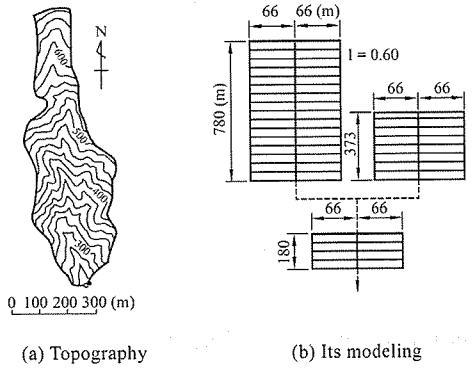

(a) Topography (b) Its modeling

Figure 1.7 An example of topographical modeling (Fukushima, 1981)

where h_1 is the depth of water, q_1 is the discharge rate in unit width, t and x are time and distance, ω is a constant of unit exchange, and r_{e1} is the effective rainfall intensity in Area 1 with the ratio of C.

$$\frac{\partial h_2}{\partial t} + \frac{\partial q_2}{\partial x} = \omega r_{e2} \tag{1.4}$$

where h_2 is the depth of water, q_2 is the discharge rate in unit width, and r_{e2} is the effective rainfall intensity in Area 2 with the ratio of 1-C.

The motion between h and q using the kinematic wave method is as follows:

$$h = kq^p \tag{1.5}$$

where k and p are the respective parameters.

If water flow in the slope system is approximated as surface flow, the following relationship can be applied to Equation (1.5) by Manning's law.

$$k = \left(\frac{N}{\sqrt{I}}\right)^p, p = \frac{3}{5} \tag{1.6}$$

where N is the equivalent roughness of Manning, and I is the slope gradient ($sin\theta$).

If water flows through the soil particles in forest soil, Darcy's law can be applied as follows:

$$k = \left(\frac{\gamma}{MI}\right), p = 1 \tag{1.7}$$

where γ is the porosity of forest soil, and M is the permeability of Darcy's law.

In the channel system,

$$\frac{\partial A}{\partial t} + \frac{\partial Q}{\partial x} = Cq_1 + (1-C)q_2 \tag{1.8}$$

where A is the cross profile of a channel section, and Q is the river discharge.

$$A = Kq^P \tag{1.9}$$

where K and P are the respective parameters.

$$R = K_1 A^Z \tag{1.10}$$

where R is the channel radius, and K_1 and Z are respectively parameters.

Finally, the following equation is assumed to present Manning's law.

$$K = \left(\frac{n}{K_1^{2/3} I^{1/2}}\right)^P, P = \frac{3}{2Z+3} \tag{1.11}$$

where n is Manning's roughness.

After the parallel-slopes model was applied to many flood events occurring in headwater basins, the parameters controlling the motion of water flow were determined. In a channel system, the following parameters were determined suitable by field measurements and the model's fittings.

Table 1.1 Parameters controlling channel flow

Basin name	P	K
Kiryu main	0.77	3.0
Kiryu sub2	0.77	3.0
Jakujo	0.77	3.0
Yayoi	0.77	2.0
Kawa main	0.7	1.0
Hachi	0.7	1.0

The areas of headwater basins used for the validation of the parameters controlling channel flow are in the range of 0.05 to 0.5 km^2 underlain by granite and Paleozoic rock. Parameters controlling water flow in a slope system are plotted in Figure 1.8 with the relationship between the slope angle and its equivalent roughness, K_2, in Area 2.

In the same time, it became evident the degree of K_1 in Area 1 was almost 0.1 times that of K_2. It was also established that the C value is useful for a prospective evaluation of the condition of forest coverage.

In Figure 1.8, the data on the Whitehall headwater was personally provided by Professor Hewlett. This headwater has become well known for its role in explaining the concept of a variable source area by Choley (1978) and was originally studied by Tishendolf (1969). The reason why the author used it for validation is that it has gentler slopes than those of the Japanese headwaters previously observed. In any event, it is very important that the equivalent roughness in a forested slope can be explained as being in the value range of 5-10$m^{-1/3}$sec, in spite of any difference in the slope incline.

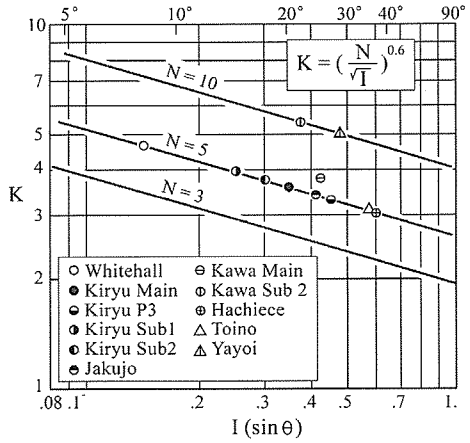

Figure 1.8 Relationship between slope angle, I, in Area 2 and equivalent roughness, K_2

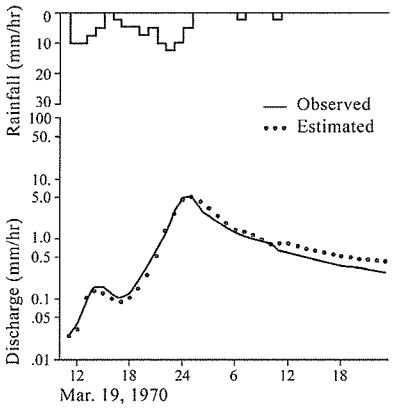

Figure 1.9 Example of an estimated hydrograph in Whitehall headwater

1.4 Forest coverage and water yield

1.4.1 Effects of forest coverage on water yield

Since early in the 19th century, experimental studies in many countries have used the paired watershed method for clarifying the effects of forest coverage on water yield. It was Bosch and Hewlett (1982) who finally completed a synthesis of the results reported by many research groups. They showed that the annual increase in the water yield in a headwater area is proportional to the level of forest destruction and that the increase in water yield is highest in over-exploitative evergreen coniferous forests, followed by that in deciduous broad-leaved and bush forests. This tendency persists in spite of the differences in rainfall amounts. Moreover, it is an unknown issue whether annual water yields change or not with the regeneration of forest. Using long-term experimental results, Swift and Swank (1981) have shown that the water yield was much higher just after clear-cutting, and that it gradually declined in the controlled headwater area of the Coweeta Experimental Station in the United States. In the course of two clear-cuttings, the same tendency persisted. As an example of the effect of reforestation on water yield, Schulze and George (1987) have analyzed observed data from South Africa, and concluded that the annual evaporation amount quickly increases just after reforestation when compacted to a grassy-area used as a control and that the rate of that increase seems to peak after 10-20 years of reforestation. I interpret this to mean that the peak seems to correspond with the volume of leaves that have reached saturation. Thus, such experiments assume the water budget in a basin scale shown as follows:

$$P = Q + E + \Delta S \tag{1.12}$$

where P is precipitation, Q is runoff, E is evaporation, and ΔS is the difference in water storage.

If the period for the analysis is taken as one year, ΔS is negligible. Therefore, it now becomes easy to understand that an increase in runoff corresponds to an equivalent decrease in the evaporation, based on the above-mentioned studies that used and discussed annual amounts.

Except for tropical regions and those where the effect of snowfall is considerable, in most countries with a humid climate located in the middle latitudes, the actual evaporation shows a clear seasonal variation. In such areas, the short-term analysis of water budgets which Linsley *et al.* proposed in 1958 can be applied to any small basin on the assumption that the amount of river discharge is equivalent to the amount of stored water in the basin, since any difference in stored water, ΔS, is assumed to be negligible as long as both the primary and the end date of timings of the same discharge amounts used are selected to fall within one or two months of each other. Suzuki (1980) used this method when collecting ten years of hydrological data in a mountainous headwater basin in Japan and succeeded in determining monthly amounts of evaporation. The attained result will be treated in the next section.

1.4.2 Development of a synthetic hydrological model

Though we succeeded in explaining the formation system of flood runoff in Section 1.3.2, additional issues such as direct runoff and evaporation processes were left unresolved. The HYCYMODEL (Fukushima, 1988) was developed and proposed to quantitatively determine the hydrological effects of reforestation. It is a type of conceptual runoff model and has features that assume only seven parameters with time independence in a runoff formation system. The structure of the HYCYMODEL is shown in Figure 1.10

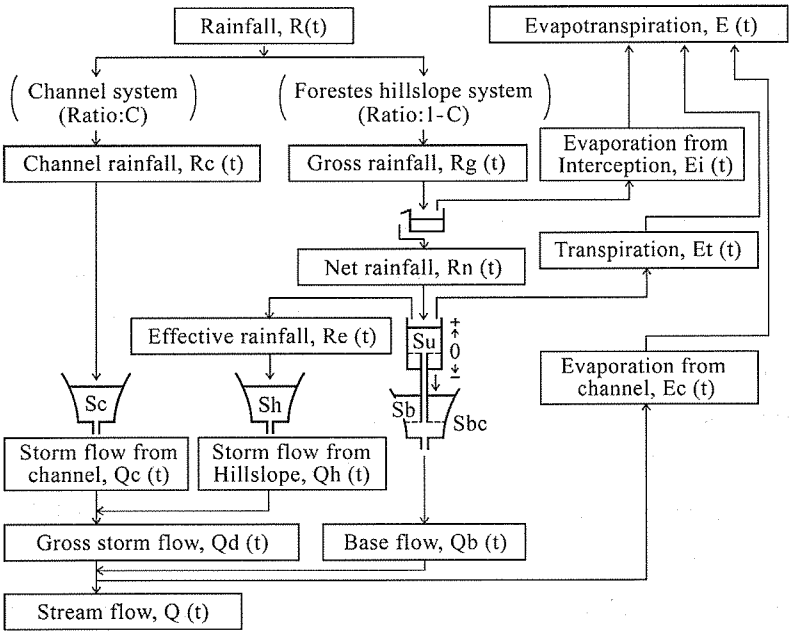

Figure 1.10 Structure of HYCYMODEL (Fukushima, 1988)

In Figure 1.10, C indicates the area ratio of an impermeable channel. Effective rainfall, $Re(t)$, all

other areas except for the impermeable channel areas is determined by the mean effective soil depth parameter, D_{50}(mm), and its deviation, D_{sig}. *Re(t)*, is calculated by the following detail procedure.

At first, an apparent storage in the *Su* Tank of Figure 1.10, *Su'(t)* is

$$S'u(t) = Su(t-1) + Rn(t) \tag{1.13}$$

where *Su* is storage in the *Su* Tank, *Rn* is net rainfall reaching to the ground, and *t* is the time step.

The variable for the normal distribution, ξ, is

$$\xi = \{\log[S'u(t) / D_{50}]\} / D_{sig} \tag{1.14}$$

D_{sig} is defined as follows:

$$D_{sig} = \log(D_{50} / D_{16}) \tag{1.15}$$

The *m* value, i.e., the contributing area ratio, can be calculated as an excess probability using the normal distribution.

$$m = \int_{-\infty}^{\xi} \frac{1}{\sqrt{2\pi}} \exp\left(-\frac{x^2}{2}\right) dx \tag{1.16}$$

The effective rainfall forming a direct runoff component, *Re(t)* , is

$$Re(t) = m \cdot Rn(t) \tag{1.17}$$

Since the author assumes that effective rainfall is derived from the saturated surface, its ratio therefore varies according to the saturated area and rainfall intensity. That assumption seems to agree with the idea of Dunne *et al.* (1982).

The relationships between storage *S* and discharge rate *Q* in each Tank on Figure 1.10 are assumed as follows:

$$Sc = KcQc^{0.6}, Sh = KhQh^{0.6} \tag{1.18}$$

$$Su = KuQu \tag{1.19}$$

$$Sb = KbQb^{0.1} \tag{1.20}$$

where *Kc*, *Kh*, *Ku* and *Kb* are the respective parameters.

Equation (1.18) is used to express the direct runoff component in each channel or hillslope system, Equation (1.19) the change in soil water at the top soil layer, and Equation (1.20) the base-flow component. The power of Equation (1.18) was assumed to be based on 0.6 by the previous study (Fukushima, 1981), that used a parallel-slopes model, since the motion of surface and sub-surface flows is approximated by Manning's law. The power of Equation (1.20), 0.1, was determined by least-square error analysis and satisfies the analysis of a saturated-unsaturated flow regime in the slope system (Suzuki, 1984).

In order to apply the HYCYMODEL to actual headwater basins, evaporation, *Ei(t)*, transpiration, *Et(t)*, in slope system and channel evaporation, *Ec(t)*, should be determined. This subject is to be mentioned in Section 1.4.3.

Finally, the direct runoff component, *Qd(t)*, is written as follows;

$$Qd(t) = C \cdot Qc(t) + (1-C) \cdot Qh(t) \tag{1.21}$$

Evaporation component, $E(t)$, is written as follows:

$$E(t) = C \cdot Ec(t) + (1-C) \cdot [Ei(t) + Et(t)] \quad (1.22)$$

Anyhow, HYCYMODEL has only seven time-independent parameters such as C, D_{16}, D_{50}, Kc, Kh, Ku and Kb, and it can be used for short-term flood events to long-term runoff analysis.

1.4.3 Application of HYCYMODEL to a small headwater area

The HYCYMODEL was applied to the mountainous small headwater at first called the Kiryu Experimental Basin which is underlain by granite, 5.99 ha in area, and covered by pine and cedar. Almost eighty years have passed since its reforestation, and it has had a reliable stream flow and rainfall data during the past ten years at hourly time intervals. Moreover, the parameters controlling evapotranspiration have been investigated and determined in this basin.

At first, the monthly mean evapotranspiration amounts have been estimated by the short-term water budget method (Suzuki, 1980). Secondly, the relationship between rainfall intensity and rainfall interception has been modeled at one hour intervals by field investigations and analysis (Suzuki *et al.*, 1979a, 1979b). Concerning the modeling of rainfall interception on forest canopy, Gash *et al.* (1978,1980) and Hattori (1982) have reported using the rainfall interception model developed by Rutter *et al.* (1971/1972). The results show that the rainfall interception component is not negligible in humid mountainous areas (Fukushima, 1988).

Suzuki (1980) considered that the monthly mean evapotranspiration minus the monthly mean rainfall interception calculated by the model equals the monthly mean transpiration. The bold solid line in Figure 1.11 indicates the monthly mean distribution of the transpiration estimated in the Kiryu Experimental Basin by Suzuki (1980).

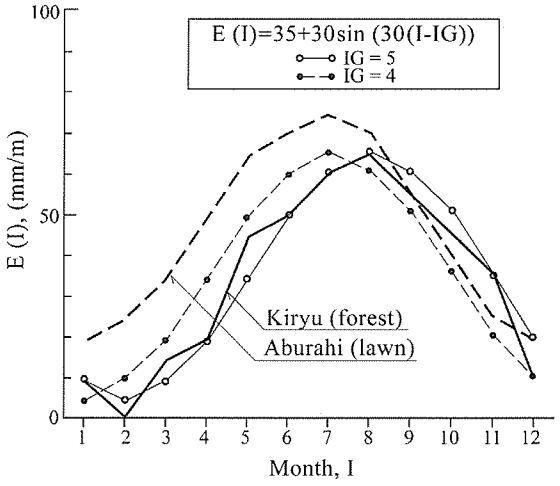

Figure 1.11 Approximation of transpiration on different land surfaces from the estimated monthly transpiration determined at Kiryu and other basins (Fukushima and Kuroda, 1989)

With the HYCYMODEL, the obtained monthly mean transpiration is first taken as monthly potential transpiration rate, $e_p(i)$. Actual transpiration is controlled by the Sb amount. Now, the model assumes the critical storage to restrain transpiration, Sbc. Thus, the actual transpiration is estimated by the following rule:

$$Et(t) = e_p(i), \qquad if\ Sb \geq Sbc \tag{1.23}$$

$$Et(t) = e_p(t) \cdot Sb(t) / Sbc, \qquad if\ Sb \leq Sbc \tag{1.24}$$

where $Sb(t)$ and Sbc are calculated by Equation (1.20).

The model of rainfall interception may be rather complicated, but the concept is not so difficult. It is a transformation system from the gross rainfall, $Rg(t)$, to the net rainfall, $Rn(t)$, on the HYCYMODEL shown in Figure 1.10. Generally, the maximum storage on canopy and trunk and its evaporation rate were assumed as 1.97 mm and 0.162 mm/hr in Kiryu, respectively. Nowadays, the evaporation rate on wet canopy can be estimated by Penman-Monteith's equation, but the maximum storage parameter is not easily determined because it has no direct relation with the leaf-area index. The monthly distribution of the evaporation rate in the cannel system was represented by the same rate of transpiration as in Kiryu because the C value is rather small at C=0.035. Although the author has considered the restraining effect of transpiration using Qbc, its effect clearly became small in Kiryu in temperate-humid climate.

The sequential estimation of hourly stream flow during ten years has corresponded well with the observed one, as it confirmed not only long-term runoff, but also short-term flood runoff; the change of base flow, moreover seems rational, and the effect of the antecedent rainfall can be explained as a change in water storage in the basin (Fukushima, 1988).

Figure 1.12 shows the relationship between cumulative rainfall and direct runoff by different rainfall intensities. This means that the direct runoff is very much controlled by rainfall intensity and cumulative rainfall amount. It should be understood and used for flood forecasting and flood countermeasures.

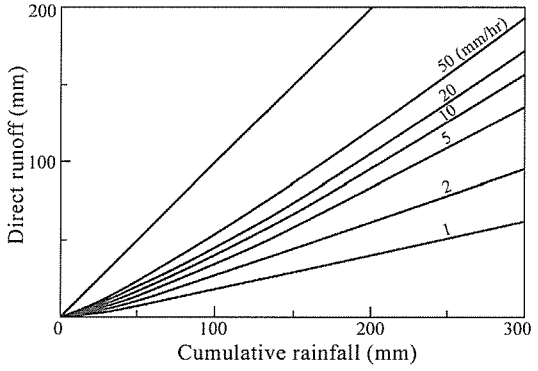

Figure 1.12 The relationship between cumulated rainfall and direct runoff estimated by different rainfall intensities (Fukushima, 1988)

1.4.4 Evaluation of reforestation by HYCYMODEL

The parameters of the HYCYMODEL were determined by application to the observed hydrographs chosen from the six mountain small headwater basins located within the same granite mountain. Figure 1.13 shows the number of years that had passed since the reforestation works had been completed. The gray lines in each hydrograph show the lines of both the entire flow and base flow estimated.

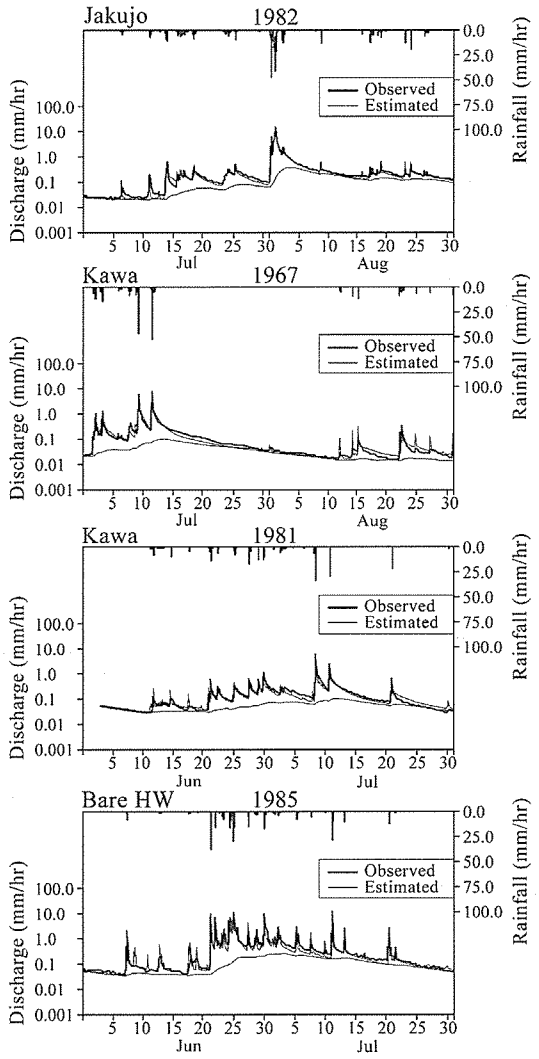

Figure 1.13 Estimated hydrographs at daily interval in terms of years since reforestation, Mount Tanakami, Japan (Fukushima and Suzuki, 1987)

As the parameters such as *C*, D_{16}, D_{50}, *Kc*, *Kh* and *Ku* mainly control quick flow, the validation was done using the data of rainfall and discharge with the time interval at either twenty minuets or one hour, but *Kb* and the parameters controlling evaporation were determined using long-term daily data because they were concerned with base flow. Concerning the transpiration rate in each basin,

the trigonometric function shown in Figure 1.11 was approximated. The function is as follows:

$$Et(I) = Delta \cdot \{35 + 30\sin[30(I - IG)]\} \tag{1.25}$$

where I is the month explained by 1-12. Therefore, the parameters controlling the transpiration rate are *Delta* and *IG*.

The decrease from the gross rainfall, *Rg(t)*, to the net rainfall, *Rn(t)*, is an effect of the rainfall interception. After the intercepted rainfall in each basin estimated by hourly data, it was converted to daily data as shown in the following function:

$$Rn(t) = AG \cdot Rg(t) - AI \tag{1.26}$$

where *AG* and *AI* are parameters estimated by the hourly application.

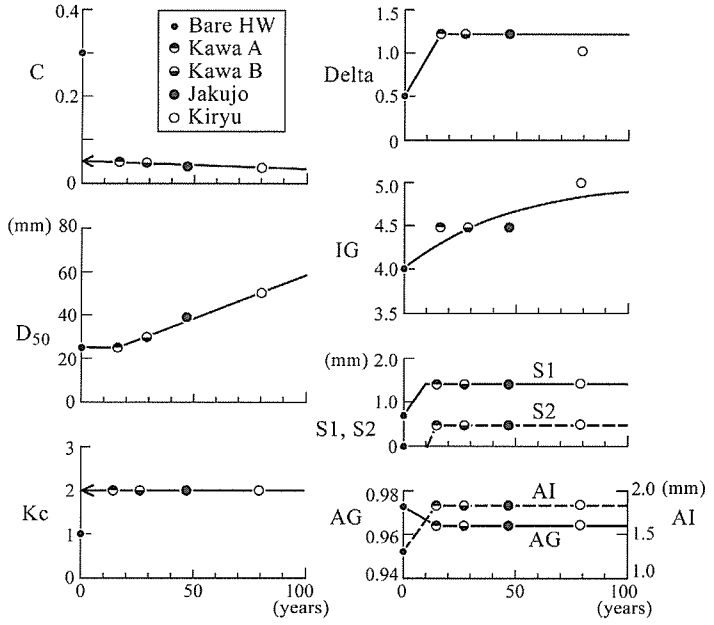

Figure 1.14 HYCYMODEL parameters determined by the application (Fukushima and Suzuki, 1987): *C*, D_{50}, *Kc* are parameters controlling delay time; *Delta* is the ratio of monthly transpiration; *IG* is the phase change in the sine function listed in Figure 1.11; *S1* and *S2* are parameters concerned with rainfall interception on the canopy and trunk, respectively; *Ag* and *AI* are also parameters of the interception aggregated to daily interval; *AI* means the maximum amount of daily rainfall interception; *AG* is its evaporation rate.

The results obtained by the application for each basin versus the passing years after reforestation works are shown in Figure 1.14. The unlisted parameters are exactly the same as the values obtained in the Kiryu Experimental Basin (Fukushima, 1988).

Now, it became possible to quantitatively estimate stream flow in headwater basin on reflecting forest effects. Figure 1.15 is an attempt explaining the deference of stream flow by the forest re-growth when the same rainfall data are inputted to the HYCYMODEL. The hydrograph passing

100 years after reforestation seems to be very mild, but the hydrograph at bare basin shows a rapid change and wide fluctuation.

The annual changes of water balance components, such as evaporation, direct runoff and base flow, are simulated at ten-year intervals after reforestation. The result is shown in Figure 1.16 as the ratio of rainfall amount. It indicates that a devastated basin without vegetation produces a much larger total runoff, consisting of direct runoff and base flow component, and that it does a less amount in both evaporation and base flow components than that with vegetation.

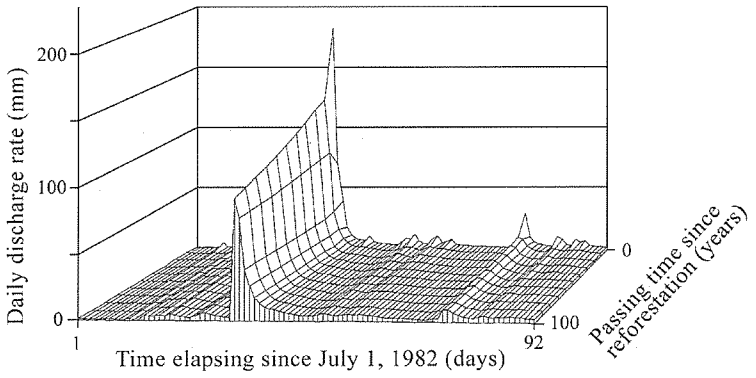

Figure 1.15 Simulated hydrographs during three months (=ninety-two days) showing how the passing years after reforestation do affect to stream flow during 100 years, using the same rainfall data and with an interval of ten years after reforestation. (Fukushima and Suzuki, 1987)

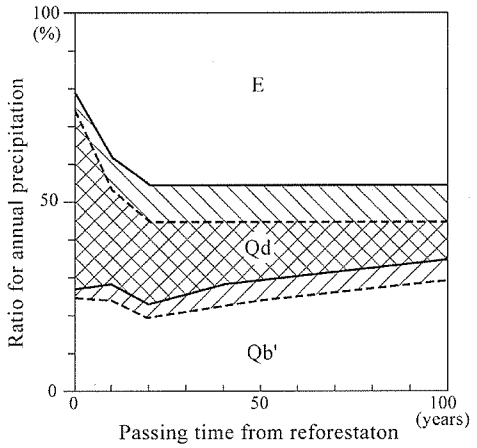

Figure 1.16 Change of water balance components at different times after reforestation. Hatched parts indicate the results of years with much/less annual rainfall than the mean. (*E*: Evapotranspiration; *Qd*: Direct runoff; *Qb'*: Base flow) (Fukushima and Suzuki, 1987)

After almost twenty years, the ratio of evaporation reached maximum because the forest canopy almost entirely closes to cover the land surface. The tendency is not changed in the year with either much or less rainfall, as shown by the two kinds of slant lines. Generally, river water of the base

flow component in the headwater is clean and is easily available to meet the entire demand. How to increase the base flow component is the ultimate objective in considering headwater management. Although it is true that a devastated mountain can supply much more water downstream than in a forested area, nowadays all of us recognize that river water from bare land contains 100 to 1,000 times the sediment yield of that in a forested area as shown in Figure 1.1. Figure 1.16 indicates that the ratio of base flow recovers almost 50 to 60 years later after the reforestation. This means that the worth of reforestation should be recognized and supported by those who wish to maintain sustainable life in a long-term perspective.

1.4.5 Hydrological effects on land use change

Hydrological differences between a forested mountain and a golf course were investigated at Aburahi basin, in a mountainous area near Lake Biwa, central Japan (Fukushima and Kuroda,1989). Hydrological components were separated by the application of the HYCYMODEL from the data over a year. The water budget in both areas is shown in Figure 1.17.

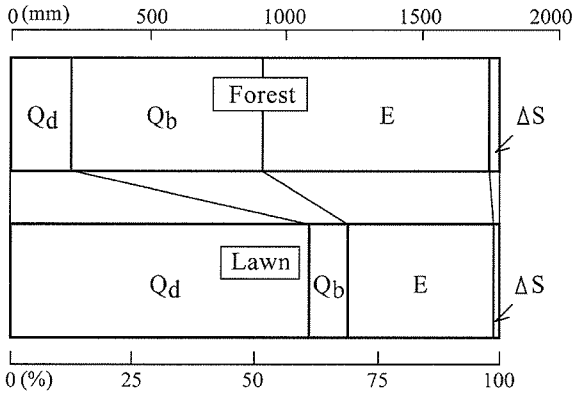

Figure 1.17 Comparison of Water budgets in forested mountain and golf course (Fukushima and Kuroda, 1989) (*Qd*: direct runoff; *Qb*: base flow; *E*: evapotranspiration; *ΔS*: changes of storage). Lawn here means the golf course.

This shows that the evaporation amount in the golf course is smaller than that in the forested area. On the other hand, the monthly evaporation amount in the golf course was founded to agree with the values estimated by Priestly-Taylor's Equation (1972), which has only two parameters, these are radiation balance and air temperature. If we consider a golf course to represent grass land, this result is understandable. And the direct runoff amount in a golf course is much larger than in a forested area. It is also easy to understand that a golf course has been built with an underground drain network system in order to be able to keep playing golf even on rainy days in Japan. This result was included in the annual report published by the Japanese Ministry of the Environment, in 1994.

In the same period, the rain and stream waters were collected at one week interval. The chemical

budget attained is shown in Table 1.2. Except pH, the unit of other components is explained as a unit of kg/ha/yr. Table 1.2 shows that pH of rain water is smaller than that in stream, and that the chemical components such as N and P are poor in the stream water than that in rainwater. And only these components in golf course show larger than that in forested area. It seems that chemical fertilizer is used for the maintaining golf course as just the same as agricultural field. But, the other geochemical components seem to hold almost the same amount in both forested area and golf course.

Table 1.2 The input/output of water chemicals (kg/ha/yr)

	R	Qf	Qg	R-Qf	Qg/Qf
pH	4.64	7.58	7.43	-	-
SS	-	87.9	84.0	-	0.96
HCO_3	-	333.5	354.8	-	1.06
Cl	24.1	48.7	105.6	-24.6	2.17
SiO_2	-	64.9	58.6	-	0.90
SO_4	24.7	58.8	173.6	-34.1	2.95
NH_4-N	3.72	0.04	0.05	3.68	1.25
NO_3-N	3.27	2.56	3.73	0.71	1.45
Org-N	1.08	0.28	3.97	0.80	14.2
Total-N	8.07	2.88	7.75	5.19	2.69
P	R	0.081	1.625	0.465	20.1
K	3.75	10.34	34.15	-6.59	3.30
Ca	4.97	66.65	88.49	-61.68	1.33
Mg	1.40	18.25	38.23	-16.85	2.09
Na	7.55	47.27	64.67	-39.72	1.37

(R: Rain water; Qf: Stream water from forested area; Qg: Stream water from lawn area)

1.5 Estimates of evaporation and snowmelt by energy budget

1.5.1 Frame of energy budget near the land surface

It was clarified that the HYCYMODEL was very effective to analyze the observed hydrological data in relation to the principal hydrological components and to understand the real hydrological phenomena in Section 1.4.3-1.4.5, but it became clear that some issues were unresolved yet. It means that application to different climate regions is still difficult because the energy budget was not considered. However, evaporation and snowmelt processes are usually discussed recently within

the framework of the energy budget because the routinely observed meteorological data became available to the hydrological research community.

Generally, the radiation budget is written as follows:

$$Rnt = Rs\downarrow + Rs\uparrow + Rl\downarrow + Rl\uparrow = (1-alb)Rs\downarrow + Rl\downarrow - \varepsilon\sigma T_s^4 \quad (1.27)$$

where Rnt is the net radiation, $Rs\downarrow$ is the incoming short-wave radiation or solar radiation, $Rs\uparrow$ is the outgoing short-wave radiation, $Rl\downarrow$ is the incoming long-wave radiation or atmospheric radiation, $Rl\uparrow$ is the outgoing long-wave-radiation, alb is the albedo, ε is the emission ratio, σ is the Stefan-Boltzmann constant, and T_s is the surface temperature.

$Rs\downarrow$ and $Rl\downarrow$ can be observed by using some equipment and can be estimated by using some formula and substitute data such as the sunshine ratio.

Net radiation is also written near land surface as follows:

$$Rnt = H + \lambda E + G \quad (1.28)$$

where H is the sensitive heat flux, λE is the latent heat flux, λ is the latent heat of evaporation, E is the evaporation and G is the soil heat flux.

1.5.2 SVAT model for estimating evaporation and snowmelt

In Equation (1.28), the rather applicable model is called SVAT model (Soil-Vegetation-Atmosphere Transfer scheme). The Penman-Montheith model (1965, 1975) is a representative SVAT model developed on the basis of the Penman equation (1948). Penman has made a model scheme on the wet-land surface, and Penman-Monteith(1965, 1975) expanded it to the unsaturated land surface with vegetation cover. This frame was then expanded under consideration of the interactions among components, aiming at the numerical simulation of land surface processes such as evaporation, snowfall and the change of active layer depth in Siberian permafrost regions (Ma *et al.*, 1998). Its model, which sometimes may be called a big-leaf model or a single layer model was applied to the mountainous headwater in Japan, aiming at the estimation of evaporation, snowfall and snowmelt (Ma *et al.*, 1999).

The latent heat flux, λE, and the sensible heat flux, H, are written as the following equations in the big leaf model.

$$\lambda E = \frac{\Delta(R_{nt} - G) + \rho_a c_a \delta q / r_a}{\Delta + \gamma(1 + r_s / r_a)} \quad (1.29)$$

$$H = \frac{(R_{nt} - G)\gamma(1 + r_s / r_a) - \rho_a c_a \delta q / r_a}{\Delta + \gamma(1 + r_s / r_a)} \quad (1.30)$$

where Δ is the slope of the saturated vapor pressure curve at air temperature Ta, γ is the psychometric constant, c_a is the specific heat of the air, ρ_a is the density of air, δq is the specific humidity deficit, r_a and r_s are aerodynamic resistance and surface resistance, respectively.

The aerodynamic resistance, r_a is written as follows:

$$r_a = \frac{1}{\kappa u_*}\left[\ln\left(\frac{z_w - d}{z_{oh}}\right) - \Psi_k\left(\frac{z_w - d}{L}\right)\right] \tag{1.31}$$

where, z_w is the measurement height, d is the displacement height, z_{oh} is the roughness length for scalar variables, κ is the Karman's constant, u_* is the friction velocity.

the friction velocity, and u_* is written as follows:

$$u_* = \frac{\kappa u}{\left[\ln\left(\frac{z_w - d}{z_o}\right) - \Psi_m\left(\frac{z_w - d}{L}\right)\right]} \tag{1.32}$$

where u is the wind speed, and z_o is the roughness length for momentum.

The terms of Ψ_k and Ψ_m in Equations (1.31) and (1.32) are the stability correction functions for scalar fluxes and momentum, respectively.

If snow-surface exists on land, the following equation proposed by Kondo and Yamazaki (1990) is available.

$$Ms = \varepsilon(Rl\downarrow - \sigma T_s^4) - H - \lambda E - G \tag{1.33}$$

where Ms is the snowmelt.

The surface temperature has the following relationship of air temperature, Ta and sensible heat flux, H. The detailed numerical procedure and the computer program are shown in Ma and Fukushima (2002).

$$T_s = Ta + H\frac{\gamma_a}{\rho_a c_a} \tag{1.34}$$

According Blyth and Harding (1995), the surface resistance, r_s can be explained by the next equation,

$$r_s = r_{s\min}\exp(\beta\delta q) \tag{1.35}$$

Where r_{smin} is the minimum surface resistance and β is a constant.

Ma *et al.* (1999) have found the value of r_{smin} has a linear relationship for the radiation-dryness index, RDI, which is determined by the net radiation divided by the precipitation during two or three months, as shown in Figure 1.18.

By the development of the SVAT model, it has become possible to estimate quantitatively the evaporation and snowmelt amounts for forest and grassland, in different climate regions. Nowadays, this SVAT model is used for estimating evapotranspiration components of the previously proposed HYCYMODEL. The estimation of snowmelt is shown in Figure 1.19 as an example of a forested mountainous basin in rather warm-temperate climate condition.

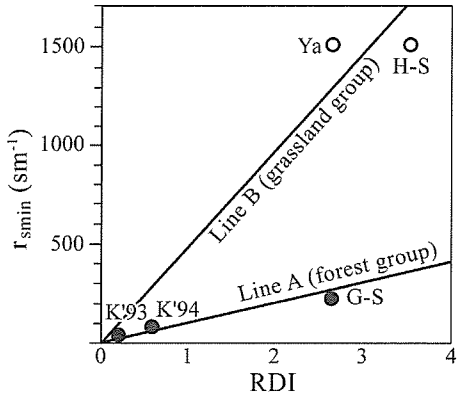

Figure 1.18 The relationship between Radiation-dryness index, RDI, and minimum surface resistance, r_{smin} (Ma *et al.*, 1999). Here, Ya: grassland in Yakutsk, Siberia; H-S: bush-land in HAPEX-Sahel; G-S: Forested area in Yakutsk; K'93: Ashu, Japan 1993; K'94: Ashu, Japan 1994.

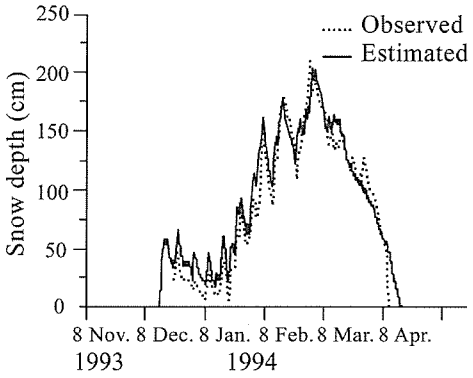

Figure 1.19 A change in snow depth estimated by the SVAT model in the Ashu Experimental Forest of Kyoto University, Japan (Ma *et al.*, 1999)

1.6 Conservation of headwater on hydrology

The reason why headwater's exist seems that it has either so many rainy days or little evaporation amount first, the slope system can supply comparatively much of the lateral flow because base flow component is rich secondly and the capacity to outflow to downstream is less topographically, thirdly. In a sense, headwaters are formatted by the condition of climate, geology and topology.

Generally, headwaters may have a different water quality from these in dry areas, which have thick deposits of organic matter because its decomposition is so slow. At the same time, we need to pay attention to that most headwater wetlands are unstable by climate changes due to a transit stage on geomorphologic cycle.

Acknowledgement

The author would like to express his thanks to Dr. Xieyao Ma, Frontier Research System for Global Change, Japan, for his helpful comments on the manuscript.

References

Blyth, E.M. and R.J. Harding (1995): Application of aggregation models to surface heat flux from the Sahelian tiger bush. *Agri. For .Meteol.*, 72, 213-235.

Bosch, J.B. abd J.D. Hewlett (1982): A review of catchment experiments to determine the effect of vegetation changes on water yield and evaporation. *J. Hydrol.* 55, 3-23.

Chorley, R.J. (1978): The hillslope hydrological cycle, Hillslope Hydrology, edited by M.J. Kirkby, John Wiley &Sons, 20-21.

Dunne, T., T.R. Moore and Tayor(1975): Recognition and prediction of runoff-producing zones in humid regions. *Hydrol. Sci.*, 20(3), 305-327.

Fukushima, Y(1981): Formation system of short-term flood runoff in small headwater basins. Ph.D dissertation, Kyoto Univ, Kyoto, 1-76. (in Japanese)

Fukushima, Y. and M. Suzuki (1987): Effects of stream flow on reforestation in granitic hilly mountain. *J. Water Science*, 177, 17-34. (in Japanese)

Fukushima, Y. (1988): A model of river flow forecasting for a small forested mountain catchment. *J. Hydro. Processes*, 2, 167-185.

Fukushima, Y. and Y. Kuroda(1989): Differences of stream runoff and mineral budget between a golf course and a forested area. *Proc. Int'l. Symp. Headwater Control*, Prague, 32-38.

Gash, J.H.C. and A.J .Morton (1978): An application of the Rutter model to the estimation of the interception loss from Thetford Forest. *J. Hydrol.*, 38, 49-58.

Gash, J.H.C., I.R. Wright and C.R. Lloyd (1980): Comperative estimates of interception loss from coniferous forests in Great Britain. *J. Hydrol.*, 48, 89-105.

Hattori, S., H. Chikaarashi and N. Takeuchi (1982): Measurement of the rainfall interception and its micrometeorological analysis in a Japanese cypress stand., *Bull. For. Res. Inst.*, 318, 79-102.

Horton, R.E. (1933): The role of infiltration in the hydrologic cycle., *Trans. A.G.U.*, 446-460.

Horton, R.E. (1939): Analysis of runoff-plat experiments with varying infiltration-capacity., *Trans. A.G.U.*, 20, 693-711.

Hewlett, J.D. and A.R. Hibbert(1967): Factors affecting the response of small watersheds to precipitation in humid areas. *Intern. Symp. Forest Hydrology*. Pergamon Press.

Kondo, J. and T. Yamazaki (1990): A prediction model for snowmelt, snow surface temperature and freezing depth using a heat balance method. *J.Applied Meteorology*, 29, 375-384.

Linsley, P.K., M.A. Kohler and J.L. Paulhus (1958): Hydrology for engineers, McGraw-Hill, New York, 113-116.

Ma, Xieyao, T. Hiyama, Y. Fukushima and T. Hashimoto (1998): A numerical model of the heat transfer for permafrost regions. *J. Jpn Soc. Hydrol. &Water Resour.*, 11-4, 346-359.

Ma, Xieyao, Y. Fukushima, T. .Hiyama, T. Hashimoto and T. Nakashima (1999): Application of a simple SVAT Model in a Mountain Catchment under temperate humid climate. *J. Jpn Soc. Hydrol. & Water Resour.* 12-4, 285-294.

Ma, Xieyao, Y. Fukushima, T. Hiyama, T. Hashimoto and T. Ohata (2000): A macro-scale hydrological analysis of the Lena River basin. *J. Hydrol. Processes.* 14, 639-651.

Ma, Xieyao and Y. Fukushima (2002): Numerical model of river flow formation from small to large scale river basin. Mathematical Models of Large Watershed Hydrology. edited by V.P. Singh and D.K. Frevert. Water Resources Publications, LLC, USA. 433-470.

Meyer-Peter, E. and R. Müller (1948): Formulas for bed-load transport, *Proc. The 2nd Congress of the Inter'l Assoc. for Hydraulic Res.*, Stockholm, Sweden.

Monteith, J.L. (1965): Evaporation and environment, *Symp. Soc. Exp. Biol.*, 19, 206-234.

Monteith, J.L. (1973): Principles of environmental physics, Edward Arnold Press Ltd.

Penman,H.L. (1948): Natural evaporation from open water, bare soil and grass. *Proc. Roy. Soc.*, London A, 193, 120-145.

Priestley, C.H.B and J. Taylor (1972): On the assessment of surface heat flux and evaporation using large-scale parameters, *Monthly Weather Review*, 100(1), 81-91.

Rutter, A.J., K.A. Kershaw, P.C. Robins and A.J. Morton (1971/1972): AQ predictive model of rainfall interception in forests.(1)Deviation of the model from observation I a plantation of Corsican pine. *Agr. Meteorol.*, 9, 367-384.

Schulze, R.E. and W.J. George(1987): A dynamic, process-based, user-orientated model of forest effects on water yield. *J. Hydrol. Processes*, 1, 293-307.

Seno, K., S. Ohyagi and Y. Fukushima (1981):Erosion control and a granite mountain in Japan. *Proc. South-east Asian Symp. Problems of soil erosion and sedimentation*, Bangkok, 95-105.

Suzuki, M and Y. Fukushima (1989):Sediment yields in bare and forested mountain. *J. Water Science*, 190, 89-100. (in Japanese)

Suzuki, M., H. Kato, M. Tani and Y. Fukushima (1979a): Throughfall, streamflow and rainfall interception in Kiryu experimental catchment,(1) Troughfall and stemflow, *J. Jpn. For. Soc.*, 61, 202-210.

Suzuki, M., H.Kato, M.Tani and Y. Fukushima (1979b): Throughfall, streamflow and rainfall interception in Kiryu experimental catchment, (2)Rainfall interception, *J. Jpn. For. Soc.*, 61, 391-398.

Suzuki, M. (1980): Evaporation from a small catchment in hilly mountains, (1) Seasonal variations in evaporation, rainfall interception and transpiration, *J. Jpn. For. Soc.*, 62, 46-53.

Suzuki, M. (1984): The properties of a base-flow recession on small mountains watersheds, (1)

Numerical analysis using the saturate-unsaturated flow model, *J. Jpn. For. Soc.*, 66, 174-182.

Suzuki, M. (1985): Evapotaranspiration estimates of forested watersheds in Japan using the short-time budget method, *J. Jpn. For. Soc.*, 67, 115-125.

Swift Jr, L.W. and W.T. Swank(1981): Long term responses of stream flow following clearcutting and regrowth. *Hydrol. Sci.* 26(3), 245-256.

Takei, A., S. Kobashi and Y. Fukushima (1981):Erosion and sediment transport measurement in a weathered granite mountain area. *Publ. IAHS*, 133, 493-501.

Tischendorf, W.G. (1969):Tracing stormflow to Varying source area in small forested watershed in the southern piedmont, Ph.D dissertation, Univ. Georgia, Athens, Georgia, 1-114.

Chapter 2

Ocean Circulations & Climate

Youichi Tanimoto
Graduate school of Environmental Science
/Faculty of Environmental Earth Science, Hokkaido University
Kita 8, Nishi 5 Kita-Ku, Sapporo 060-0808, JAPAN
e-mail: tanimoto@ees.hokudai.ac.jp

2.1 Ocean properties and climate

2.1.1 Outlines

It is well known that ocean properties have large potential to give substantial influences on climate of our planet. Those effects are summarized as follows,

Ocean absorbs nearly a half amount of solar energy at the top of atmosphere, and releases the same amount heat by evaporation, and other processes. So the ocean is in heat balance.

Ocean plays a role of moisture source for atmosphere. Water vapor is one of the active greenhouse gases that emit and absorb infrared radiation. During the period of less solar heating in winter, downward emission from moist atmosphere is important in keeping mild climate at the surface.

Ocean has larger inertia than atmosphere. Residence time is from a few weeks to hundreds-thousands years. Deeper circulation tends to have longer time scale.

Because of the large inertia, the ocean gains and stores heat in summer time, and release it in winter time. As a result, ocean temperature, marine air temperature, land air temperature near the coast has small amplitude of the seasonal cycle. As a consequence, the ocean plays a role of energy and moisture source for the atmosphere.

Ocean water can be transported with its property of temperature and salinity. Heat transport by the ocean reduces the meridional thermal gradient between the tropics and polar regions, and provides regional characteristics of climate.

2.1.2 Properties of ocean waters

One of most important ocean properties is sea water density that is a function of temperature,

salinity and pressure. Because of a linear relation of salinity and a non-linear relation of temperature on density, isopycnal contours on temperature-salinity diagram show curves rather than straight lines as shown in Figure 2.1. Hence, warm saline and cold less saline waters can be mixed in the same density layer. After this isopycnal mixing, the density become higher in the mixing waters than in the original waters.

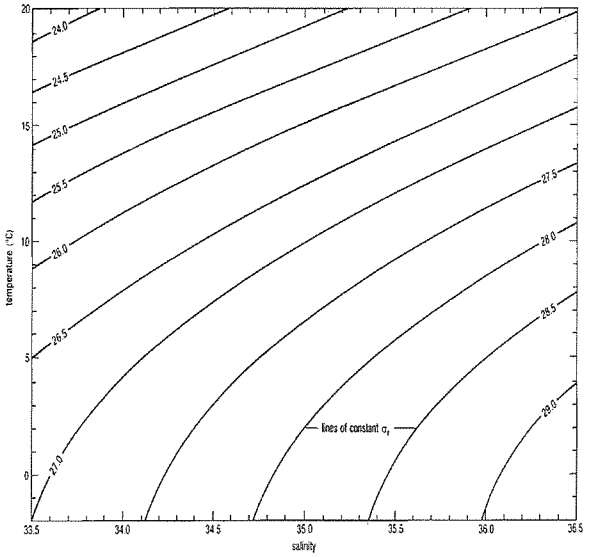

Figure 2.1 Temperature-salinity diagram with contours of dencity, which has units, kg m^{-3}. [From Seawater:its composition, properties and behaviour, The Open University, 1989].

Temperature mostly determines water density at more than 15°C. Therefore, sea water densities in the tropical and subtropical regions mostly depend on its temperature. By contrast, at nearly freezing point, salinity rather than temperature is a major factor on density. In the polar regions, salinity is an important factor in determining density.

Waters have unique physical properties to other materials. Thermal expansion coefficients and compressibility are smallest in liquid materials as well as mercury. Specific heat, latent heat of evaporation and melting are largest in all of materials except for ammonia. Large thermal capacity by large specific heat and large density in ocean than in atmosphere reduces temperature variations and associated density changes. Small thermal expansion coefficients and compressibility also reduce density changes. These effects make the ocean waters moving very slow. Large latent heat of melting requires strong cooling for water freezing. While large latent heat of evaporation is associated with large heat release from the ocean into the atmosphere, large heat capacity reduces temperature variations forced by evaporative cooling.

2.1.3 Climatological sea surface temperature and salinity

Through the ocean surface, water, heat, and momentum exchange between ocean and atmosphere. Therefore, sea surface temperature (SST) and salinity (SSS) are basic boundary conditions of the

ocean circulations. In this section, large-scale characteristics of SST and SST will be documented. SST and SSS contours tend to be parallel to latitude because the solar heating and associated evaporation are mostly in function of latitude (Figure 2.2). However, those contours are neither equatorial symmetric nor zonally symmetric.

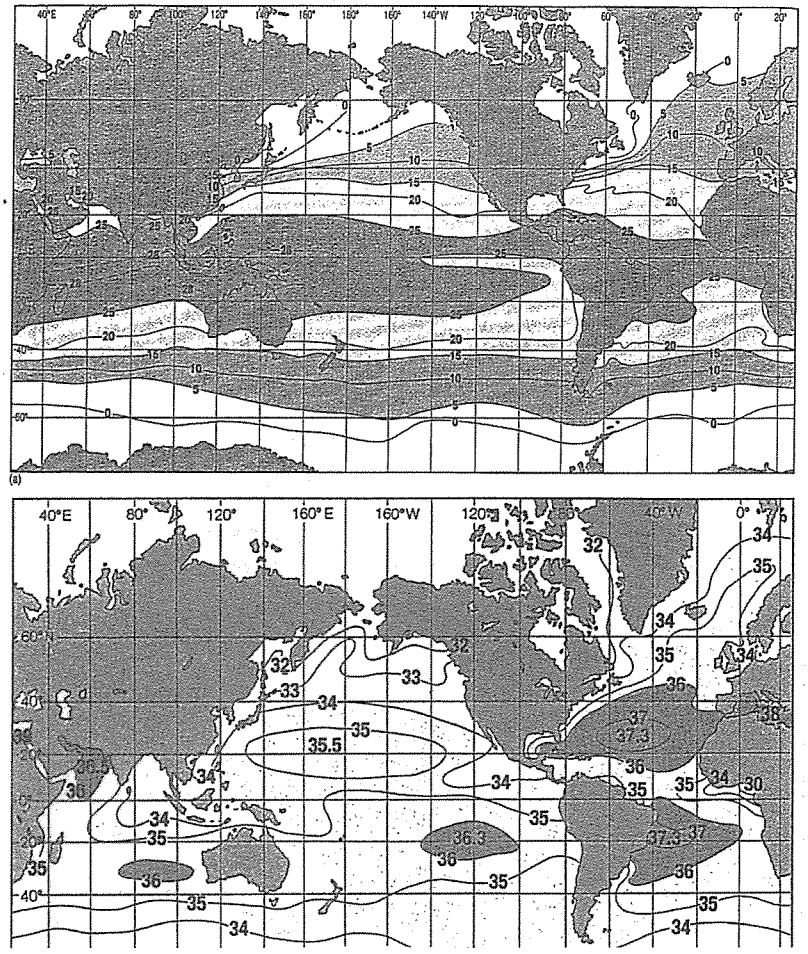

Figure 2.2 Climatological SST in February (upper panel, °C) and annual mean SSS (lower panel, ‰).[From Ocean Circulation, The Open University, 1989].

Due to the ocean circulation, steep SST front forms in 30-40° latitude in either of hemispheres. As shown in Figure 2.3, one of the most strong ocean surface current is Kuroshio current in the western North Pacific. The counterpart of the current in the North Atlantic is Gulf Stream. At around 35°N, both of the currents separate from the western boundary (Japanese islands for Kuroshio and east coast of United states for Gulf Stream) and flow far eastward into the interior region of the ocean basin.

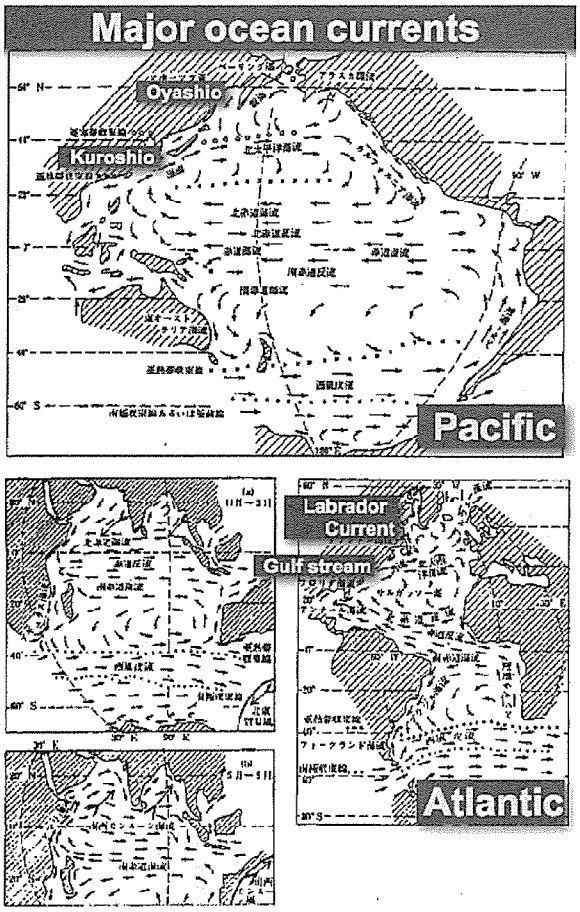

Figure 2.3 Schematic figure of the major ocean currents.

In the region north of these subtropical currents, there is a southward ocean surface current along the western boundary. Those currents are Oyashio in the western North Pacific, and Labrador current in the western North Atlantic. Warm northward and cold southward currents converge at around in 30-40° latitude of the western boundary, thereby from strong meridional gradient of temperature, SST fronts in the same region.

SSS tends to be high where annual mean evaporation exceeds annual mean precipitation, and vice versa. Indeed, a meridional plot of zonal mean SSS and E-P (evaporation minus precipitation) is correlated to one another in the annual mean field (not shown). In the subtropical region, climatological high sea level pressure (SLP) provides clear sky or less cloud, which increase solar heating and enhance evaporation.

In the subpolar region, by contrast, the sea fog and low-level cloud deck (stratus) prevail especially in summer. The increased cloud amount reduces solar heating and evaporation. In winter, extratropical synoptic weather disturbances (low pressure systems represented in daily weather maps in the mid-latitudes) are associated with the zonal elongated rainy zone in 30-40° latitude in the domain. Such a large-scale precipitation band tends to reduce SSS in the subpolar region. As shown

in Section 2.1.2, SSS in the subpolar region plays an important role in determining water density. A decreased SSS tends to prevent deep water formation that is essential for vertical circulation of the ocean.

2.1.4 Vertical cross section of temperature and salinity

Despite very shallow depth of the ocean (~4000m) to its basin scale (~10^{3-4}km), there is a vertical circulation of the ocean that provides characteristic distribution of temperature and salinity in the deep oceans (Figure 2.4). A basic vertical structure of the ocean consists of surface and deep layers. Between these layers, temperature sharply decreases with depth at around 1000m (We call this large gradient layers in temperature, main thermocline). Ocean waters over 4°C exist in the layers shallower than the main thermocline within 50 latitude. As stated in Section 2.1.3, evaporation minus precipitation is a major factor in determining salinity in surface layers. Fresher (low salinity) tongue from the polar region to low latitudes is distinct in the salinity section, indicating deep water formations at the surface in the subpolar region.

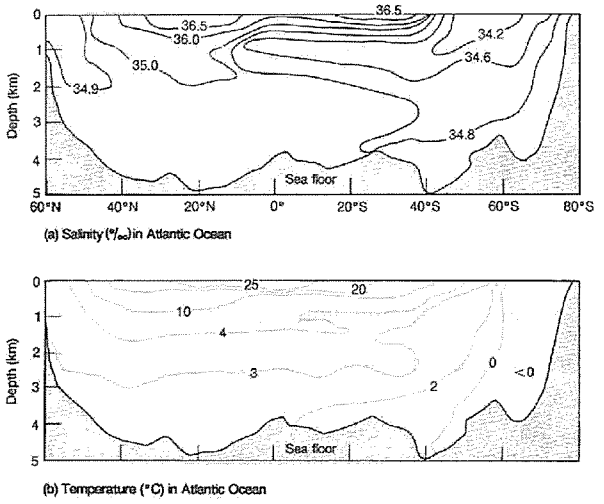

Figure 2.4 Vertical cross sections of salinity (upper panel) and temperature (lower panel) in Atlantic.

2.2 Climate of aqua planet

2.2.1 Moisture source

From the space, our planet looks like a blue ball due to the ocean covering 70% of the surface. Not as like in any surface type over the land, ocean surface has low albedo (reflectivity of the surface). Typical values are in 7-12% (see Table 2.1), indicating that ocean is efficient absorber of solar heating. Note that the ocean surface albedo strongly depends on solar zenith angle. Before the sunset and after sunrise when the solar zenith angle is large, ocean albedo are very large.

Table 2.1 Albedoes for various sufaces. [From Global Physical Climatology, Hartmann 1994].

Surface type	Range	Typical value
Water		
Deep water: low wind, low altitude	5–10	7
Deep water: high wind, high altitude	10–20	12
Bare surfaces		
Moist dark soil, high humus	5–15	10
Moist gray soil	10–20	15
Dry soil, desert	20–35	30
Wet sand	20–30	25
Dry light sand	30–40	35
Asphalt pavement	5–10	7
Concrete pavement	15–35	20
Vegetation		
Short green vegetation	10–20	17
Dry vegetation	20–30	25
Coniferous forest	10–15	12
Deciduous forest	15–25	17
Snow and ice		
Forest with surface snowcover	20–35	25
Sea ice, no snowcover	25–40	30
Old, melting snow	35–65	50
Dry, cold snow	60–75	70
Fresh, dry snow	70–90	80

Ocean is a major moisture source to the atmosphere. Spatial and temporal characteristics of moisture fields are very important in forming local climate. Since saturation of water vapor strongly depend on temperature, moistures are abundant in low-latitude and low-altitude. Likewise, a total moisture amount (= precipitable water, PW) in the atmospheric column denoted by

$$PW = \frac{1}{g}\int_0^{P_s} q\,dp$$

tends to be large in the low-latitude over the ocean. Contour lines of PW are closely correlated with SST contours (not shown). This indicates that the precipitation potential partly depends on the thermal condition of the ocean. We should note that PW is not directly related with the local intensity of the precipitation. Rather, moisture flux convergence is closely related with the local precipitation.

As stated in the previous section, the mean depth of the ocean is about 4 km, nearly corresponding to the water volume of 1.37 x 10^9 km^3. This volume is about 97% of total fresh water in our planet (Table 2.2). By contrast, fresh waters in the atmosphere and underground are very small in volume. Water volumes of 0.013 x 10^9 km^3 and 8.062x 10^9 km^3 are corresponding to 25 mm and 2m of liquid water in the mean depth.

Table 2.2 Water volume of our planet. [From Global Physical Climatology, Hartmann 1994].

Water Volumes of Earth

Category	Volume (10^6 km^3)	Percent
Oceans	1348.0	97.39
Polar ice caps, icebergs, glaciers	227.8	2.010
Groundwater, soil moisture	8.062	0.580[a]
Lakes and rivers	0.225	0.020
Atmosphere	0.013	0.001
Total water amount	1384.0	100.0
Freshwater	36.00	2.60

2.2.2 Hydrological cycle and mean resident time

The mean resident time of the fresh waters can be estimate based on the exchange rate of the fresh waters between the categories such as oceans, atmosphere, and underground. Annual precipitation and evaporation over the ocean and the land are about 1m $year^{-1}$ and 0.5m $year^{-1}$, respectively. Moisture flux in the atmosphere from the ocean to the land and river runoff from the land to the ocean is 0.11m for the ocean and 0.27m for the land. This difference between 0.11 and 0.27 is attributed to the ratio of ocean and land surface.

The schematic figure of water exchange (Figure 2.5) shows that, the mean resident time of the ocean is very long (~10^{3-4} years) in the ocean if we consider the deep water circulation up to 4000m. Only if we will take only the surface layer circulation up to the thermocline (~1000m), the resident time is still long (~10^{2-3} years). Though large uncertainties in the estimation of underground water volume and its exchange rates to other categories, the resident time is also longer in deep underground where waters do not appear in the surface as the river runoff. By contrast, the atmosphere has very short resident time (~ 10 days). In other words, there are 10-20 recycles of the freshwater in the atmosphere. These mean resident times in the categories indicate that the climate as long-term mean state of atmospheric variables is mainly determined by extra-forcing such as the ocean and land rather than in several inner processes.

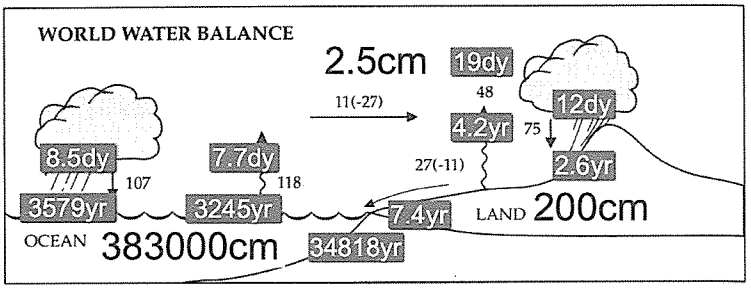

Figure 2.5 Schematic figure showing mean depth of the fresh water in the category (bold black), annual exchange rate of the fresh waters between the categories (values with arrows) , and mean resident time estimated from those values (bold white) . [Modified from Global Physical Climatology, Hartmann 1994].

2.2.3 Moisture role in the global energy balance

As documented in the previous section, heat capacity is larger in the ocean than in the atmosphere. Specific heat and density are 4.2×10^3 $Jkg^{-1}K^{-1}$ and 1.0×10^3 kg m^{-3} for water, 1.0×10^3 $Jkg^{-1}K^{-1}$ and 1.28 kg m^{-3} for air. Hence the heat capcity of the ocean is 3.2×10^3 times larger than that of the atmosphere. This difference in the heat capacity can induce changes of amplitudes in annual cycles of surface air temperature; small (large) amplitudes of the cycle near (far from) the ocean under the same solar forcing on the same latitude.

Heat capacity is not the only factor that reduce temperature difference between night and day, or between winter and summer. Water vapors (H_2O) work as one of the major greenhouse gases in the radiative processes as like carbon dioxside (CO_2) and ozone (O_3). As stated in the previous section, the total amount of water vaper tends to be larger near the ocean. This indicates that radiative forcing by water vapors is active near the ocean, too. Increased water vapor enhance emissions of infrared radiation from the atmosphere. At the surface energy balance, emissions of infrared radiation from the atmosphere (mainly from the troposphere) are largest (89 unit) (Figure 2.6). This value is closely twice of the solar heating at the surface (50 unit). Since these values are based on the annual mean, radiative forcing from the atmosphere become more important during night and winter when the solar heating is less active.

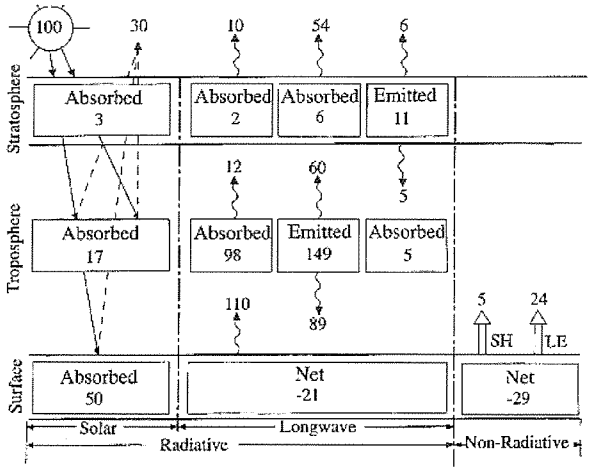

Figure 2.6 Schematic figure of global energy balance. Units are percentages of the global-mean solar heating (100=342 Wm^{-2}). [From Global Physical Climatology, Hartmann 1994].

2.2.4 Climatological surface air temperature and ocean condition

At the top of the atmosphere, the annual cycle of the solar heating is mostly equatorial anti-symmetric due to the slight tilt of a rotation axis of our planet to the orbiting surface (not shown). However, climatological surface air temperature is zonal and equatorial asymmetric. In other words, the land-sea contrast along the same latitude of surface air temperature is very much enhanced in the Northern Hemisphere than in the Southern Hemisphere (Figure 2.7).

In January, winter hemisphere has a large land-sea contrast of surface air temperature. Over the land region far from the ocean, a small heat capacity of the land surface and the overlying less moist atmosphere may induce strong cooling, and therefore very low surface air temperature the below $-40^{\circ}C$ (this is the climatological value!) is formed in the central North America (Canadian territory) and the Northeastern Eurasian continent (Siberia region). Even if we look at only the ocean, a zonal

asymmetry is still distinct in January as stated in the previous section. There is a sharp meridional gradient in the western boundary, while the meridional gradient is weak in the eastern boundary. Those gradients in either side of the domain are associated with the surface temperature gradient over the land nearby.

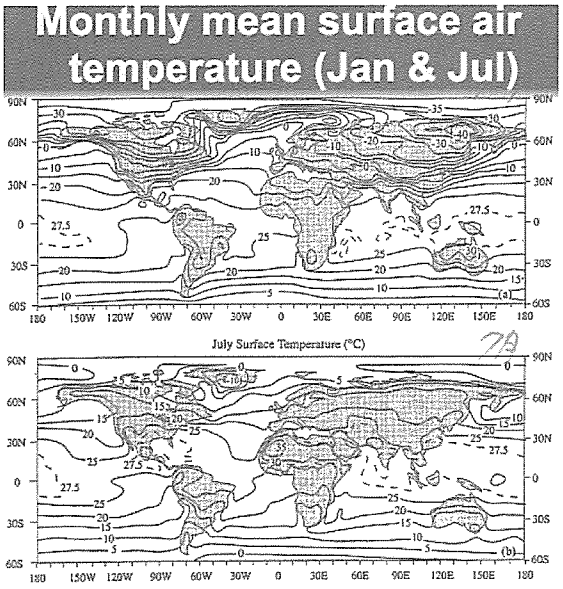

Figure 2.7 Climatological surface air temperature global of January (upper panel) and July (lower panel). [From Global Physical Climatology, Hartmann 1994].

The zonal asymmetric surface air temperature in the Northern Hemisphere is relative weak in summer (July) than in winter (January), probably due to the fact that the strong solar heating rather than the ocean currents is the major process in the summertime SST formation. The zonal asymmetry of the surface air temperature is nearly always weak in the Southern Hemisphere. A larger coverage of the ocean in the Southern Hemisphere reduce the land-sea contrast and an amplitude annual cycle, compared to those in the Northern Hemisphere (Figure 2.8). In addition, the circumpolar circulation in the Southern Ocean may contributes to reduce a zonal asymmetry.

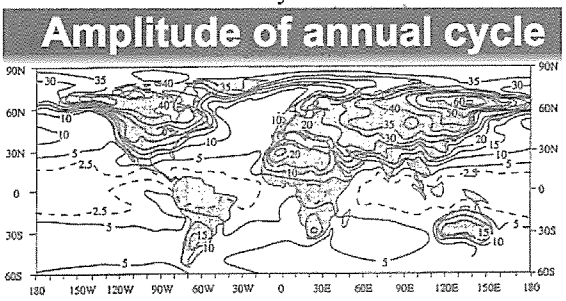

Figure 2.8 Climatological amplitude of annual cycle in surface air temperature [From Global Physical Climatology, Hartmann 1994].

Thus the dynamical and physical properties of the ocean (ocean currents, large heat capacity, radiative active water vapor source, and so on) are essential to determine the current climatological climate condition. Since the ocean conditions are actually unstable rather than always stable, the ocean variability is very much associated with the climate variability on the time scales from the seasonal to thousands years.

This document is a summary of lecture 2 in the 16th International Hydrolocal Programme Training Course -Oceanographic basis- on November 27, 2006 at Hydrospheric Atmospheric Research Center, Nagoya University.

Chapter 3

Ocean Circulation

Toshio Suga
Department of Geophysics
/ Graduate School of Science, Tohoku University
6-3 Aoba, Aramaki, Aoba-ku, Sendai-shi 980-8578, JAPAN
e-mail: suga@pol.geophys.tohoku.ac.jp

3.1 Introduction

The Ocean has a rich variety of the stratified structure of physical, chemical and biological parameters, including temperature, salinity, density, dissolved oxygen, nutrients, *etc.* (Fig. 3.1). The structure is maintained through both the atmosphere-ocean exchanges of heat, fresh water, momentum and other materials and the circulation/mixing of the ocean. Accordingly this stratified structure varies in time and space due to changes in those processes. Since those processes are components of the climate system, the oceanic structure varies according to climate conditions. On the other hand, the ocean actively affects on the climate condition through its heat and fresh water transport and storage.

Understanding of large scale circulation and mechanism to maintain the large scale structure of the ocean is essential to understand the ocean's role in the climate. The goals of this chapter is

(1) to understand basic dynamics of large scale ocean circulation (Section 3.2),
(2) to grasp the outline of the global ocean circulation (Section 3.2),
(3) to grasp the outline of major water masses in the Pacific Ocean (Section 3.3), and

to have a rough idea of a fundamental mechanism maintaining subsurface temperature (T) and salinity (S) structure (Section 3.3).

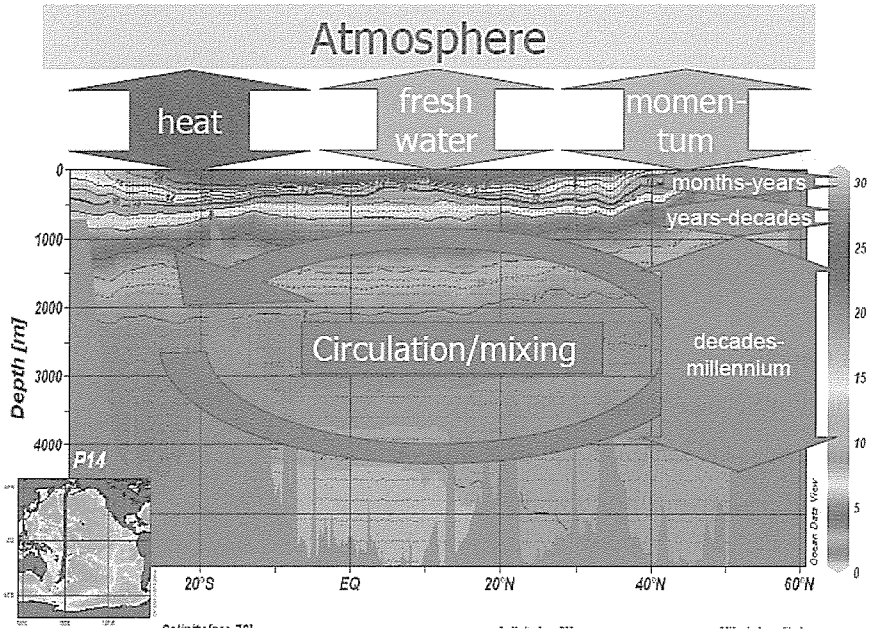

Figure 3.1 Schematic diagram to show the factors to maintain/change the stratified structure of the ocean and typical time scale of their variability for three depth ranges. Background is the vertical section of temperature along 179°E, adopted from"*eWOCE* - Electronic Atlas of WOCE Data" (http://www.ewoce.org/).

3.2 Large scale ocean circulation

3.2.1 Scales of circulation to be considered

In the ocean, the flow filed consists of phenomena on various time and space scales, including periodic tidal flow, variable flow associated with mesoscale eddies, swift currents such as the Kuroshio, *etc.* The ocean circulation we deal with here is one that emerges when the flow field is averaged over several months or longer periods and that extends over an oceanic to global scale (10^3-10^4 km), so-called "ocean general circulation". The ocean general circulation is not only an interesting subject of oceanographic research but also that of climate research because the associated transport of heat, fresh water and other materials plays an important role in the climate system.

3.2.2 Geostrophic current

General circulation, or large scale circulation, is almost in geostrophic equilibrium in which the Coriolis force acting on the water is balanced by a horizontal pressure gradient force. Geostrophic equilibrium is expressed in terms of equations of motion as

$$-fv = -\frac{1}{\rho}\frac{\partial p}{\partial x} \tag{3.1}$$

$$fu = -\frac{1}{\rho}\frac{\partial p}{\partial y} \tag{3.2}$$

where x and y are eastward and northward axes, u and v are eastward and northward velocity components, p, ρ, and f are pressure, density and Coriolis parameter, or in the vector form,

$$\mathbf{k} \times f\mathbf{v} = -\frac{1}{\rho}\nabla p \tag{3.3}$$

where $\mathbf{k}$, $\mathbf{v}$, and ∇ are vertical unit vector, horizontal velocity vector and horizontal gradient operator.

As an example, surface geostrophic current associated with raised sea surface in the Northern Hemisphere is shown in Fig. 3.2. Geostrophic current flows along an isobaric contour. Pressure is higher to the right of the current direction.

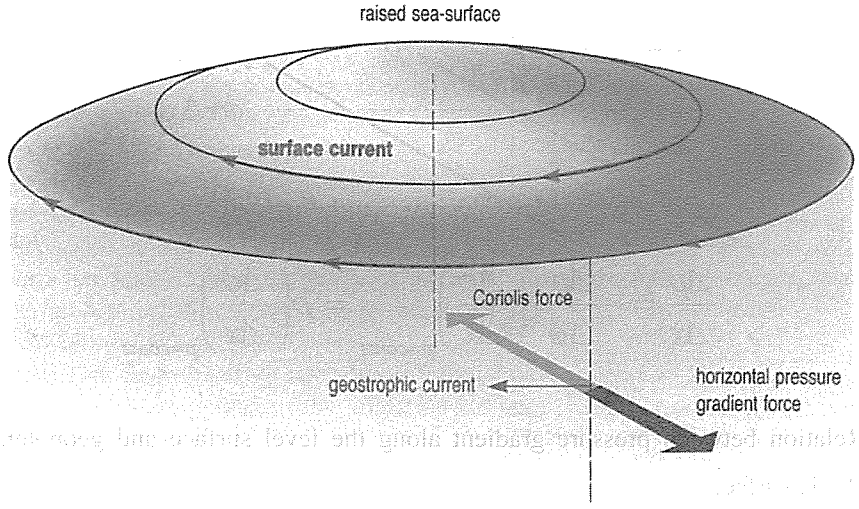

Figure 3.2 Surface geostrophic current associated with raised sea surface in the Northern Hemisphere, adopted from Open University (1989).

3.2.3 Pressure distribution in the ocean

Since large scale circulation is almost in geostrophic equilibrium, if we know pressure distribution on a level surface, we know the geostrophic current, that is, large scale circulation on the surface. In practice, the pressure distribution is described as height distribution of an isobaric surface.

Using geopotential as a measure of height,

$$d\phi = gdz$$

or

$$g = \frac{d\phi}{dz}$$

where g and ϕ are gravitational acceleration and geopotential, hydrostatic equation

$$\frac{\partial p}{\partial z} = -\rho g$$

is expressed as

$$\frac{\partial p}{\partial \phi} = -\rho \,.$$

Accordingly, pressure gradient along the level surface is expressed by geopotential gradient along the isobaric surface as

$$\nabla p = -\frac{\partial p}{\partial \phi}\nabla_p \phi = \rho \nabla_p \phi \tag{3.4}$$

where ∇_p is an gradient operator along an isobaric surface (Fig. 3.3).

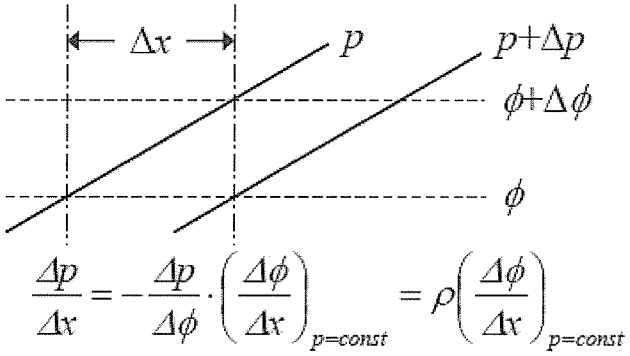

Figure 3.3 Relation between pressure gradient along the level surface and geopotential gradient along the isobaric surface.

Pressure distribution expressed as geopotential distribution on an isobaric surface is used to describe geostrophic currents. From (3.1), (3.2), (3.3) and (3.4), geostrophic currents are expressed as

$$\mathbf{k} \times f\mathbf{v} = -\nabla_p \phi$$

or

$$-fv = -\left(\frac{\partial \phi}{\partial x}\right)_{p=const}$$

$$fu = -\left(\frac{\partial \phi}{\partial y}\right)_{p=const} \,.$$

Here geopotential of an isobaric surface is obtained from observation of density, or temperature and salinity, as a function of pressure,

$$\phi = -\int_{p_0}^{p} \frac{1}{\rho(T,S)} dp$$

where p_0 represents reference pressure surface on which geopotential is assumed to be constant, or

"level of no motion".

Two examples of pressure distribution in the ocean as expressed as geopotential distribution of an isobaric surface are shown. The first example is that at the sea surface or the 0-dbar (1 dbar = 10^4 Pa) surface (Fig. 3.4). The contours in Fig. 3.4 actually represent "steric height" (x10 m^2s^{-2}), which is an offset version of geopotential. 10 m^2s^{-2} in steric height almost corresponds to 1 m in geometric height so that mumerical values in Fig. 3.4 are equivalent to heights in meter. Amplitude of spatial variation is ~1 x 10 m^2s^{-2}, or 1 m. Geostrophic current flows along the contours, with higher values to the right (left) in the Northern Hemisphere (Southern Hemisphere). More closely-spaced contours mean faster currents. The other example is the geopotential distribution at 4000-db surface or a depth of approximately 4000 m (Fig. 3.5). Amplitude of spatial variation is 0.01-0.1 x 10 m^2s^{-2}, or 0.01-0.1 m. Geostrophic currents at this surface are much slower than those at the sea surface.

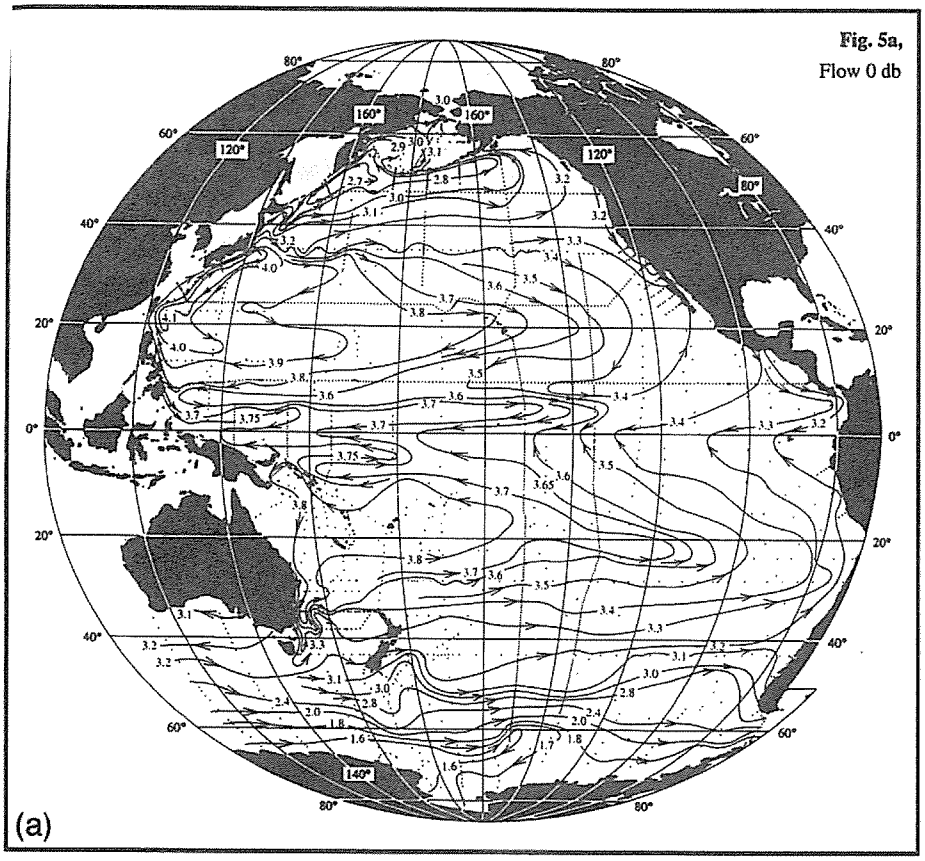

Figure 3.4 Adjusted steric height at 0 db (10 m^2s^{-2} or 10 Jkg^{-1}) adopted from Reid (1997).

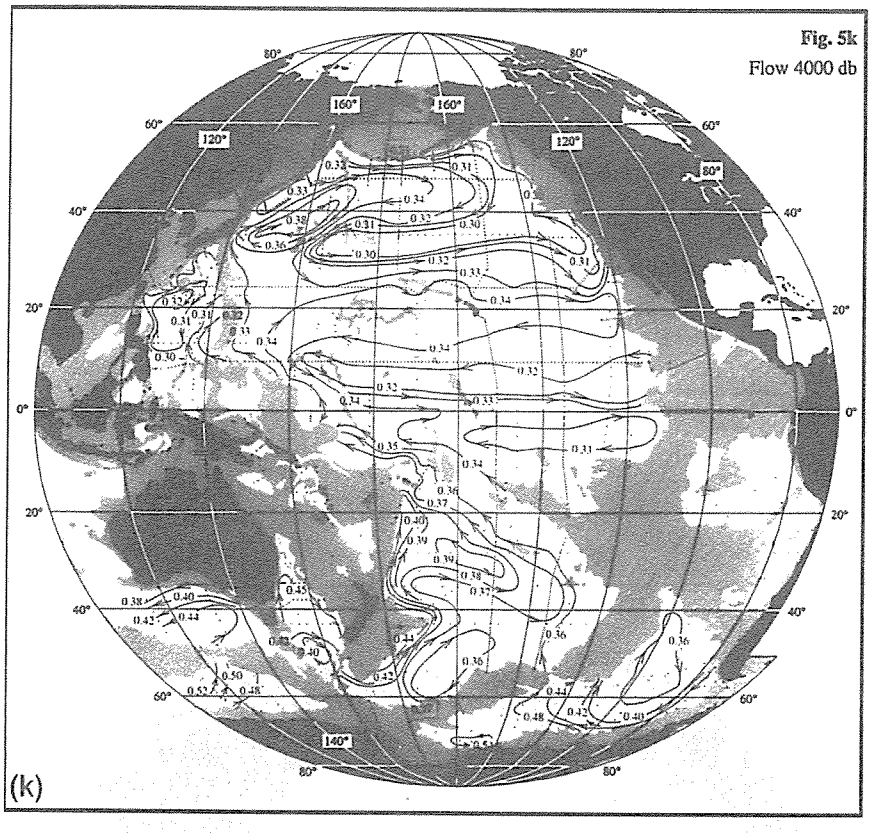

Figure 3.5 Adjusted steric height at 4000 db (10 m^2s^{-2} or 10 Jkg^{-1}) adopted from Reid (1997).

3.2.4 Driving forces

Since large scale circulation is almost in geostrophic equilibrium, causes of pressure distribution are regarded as driving forces of ocean general circulation. There are two types of such causes: "buoyancy supply" and "wind stress". Density of sea water changes through buoyancy gain or loss due to heating/cooling and evaporation/precipitation at the sea surface and mixing with water of different density. Distribution of buoyancy supply thus gives rise to distribution of density in the ocean. Since the pressure at a given locale in the ocean is essentially determined by the weight of the water above it, the density distribution causes the pressure distribution of the ocean. Therefore buoyancy supply is regarded as a driving force of the ocean circulation. On the other hand, wind stress, frictional force imposed by the surface wind, causes distribution of sea surface height. Distribution of the sea surface height also gives rise to the pressure distribution below that. Wind stress is thus regarded as another driving force of the ocean circulation.

How buoyancy supply causes pressure distribution and geostrophic current is illustrated in Fig. 3.6. Suppose, for instance, a part of the ocean consists of homogeneous water with the flat surface. In such a case, there is no horizontal pressure gradient. Now, if cooling and/or evaporation occur at the limited location of its surface, the water there loses buoyancy, becomes heavier and sinks. Suppose, as a result, a two-layer structure is formed: the upper lighter layer ("surface water") and

the lower heavier layer ("deep water"). Suppose the surface layer is maintained by buoyancy supply due to surface heating. Mixing of deep water with surface water continuously occurs, which causes buoyancy gain (loss) of the deep (surface) water. After all the processes reach the steady state, the interface between the deep water and the surface water can be tilted. In such a case, there is a horizontal pressure gradient in the deep layer. In the steady state, the pressure gradient should be balanced with the Coriolis force accompanied by the geostrophic current. Circulation driven by buoyancy supply in such a way is called thermohaline* circulation.

*Derivation is from *thermo-* for heat and *-haline* for salt.

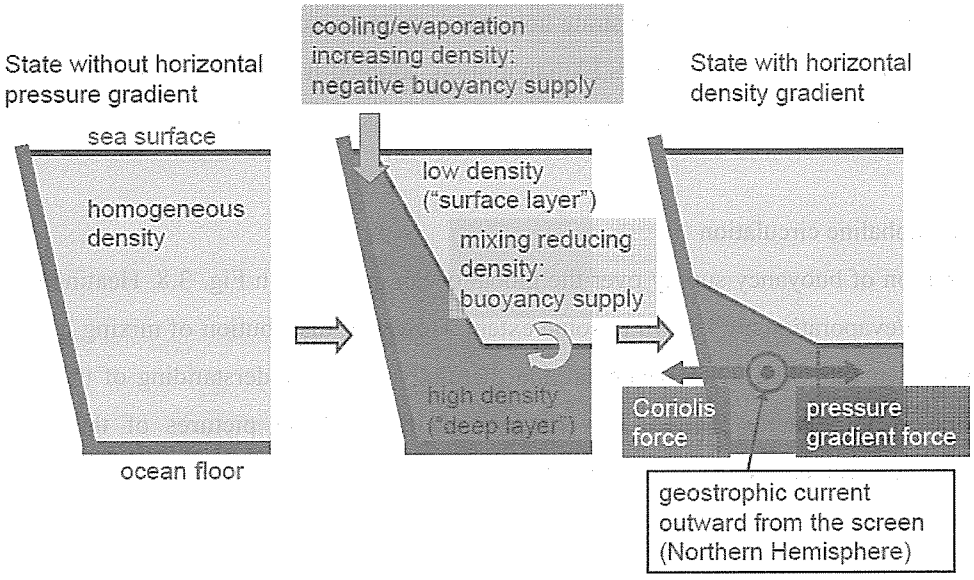

Figure 3.6 Schematic diagram to illustrate how buoyancy supply causes horizontal pressure gradient and geostrophic currents.

How wind stress causes pressure distribution and geostrophic current is illustrated in Fig. 3.7. The wind stress causes the near-surface flow called Ekman motion. Detailed structure of the Ekman motion is not very relevant here. Instead, it is important to note that the vertical average of the Ekman motion, called Ekman transport, is at the right angle to the wind direction, to the right in the Northern Hemisphere. This is because the wind stress should be balanced with the Coriolis force on the whole layer of the Ekman motion, or Ekman layer, in the steady state. When the surface wind has a horizontal shear, convergence or divergence of the Ekman motion will occur. The convergence (divergence) gives rise to raised (depressed) sea surface, which causes the horizontal pressure gradient below. The pressure gradient should be balanced with the Coriolis force accompanied by the geostrophic current. Circulation driven by wind stress in this manner is called wind-driven circulation.

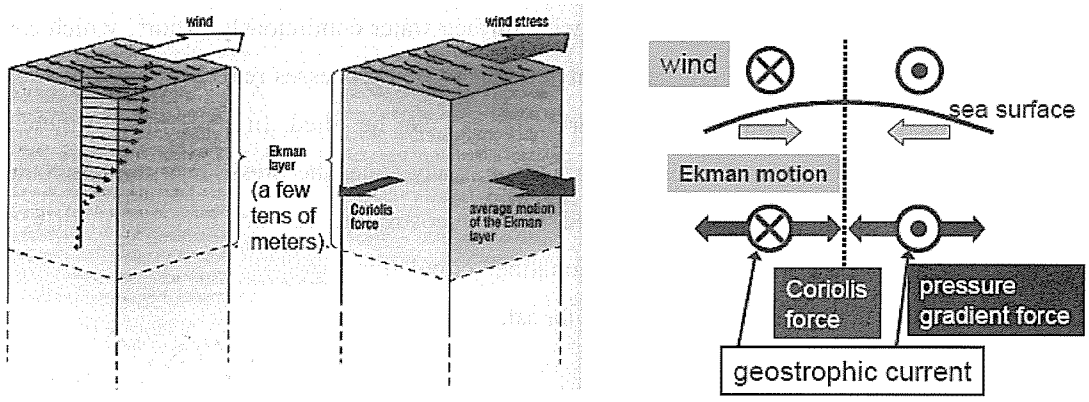

Figure 3.7. Schematic diagram to illustrate how wind stress causes horizontal pressure gradient and geostrophic currents. Left panel shows Ekman motion, adopted from Open University (1989). Right panel shows the relation between the direction of wind stress and that of geostrophic currents.

3.2.5 Thermohaline circulation

Distribution of buoyancy supply over the global ocean is shown in Fig. 3.8. Heating/cooling and precipitation/evaporation are known to some extent. However, distribution of mixing in the ocean is still not known very well. Our dynamical and thermodynamical understanding of the themohaline circulation is thus rather limited. Nevertheless we have global pictures of the thermohaline circulation constructed from the limited observations of water properties and also direct current measurements.

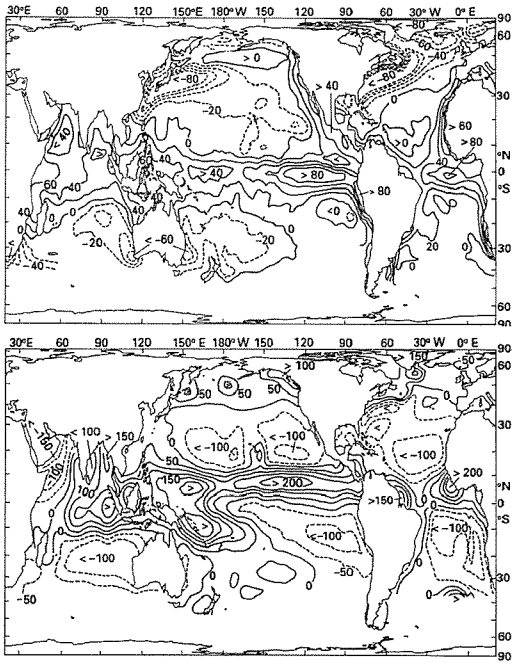

Figure 3.8 Surface heat flux in W m^{-2} and precipitation minus evaporation in cm/year, adopted from Tomczak and Godfrey (1994). Data from Oberhuber (1988).

Figure 3.9 shows a conceptual diagram of the global thermohaline circulation. Although the diagram is well known as an ocean conveyor belt, it is an extremely simplified schematic view. More realistic pictures can be obtained if we divide the ocean into several layers. Three- or four-layer approximation of the ocean water column (Fig. 3.10) is useful to present many important features of the global thermohaline circulation. For example, Figure 3.11 shows the recent schematics of the global thermohaline circulation with the four layers: surface layer, intermediate layer, deep layer and bottom layer. Figure 3.12 gives a plan view of the same schematics with expressed by three layers, combining the surface layer and the intermediate layer into a single layer.

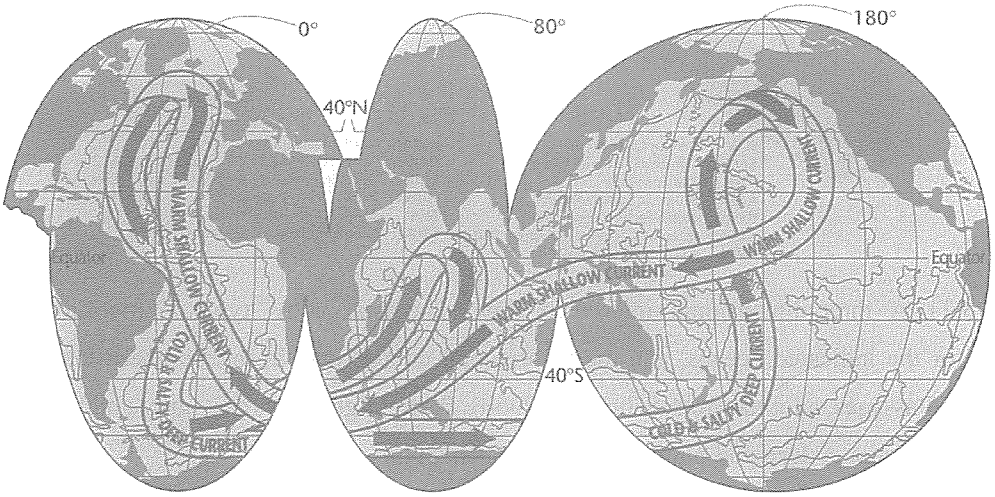

Figure 3.9 A two-layer thermohaline conveyor belt summary taken schematically from Broecker (1987) by Schmitz (1995), adopted from Schmitz (1996a).

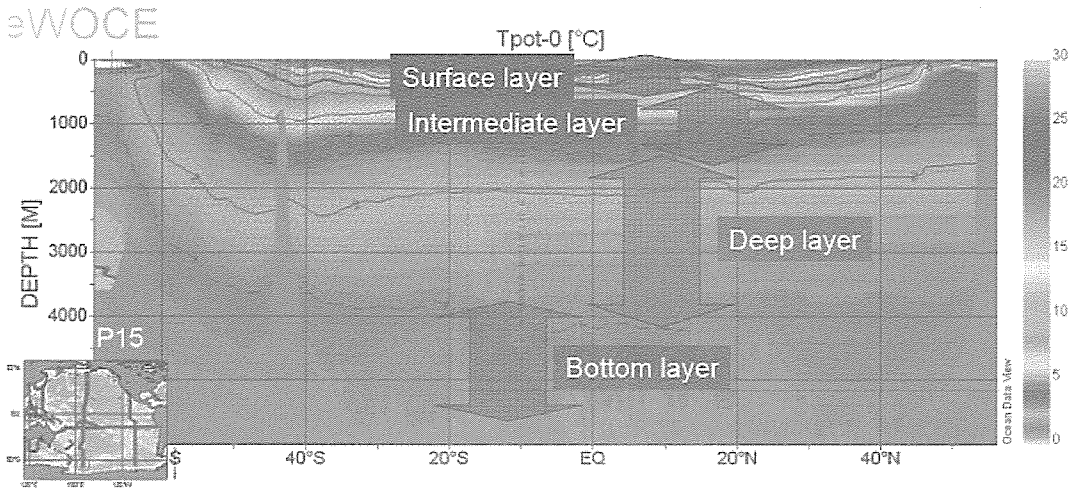

Figure 3.10 Four-layer approximation of the ocean water column. Background is the vertical section of temperature along 165°W, adopted from"*eWOCE* - Electronic Atlas of WOCE Data" (http://www.ewoce.org/).

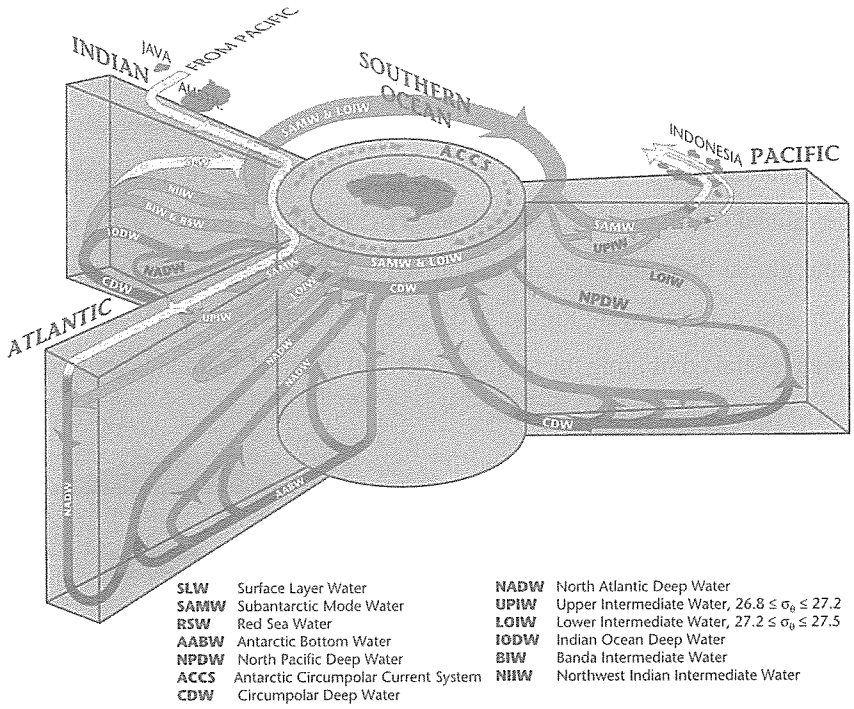

Figure 3.11 A three-dimensional interbasin flow schematic with "typical" meridional-vertical sections for the indicated oceans, and their horizontal connections in the Southern Ocean and the Indonesian Passages, adopted from Schmitz (1996b). White, light gray, dark gray and black indicate surface, intermediate, deep and bottom layers, respectively.

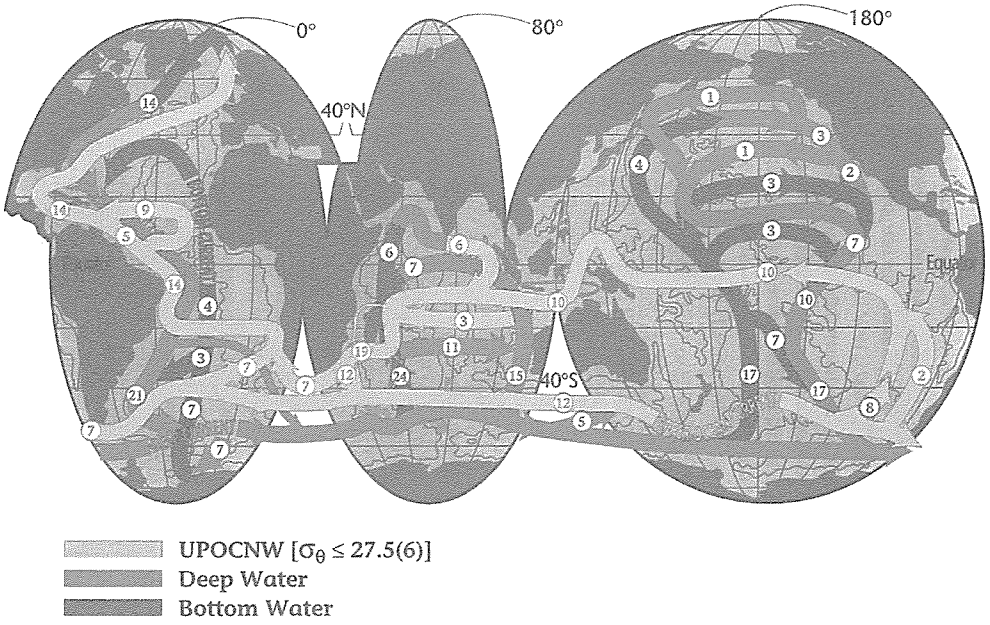

Figure 3.12 3-layer global interbasin exchange summary adopted from Schmitz (1996b). Surface and intermediate waters are combined into the upper water (UPOCNW). Numbers indicate transport in Sv (10^6 m^3 s^{-1})

3.2.6 Wind-driven circulation

Distribution of wind stress over the global ocean is shown in Fig. 3.13. Large scale anticyclonic and cyclonic wind stress patterns appear in each ocean basin. The former (latter) causes convergence (divergence) of the Ekman transport, which leads to raised (depressed) sea surface inside the wind stress pattern. The basin-wide anticyclonic (cyclonic) circulation caused by the mid-latitude anticyclonic (cyclonic) wind stress pattern is called subtropical (subpolar) gyre. The schematic distribution of the surface circulation in the world ocean is presented in Fig. 3.14. The subtropical and subpolar gyres are identified in the world ocean. The basin-scale circulation in the upper kilometer is reasonably regarded as wind-driven circulation.

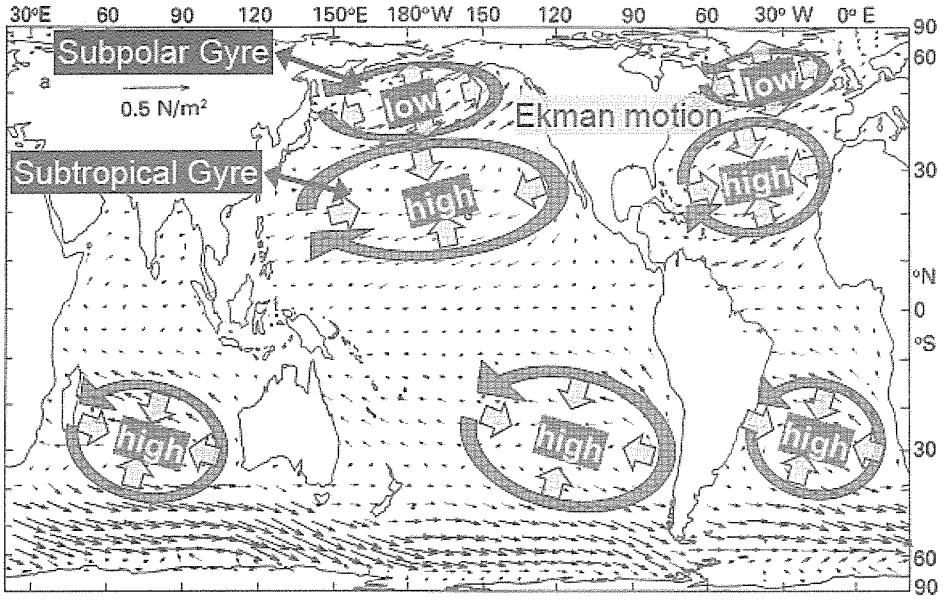

Figure 3.13 Annual mean wind stress over the world ocean adopted from Tomczak and Godfrey (1994). Data from Trenberth *et al.* (1989). Superimposed are anticyclonic and cyclonic wind stress patterns and associated sea surface height changes.

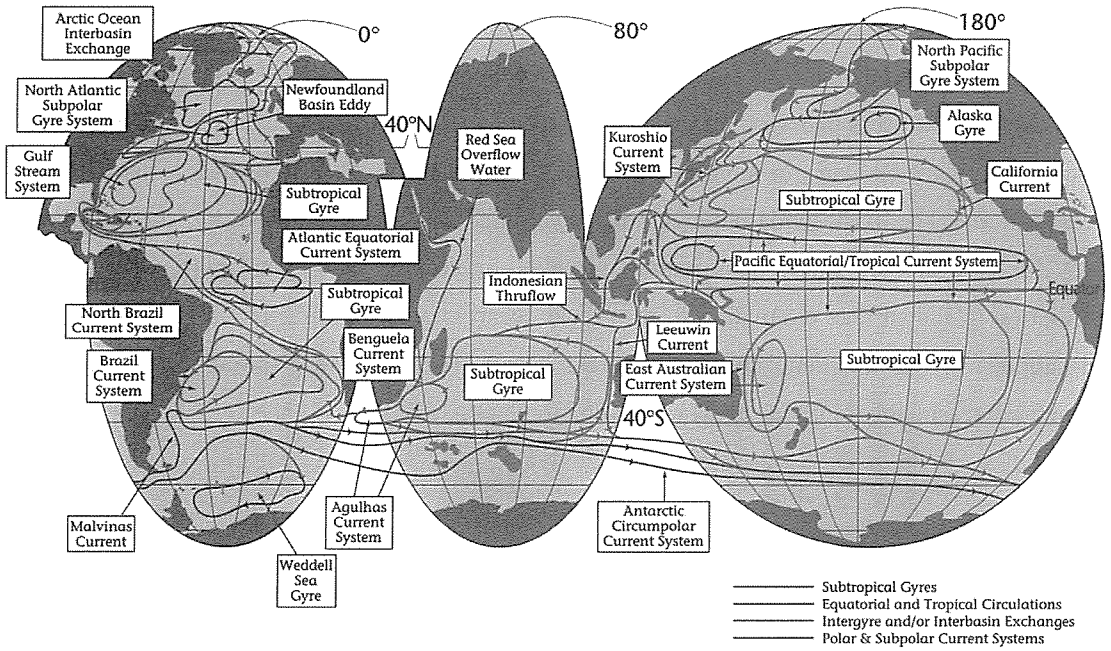

Figure 3.14 A global map schematically identifying the location and nomenclature for most major upper ocean flow patterns and the connections between these current system adopted from Schmitz (1996b).

3.2.7 Summary

Buoyancy supply causes themohaline circulation through formation of density distribution. The thermohaline circulation is slow global three-dimensional circulation. The time scale of the circulation is from several decades to a couple of thousands years. On the other hand, wind stress causes wind-driven circulation through formation of sea surface height distribution. The wind-driven circulation is fast basin-scale surface circulation. The circulation time scale is from several years to a couple of decades. One of the important consequences of the general circulation is transport of heat, fresh water, etc.

3. 3 Water mass formation in the Pacific Ocean

3.3.1 What is a water mass?

A water mass is one of the fundamental concepts in oceanography. Nevertheless, the usage of the term "water mass" is sometimes ambiguous. Here we adopt the definition of this term by Tomczak (1999); a water mass is a body of water with a common formation history, having its origin in a particular region of the ocean. Water masses have been used as tools to trace circulation and ventilation processes of the ocean. In the following subsection, major water masses in the Pacific Ocean are presented with brief comments on how they are useful to describe the ocean circulation.

3.3.2 Major water masses in the Pacific Ocean

Water masses are usually identified by combinations of several water properties such as temperature, salinity, dissolved oxygen, *etc.* Detailed and quantitative discussion of water masses requires analysis using multiple properties. To quickly grasp the outline of major water masses in the Pacific Ocean, only a single property characterizing each water mass is highlighted below.

Major features of bottom and deep water masses are illustrated by the vertical section of dissolved oxygen (Fig. 3.15). Dissolved oxygen of the sea water decreases with time after leaving the sea surface due to biogeochemical processes. The oxygen content is highest in the surface layer (~0-500 m) because it is directly in contact with the atmosphere. The bottom layer (~4000-6000 m) has higher dissolved oxygen than the deep layer (~1500-4000 m) and the intermediate layer (~500-1500 m) because newer bottom water, called Circumpolar Deep Water (CDW), enters to the Pacific Ocean from the Southern Ocean. CDW with higher oxygen from the south is transformed into older North Pacific Deep Water (NPDW) with lower oxygen, which flows back to the south.

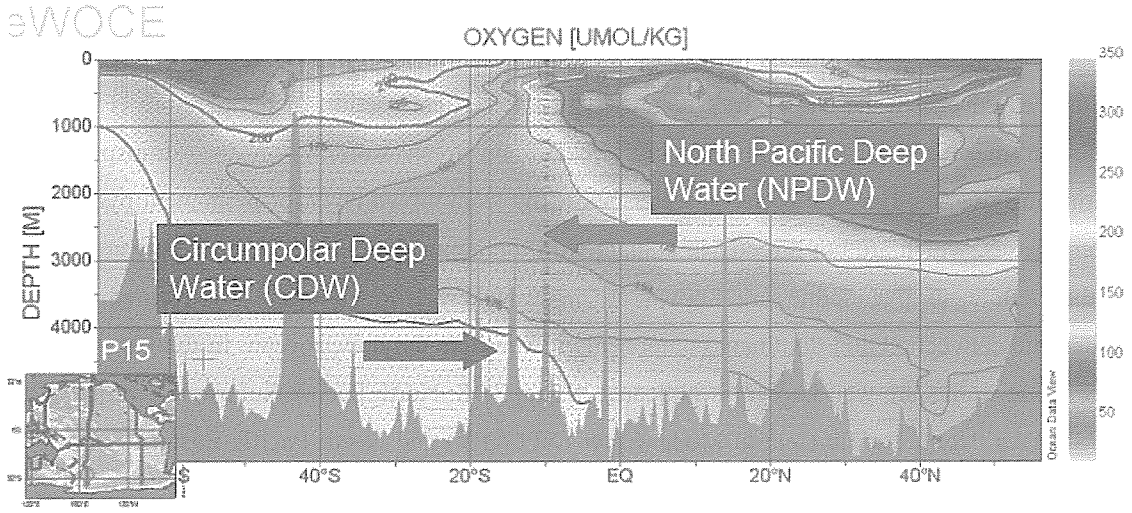

Figure 3.15 Major deep and bottom water masses in the Pacific Ocean. Background is the vertical section of dissolved oxygen along 165°W, adopted from"*eWOCE* - Electronic Atlas of WOCE Data" (http://www.ewoce.org/).

Intermediate water masses and their spreading are illustrated clearly by the vertical section of salinity (Fig. 3.16). Relatively fresh subpolar surface water is cooled in winter and becomes heavier. However, because of its low salinity, it is not as heavy as deep water masses. As a result, intermediate water masses spread over the intermediate layer to form intermediate salinity minimum layer in each hemisphere. North Pacific Intermediate Water (NPIW) spreads at the depth of 500-1000 m from the north. On the other hand, Antarctic Intermediate Water (AAIW) spreads at the

depth of 500-1500 m from the south.

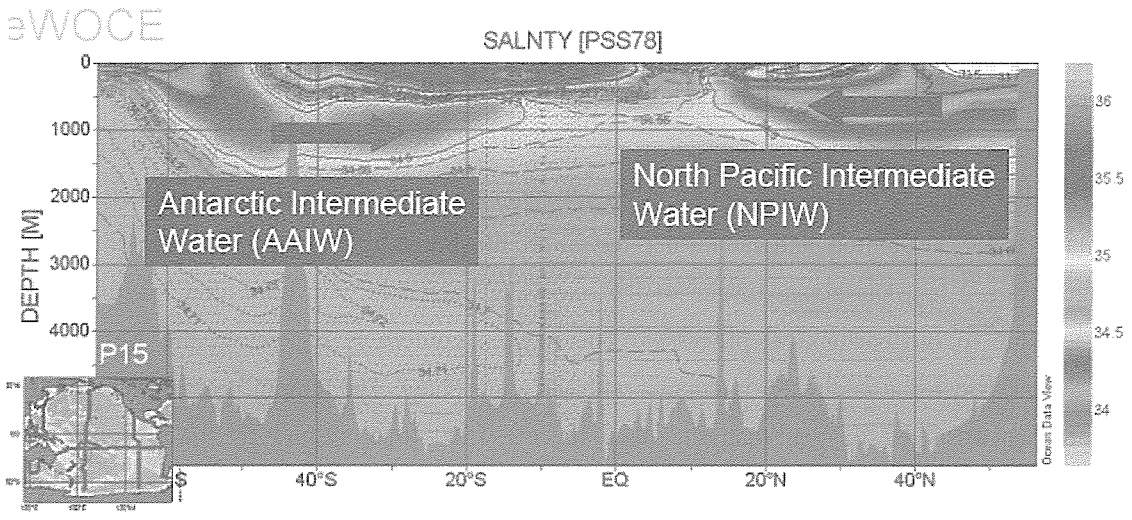

Figure 3.16 Major intermediate water masses in the Pacific Ocean. Background is the vertical section of salinity along 165°W, adopted from "*eWOCE* - Electronic Atlas of WOCE Data" (http://www.ewoce.org/).

Some of surface water masses are identified in the vertical section of temperature (Fig. 3.17). Water in the local mixed layer exchanges heat, and fresh water, with the atmosphere and continuously varies. Here we focus on water below the local mixed layer, or permanent pycnocline* water masses, which are not directly in contact with the atmosphere. Relatively thick water masses in the permanent pycnocline are known as mode waters. Mode waters are formed by deep wintertime convection and dominant components to ventilate the upper ocean. In the North Pacific, three mode waters are well known as indicated in Fig. 3.18: North Pacific Subtropical Mode Water (NPSTMW), North Pacific Central Mode Water (NPCMW) and North Pacific Eastern Subtropical Mode Water (NPESTMW).

*A permanent pycnocline is a pycnocline which the local mixed layer does not reach even in late winter.

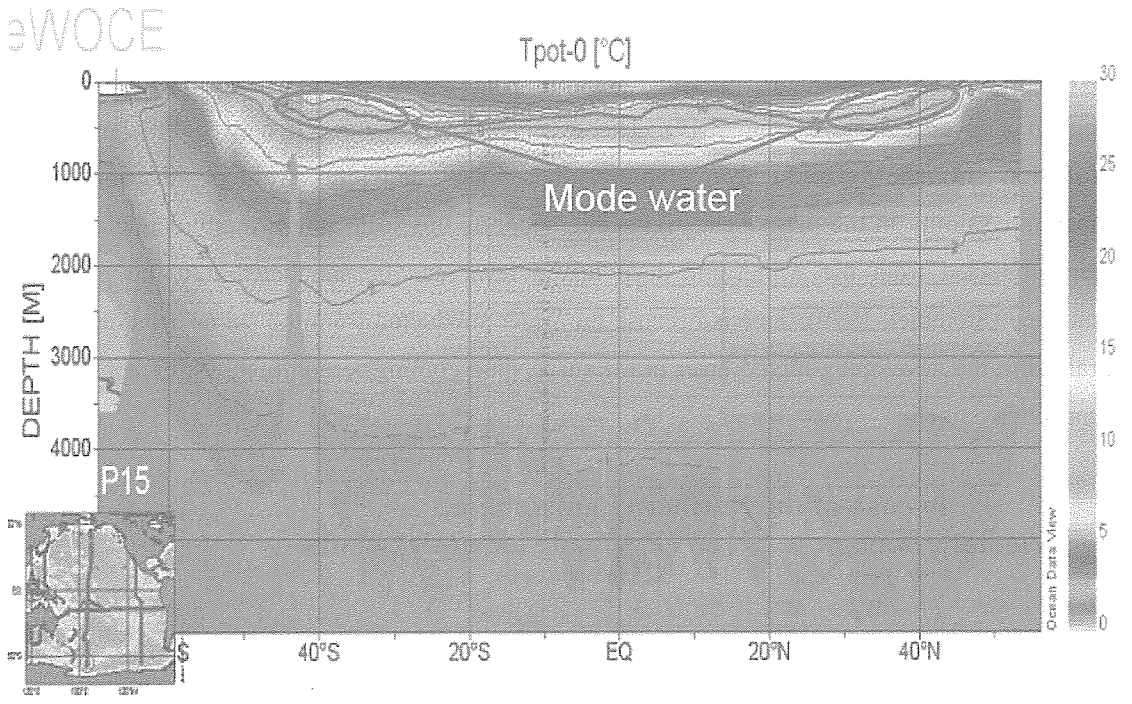

Figure 3.17 Mode waters in the Pacific Ocean. Background is the vertical section of temperature along 165°W, adopted from"*eWOCE* - Electronic Atlas of WOCE Data" (http://www.ewoce.org/).

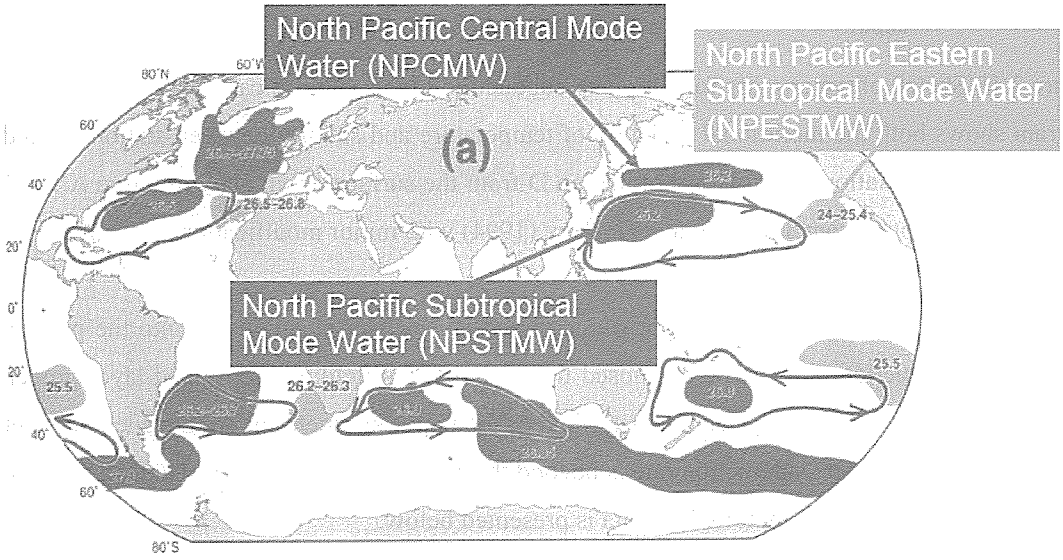

Figure 3.18 Mode waters in the world ocean adopted from Hanawa and Talley (2001). Mode waters in the North Pacific are highlighted.

3.3.3 Formation of the permanent pycnocline water

Water masses in the permanent pycnocline are maintained by subduction of mixed layer water along an isopycnal surface (Fig. 3.19). The observed correspondence between the meridional distribution of the mixed layer temperature/salinity and the vertical distribution of temperature/salinity in the permanent pycnocline supports this idea. Interestingly enough only the water subducted from the wintertime deep mixed layer can be subducted into the permanent pycnocline (Stommel, 1979). This is because the water subducted from the summer mixed layer is entrained in the developing mixed layer in the succeeding cooling season before it escapes into the permanent pycnocline.

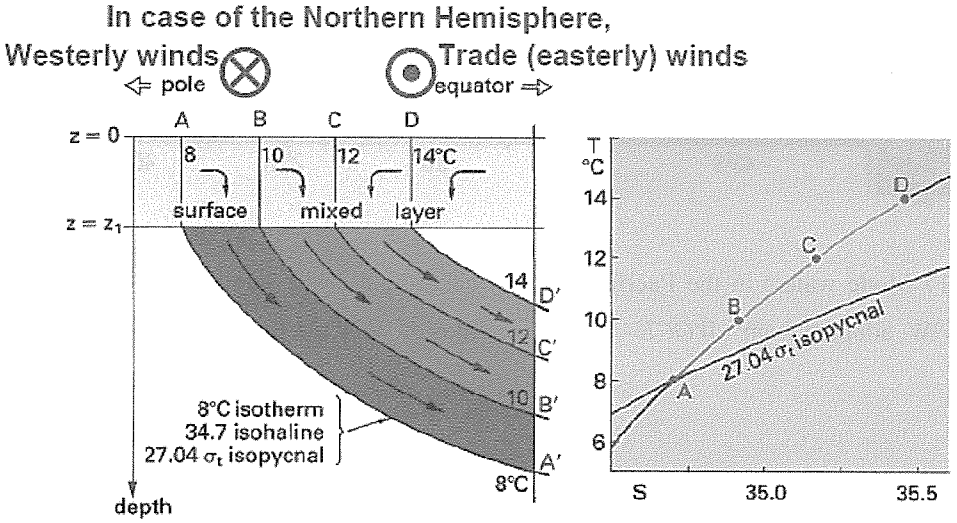

Figure 3.19 Sketch of water mass formation by subduction in the Subtropical Convergence. The T-S diagram shows both the meridional variation of temperature and salinity between stations A and D, and the vertical variation equatorward of station D from the surface down along the line A'B'C'D'. The figure is adopted from Tomczak and Godfrey (1994) with minor modification.

Subduction rate is defined as a rate at which mixed layer water is subducted into the permanent pycnocline. Subduction rate can be diagnosed from wind stress field, winter mixed layer properties (depth, temperature and salinity) and density field of the upper kilometer or so. Detailed description of the method to calculate subduction rate is beyond the aims of this chapter. In stead, an example of such estimation based on climatological data is presented below.

Figure 3.20 shows the spatial distribution of the subduction rate superimposed on the contours of the winter mixed layer properties in the North Pacific. The subduction rate has large spatial variability. Large values of the subduction rates appear in the formation regions of mode waters, indicating that mode waters are dominant water masses contributing the permanent pycnocline. The renewal time of a water mass can be estimated by diving the volume of the water mass by the

corresponding subduction rate. According to such estimation based on the subduction rate shown in Fig. 3.20, the renewal time of the permanent pycnocline water ranges from 2 years to 60 years or longer. Estimated renewal times are 2-4 years for NPESTMW, 2 years for the lighter part of NPSTMW, 5-9 years for the denser part of NPSTMW, 10-20 years for the lighter part of NPCMW, 20-30 years for the middle part of NPCMW and > 60 years for the denser part of NPCMW.

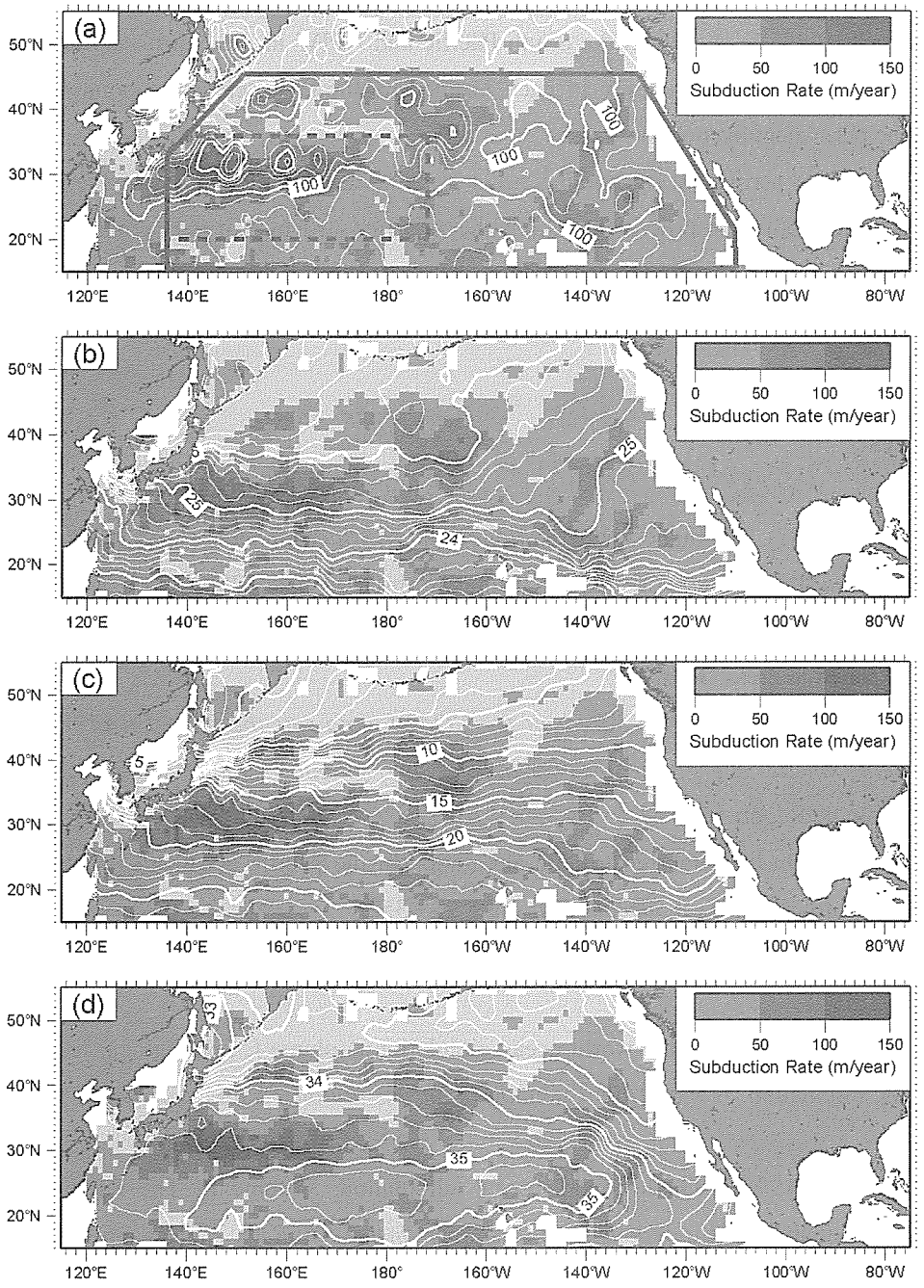

Figure 3.20 Subduction rate (gray scale) superimposed on the winter mixed layer properties (contours): (a) depth (m), (b) density (kg m^{-3}), (c) temperature (°C) and (d) salinity (PSS-78), adopted from Suga *et al.* (2007).

3.3.4 Summary

Major water masses in the North Pacific are CDW and NPDW in the bottom and deep layer, AAIW and NPIW in the intermediate layer, and mode waters (NPSTMW, NPCMW, NPESTMW) in the surface layer. High dissolved oxygen of CDW indicates its relatively recent ventilation compared to the NPDW. AAIW in the South Pacific and NPIW in the North Pacific form a clear intermediate salinity minimum layer in each basin. The mode waters correspond to volumetric modes in the permanent pycnocline water.

Formation of the permanent pycnocline water is explained by subduction of the winter mixed layer water. The subduction process maintains the stratified structure of the permanent pycnocline. Based on the estimation of subduction rate in the North Pacific, the renewal time of the permanent pycnocline water ranges from 2 years to 60 years or longer.

References

Broecker, W.S. (1987): The biggest chill, *National History Magazine*, **97**, 74-82, 1987.

Open University (2001): *Ocean Circulation*, Butterworth-Heinemann, 286pp.

Hanawa, K., and L. D. Talley (2001): Mode waters, *Ocean Circulation and Climate*, J. Church et al. Eds., Academic Press, 373-386.

Oberhuber, J.M. (1988): *An atlas based on the COADS data sat: the budget heat, buoyancy and turbulent kinetic energy at the surface of the global ocean*, Max-Planck-Institut für Meteorologie Report 15.

Reid, J.L. (1997): On the total geostrophic circulation of the pacific ocean: flow patterns, tracers, and transports, *Progress in Oceanograpy*, **39**, 263-352.

Schmitz, W.J., Jr. (1995): On the interbasin-scale thermohaline circulation, *Rev. Geophys.*, **33**, 151-173, 1995.

Schmitz, W.J, Jr. (1996a): On the world ocean circulation: Volume I, Some global features / North Atlantic circulation, *Woods Hole Oceanographic Institution Technical Report* , WHOI-96-03, 150pp.

Schmitz, W.J, Jr. (1996b): On the world ocean circulation: Volume II, The Pacific and Indian Oceans / A glabal update, *Woods Hole Oceanogr. Inst. Tech. Rept.* , WHOI-96-08, 241pp.

Stommel, H. (1979): Determination of water mass properties of water pumped down from the Ekman layer to the geostrophic flow below, *Proceedings of the National Academy of Sciences, USA*, **76**, 3051-3055.

Suga, T. Y. Aoki, H. Saito and K. Hanawa (2007): Ventilation of the North Pacific subtropical pycnocline and mode water formation, *Progress in Oceanography*, in press.

Tomczak, M. (1999): Some historical, theoretical and applied aspects of quantitative water mass analysis, *Journal of Marine Research*, **57**, 275-303.

Tomczak, M., and J.S. Godfrey (1994): *Regional oceanography: An introduction*, Pergamon, 422pp.

Trenberth, K.E., J.G. Olson and W.G. Large (1989): *A global ocean wind stress climatology based on ECMWF analysis*, NCAR Technical Note NCAR/TN-338+STR.

Chapter 4

Phytoplankton in the Ocean

Joji Ishizaka
Faculty of Fisheries, Nagasaki University
1-14 Bunkyo, Nagasaki, Nagasaki, 852-8521, JAPAN
e-mail: ishizaka@nagasasaki-u.ac.jp

4.1 Introduction

Phytoplankton composed of various kinds of microscopic unicellular organisms, are the major primary producers in the ocean. Primary production in the ocean is one of the most important biogeochemical processes, not only because it creates food for most of the animals in the ocean but also because it helps to transport materials, such as carbon, nitrogen, and phosphate. In this short lecture, first, definition of primary production and phytoplankton, second, measurements of primary production and its controlling factors, third, spatial distribution and forth, temporal variability will be discussed. More complete descriptions can be found in various textbooks, including Lalli and Parsons (1995), Mann and Lazier (2006), Falkowski and Raven (2007), etc.

4.2 Phytoplankton

Phytoplankton includes many groups of organisms (Table 4.1). Among them, cyanobacteria, diatoms, dinoflagellates and coccolithophorids are the major and most well known groups. Cyanobacteria are the prokaryotic phytoplankton which do not have nucleus, and other phytoplankters are eukaryotic organisms, which have a nucleus. Cyanobacteria are considered as one of the most abundant organisms in the world. Synecococcus and prochlorococcus are two of the newly found phytoplankton groups having small and round shape (2 to 0.7 μm diameter). However, now it is known to be extremely abundant in the open ocean. Trichodesmium, which makes visible (about 1 mm diameter) colonies (banded chains), sometimes forms red tide in tropical and subtropical coastal waters, and also known as a nitrogen fixer (can use molecular N_2 as a nitrogen source), and hence important for nitrogen limited marine ecosystem. Some of unicellular species and symbiotic species of this group are also known as nitrogen fixer.

Diatoms are one of the most well known phytoplankton groups because of it's abundance in both coastal and fresh waters. They often form long chains of larger cells (several tens to hundreds μm) with silicic shell, observable by light microscopy. It is also know as a dominant group in many of upwelling regions and seasonal blooms described in latter section. Because of their silicic cells, they require silicate as necessary nutrient for their growth.

Dinoflagellates are also one of the most abundant phytoplankton groups in coastal waters. Some of the species are well known as cause of red tide and/or harmful algal bloom, and some produce poison, which in turn leads to killing of fishes and even human diseases. They swim with the help of their flagella and often migrate vertically with the daily cycle. Some groups, having no photosynthetic pigments, are heterotrophic in nature, whereas some pigmented species exhibit both autotrophic and heterotrophic nature (mixotrophic).

Coccolithophorids are another special phytoplankton group, which have plates of calcium carbonate as shells, and sometimes, when in abundance, make water look white in colour (white water). Accumulation of their plates, in the sediment, over geological time scale had lead to formation of chalk. Because of their ability to form calcium carbonate plates, they have a special function in geochemical cycle. Molecular carbon dioxide is released by the formation of calcium carbonate.

Table 4.1 Phytoplankton groups (Common names are in the parenthesis)

Cyanobacteria (Blue-Green Algae)
Rhodophyceae (Red Algae)
Cryptophyceae (Crypotomonads)
Chrysophyceae (Chrysomonads, Silicoflagellates)
Bacillariophyceae (Diatoms)
Raphydophyceae (Chloromonads)
Xanthophyceae (Yellow-Green Algae)
Eustigmatophyceae
Prymnesiophyceae (Coccolithophorids, Prymnesiomonads)
Euglenophyceae (Euglenoids)
Prasinophyceae (Prasinomonads)
Chlorophyceae (Green Algae)
Dinophyceae (Dinoflagellates)

4.3 Primary Production

Phytoplankton is the major primary producer in vast area of ocean with the ability of photosynthesis. Primary production is a rate at which energy is stored in the form of organic substances, by photosynthetic or chemosynthetic action of producer organisms (autotrophic organisms). The production of basic organic materials supports all the heterotrophic organisms. Typically primary production including photosynthesis can be expressed as the conversion of carbon dioxide and water with energy to organic matter and oxygen. On the other hand, respiration conducted by both autotrophic and heterotrophic organisms is the decomposition (oxidize) of organic matter to obtain energy and waist carbon dioxide.

Photosynthesis

$6CO_2 + 12H_2O$ +Light Energy $\rightarrow 6CH_2O + 6H_2O + 6O_2$

Respiration

$6CH_2O + 6H_2O + 6O_2 \rightarrow 6CO_2 + 12H_2O$ + Energy

All the autotrophic organisms conduct respiration. Gross and net primary production are definded as the pure rate of primary production and the net gain rate excluding respiration, respectively.

Light is not the only energy source for primary production (photosynthesis), but there are some organisms (chemosynthetic bacteria), who can use chemical materials to extract energy for the production, called chemoshynthesis. For example, sulfur bacteria use H_2S as energy source.

4.4 Measurements, Estimation, and Controlling Factors of Primary Production

It is important to understand the difference between biomass and production. Biomass is mass of organisms and for marine organisms it is often expressed as per unit volume of water or per unit area as it is integrated through water column (Mass/Volume or Mass/Area). For phytoplankton, cell numbers can be used for biomass of single species; however, it is convenient to use amount of chlorophyll-a (such as μg-chl.a L^{-1} = mg-chl.a m^{-3}, mg-chl.a m^{-2}). This is because chlorophyll-a is the major photosynthetic pigment for all phytoplankton groups and because it is easy to measure as an indicator of sum of all phytoplankton groups which have different size and differentfunction.

Production is the rate of mass of carbon assimilated, and primary production is usually expressed in terms of Mass/Volume/Time (such as mg-C L^{-1} $hour^{-1}$, mg-C L^{-1} day^{-1}) or Mass/Area/Time (such as mg-C m^{-2} day^{-1}, g-C m^{-2} $year^{-1}$). It is also useful to calculate production per biomass known as assimilation number (P^B, mg-C mg-chl.a^{-1} day^{-1}, mg-C mg-chl.a^{-1} $hour^{-1}$) because it indicates activity of phytoplankton. P^B is controlled by environmental factors such as temperature, light and

nutrients, and species composition of the phytoplankton is also an important factor.

For biomass, cell numbers can be counted by microscopic observations after water sampling. Concentration may be necessary if the phytoplankton is not abundant. Epifluorescence microscopy, which can detect fluorescence from chlorophyll-a, is useful to discriminate autotrophic organisms from heterotrophic organisms. For small cyanobacteria, counting by a flow cytometer may be necessary because of the difficulty of the identification. Chlorophyll-a can be measured by spectrophotometrically, fluorometrically and more recently by High Performance Liquid Chromatography (HPLC). HPLC can also analyze pigments other than chlorophyll-a and be used to separate phytoplankton groups (chemotaxonomic analysis).

Primary production is usually measured by incubation method. Water samples are taken into transparent bottles and isotope of carbon (radioactive ^{14}C or non-radioactive ^{13}C) is added as bicarbonate ion. Then the bottles are incubated at the same depth of sampling (in situ method) or under similar light condition (simulated in situ method) for several minutes to a day. The samples are filtered onto a glass fiber filter and the amount of carbon changed to particulate matter is estimated from the amount of the isotope. Incubation method is a time consuming task and also expected various errors. Recently, some optical equipments to measure primary production have been developed, such as Fast Repetition Rate Fluorometer (FRRF); however its consistency with the incubation methods are under active research.

It is known that primary production significantly varied with time and space. What are the controlling factors of primary production? Since primary production of phytoplankton is based on photosynthesis, obviously light is one of the most important factors as energy source. Light penetrate only a hundred meters as maximum in water column for 3800m average depth of ocean.

On the other hand, nutrients are also an important factor for the primary production because it also limits phytoplankton growth as material source. Nitrogen and phosphorus are two major important atoms and nitrate (NO_3), nitrite (NO_2) and ammonium (NH_4) for nitrogen and phosphate (PO_4) for phosphorus are typical nutrients. Silicic acid (SiO_2) is important for diatom. Recently, iron is recognized as a very important micro-nutrient where macro-nutrients are abundant. Those regions are known as High Nutrient Low Chlorophyll (HNLC) region, such as eastern equatorial Pacific, Antarctic, North Pacific, and iron input from air may be important.

Temperature is also an important controlling factor of primary production because it controls most of the chemical reactions taking place inside plant cells. Temperature is also important because it is the major factor determining the density of water which controls both horizontal and vertical movement of water. The physical control of water mass is one of the major factors of spatial distribution of phytoplankton described in the next section.

Because of the difficulty of measuring primary production, spatial and temporal coverage of measurements of primary production is limited. Recently, satellite ocean color remote sensing can

measure sea surface chlorophyll-a from space at global scale with high spatial and frequent temporal resolution (Fig. 4.1). Now many models were developed to estimate primary production with sea surface chlorophyll-a, sea surface temperature (SST), and photosynthetically active radiation (PAR) measured from satellite (*i.e.* Kameda and Ishizaka, 2005).

4.5 Spatial Distribution

Spatial and temporal distributions of phytoplankton are mainly controlled by nutrient availability. Sverdrup (1955) showed expected high primary production areas from distribution of upwelling and vertical mixing area. The expected distribution is now verified by ocean color satellite data and the prediction was extremely accurate (Fig. 4.1). Nutrient concentration in the surface water of large area of ocean is low, and phytoplankton growth is nutrient limited. Nutrient is available in the surface water of the upwelling and vertically mixed area because high nutrient water is imported from deeper layer. Upwelling is often observed in coastal area, specifically west of east coast of continents, because wind blowing along the coast (following the wind left and right hand side is coast for northern and southern hemisphere, respectively) and rotation of earth (known as Coriolis force) moves surface water away from the shore and the surface water is replaced with high nutrient deep water (Fig. 4.2). Similar upwelling can be seen in the open ocean equatorial area where the westward trade wind and Coriolis force nearly symmetric along the equator moves surface water away from the equator.

Difference of the nutrient not only induces difference in biomass of phytoplankton but also difference in phytoplankton composition. Less nutrient open ocean environment are mostly dominated by small phytoplankton, such as cyanobacteria and small flagellates, whereas high nutrient upwelling region mostly dominated by large phytoplankton such as diatoms and dinoflagellates. The difference of the size structure also changes the food web structure and length of flood chain (Lalli and Parsons, 1995). Small and large primary producer expects to induce longer and shorter food chain and inefficient and efficient fish production, respectively. Ryther (1969) estimated world fish production is 100 times higher in the upwelling area than in the open ocean even the area of upwelling is only 1/1000 of open ocean area. Longhurst *et al.* (1995) suggested large number of biogeochemical provinces according to the difference of physical control of ecosystem structure.

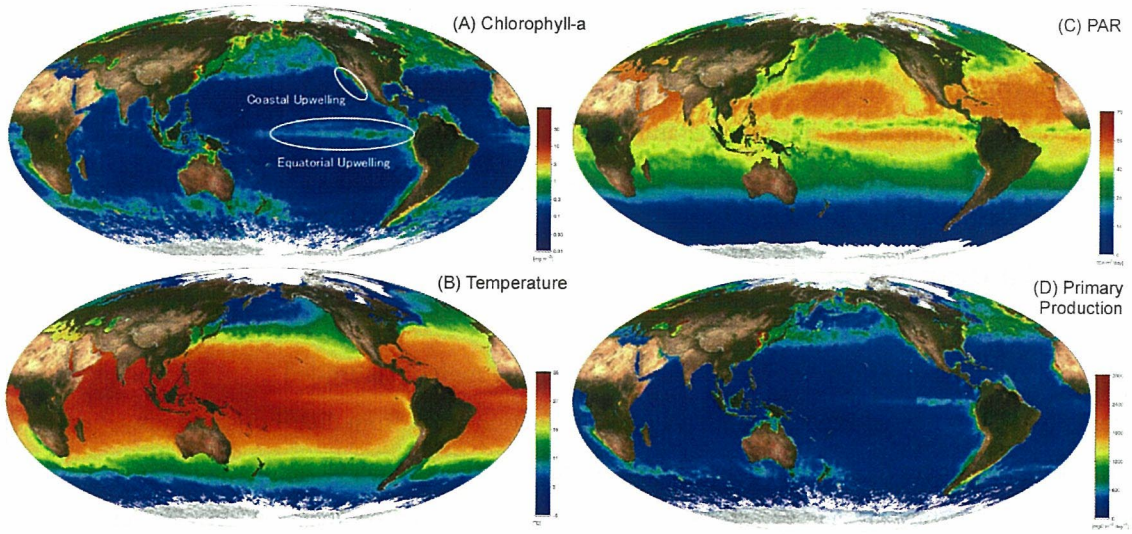

Figure 4.1 Global distribution of chlorophyll-a (A), sea surface temperature (B), photosynthetically active radiation (C) and primary production (D) derived from seasonal data (April-June 2003) of Global Imager (JAXA).

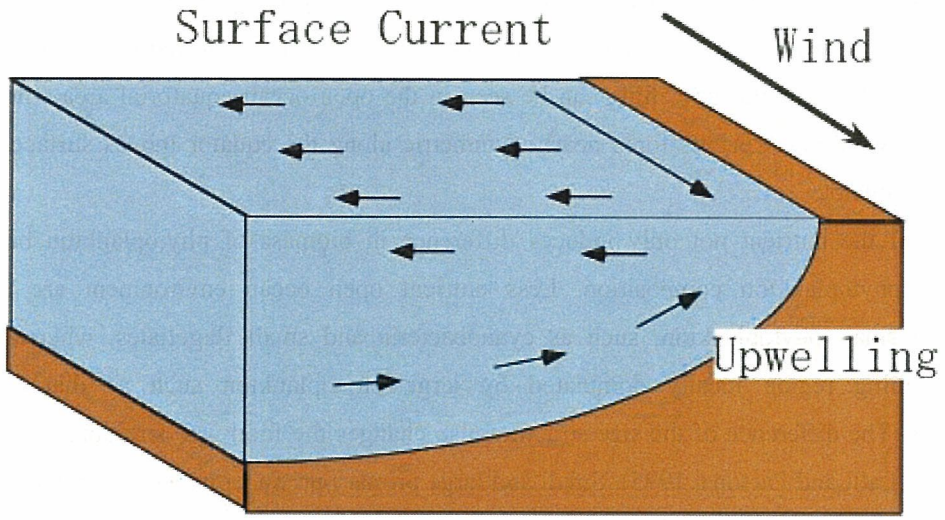

Figure 4.2 Wind driven coastal upwelling

4.6 Temporal Variability

There are variability of environment with various time scale and they influence the biomass of phytoplankton and primary production. In terms of shorter time scale than season, precipitation may be one of the important factors of the variability. In coastal area, precipitation induces increase of river discharge with nutrient inputs and stimulated short time scale phytoplankton blooms. Sometimes red tide, including harmful algal bloom (HAB), occurs after precipitation (cf. Ishizaka *et*

al., 2006). Storms, including typhoon, also induces short time scale increase of phytoplankton associated with nutrient increase through upwelling and strong wind mixing (cf. Siswanto *et al.*, 2007).

In temporal area, seasonal variation of phytoplankton is large (Fig. 4.4). During summer when water is stratified, nutrient in the surface water is depleted and phytoplankton biomass is less. Cooling and strong wind enhances mixing condition at fall, and nutrient is brought into the surface layer and phytoplankton biomass increases (known as fall bloom). During winter, deep water mixing carries phytoplankton to deep layer where light is less and light limitation is strong, and phytoplankton biomass becomes less even nutrient concentration is high in the surface water. Stratification starts during spring and phytoplankton enclosed in the high nutrient and high light surface water and increases the biomass (known as spring bloom). The depth where the amount of photosynthesis integrated from the surface is equivalent to the amount of integrated respiration is called critical depth (Fig. 4.4).

On the other hand, seasonal variation of phytoplankton in the tropical coastal water seems more to depend on monsoon. Change of direction and magnitude of monsoon often change the area of upwelling and mixing associated with the monsoon and causes the variation of phytoplankton biomass (*cf.* Tan *et al.*, 2006).

ENSO (El Nino Southern Oscillation) is known as large variability with frequency of several years. Temperature increases at the eastern equatorial area during El Nino caused by the reduction of upwelling, and phytoplankton biomass also decreases. It is well reported that the biological impacts including decrease of fishing yield during the El Nino. El Nino also influences to climate and oceanographic condition in remote area through teleconnection. For example, spring bloom in the Japan Sea was about one month earlier than La Nina year because of the weak spring wind (Yamada *et al*, 2006).

Global warming may have already started to influence phytoplankton biomass and primary production in a large area. Although there is still less information about the influence, El Nino may be one of the examples of temperature increase. Behrenfeld *et al.* (2006) recently showed phytoplankton abundance in large area of ocean may decrease with increase of temperature because the strengthening of stratification may be reducing the input of nutrients to the surface layer. The change of nutrient supply and other factors may influence not only biomass and primary production but also the species composition and whole ecosystem structure, fish yield and biological pump. Recent increase of HAB in various area may also related to global warming

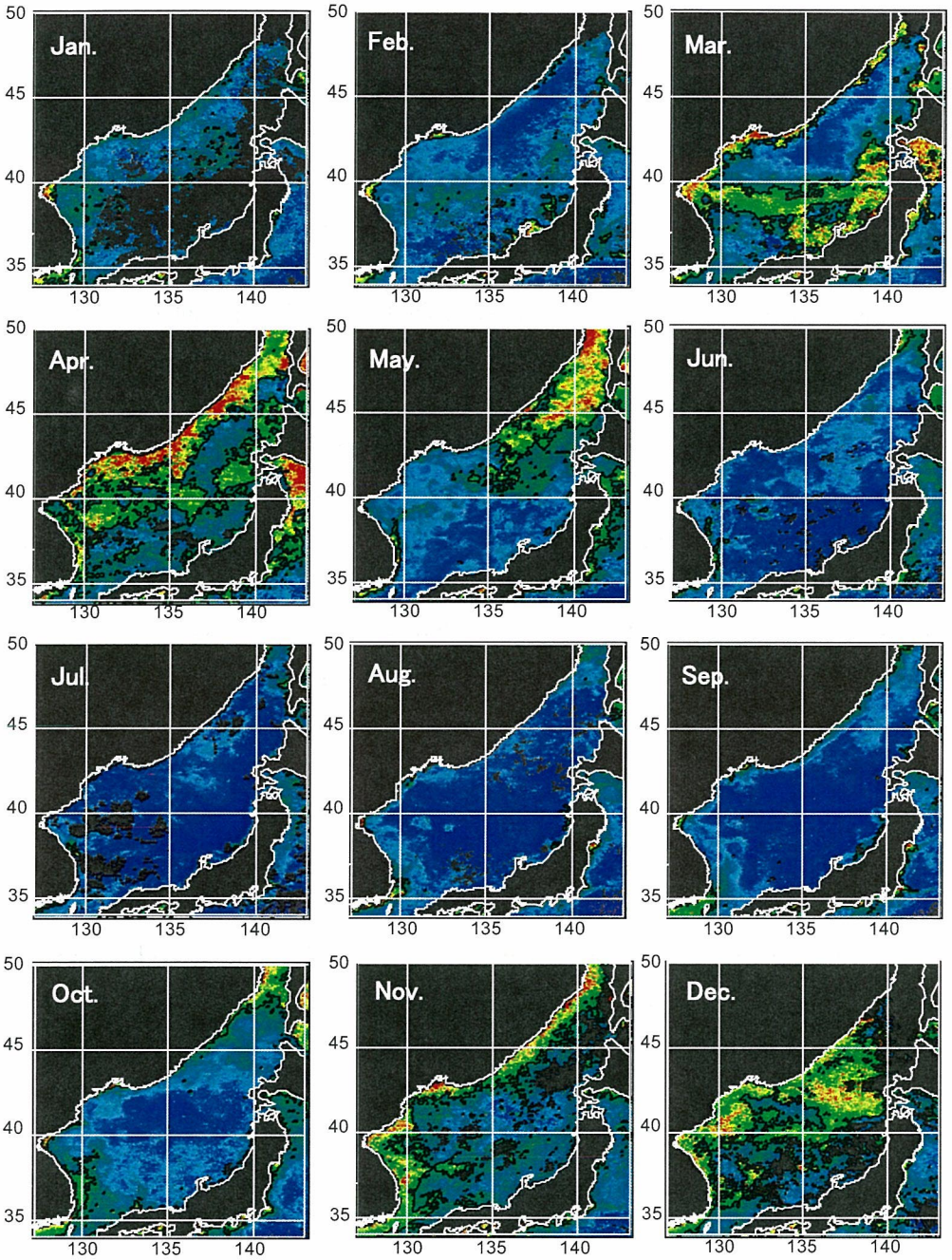

Figure 4.3 Monthly SeaWiFS chlorophyll images in the Japan Sea.

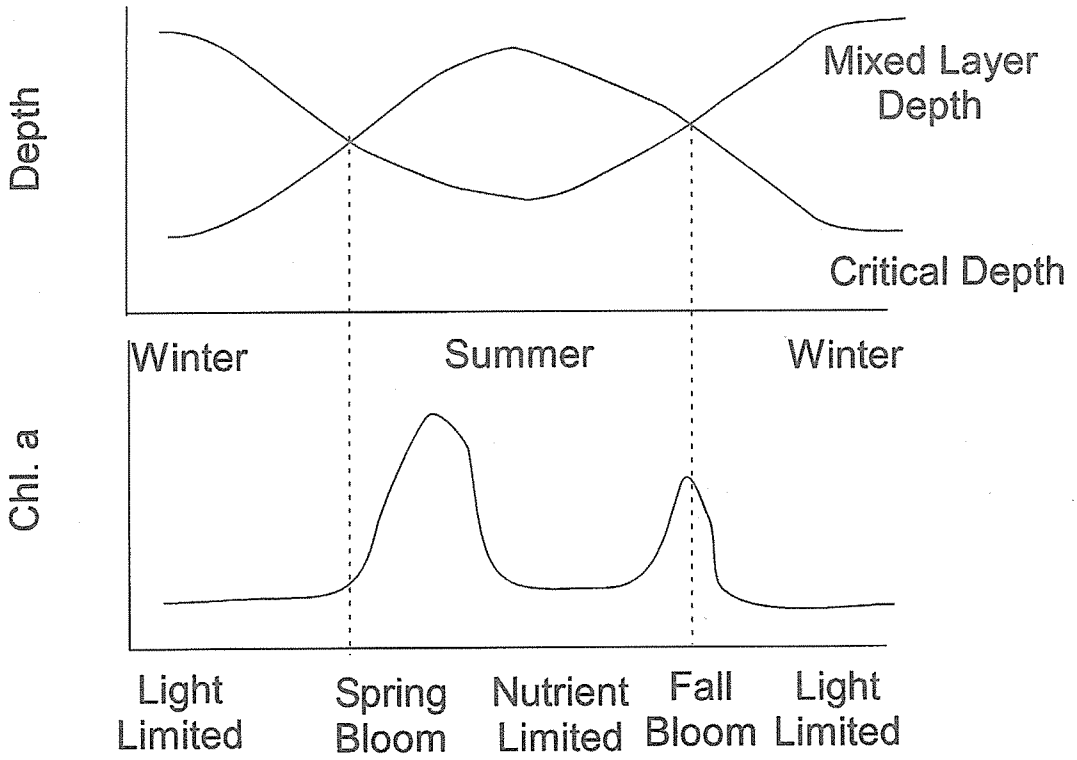

Fig.4.4 Seasonal changes of critical depth and mixed layer depth (upper panel), seasonal change of chlorophyll a concentration, and limiting factors between seasonal blooms in temporal region.

4.7 Concluding Remarks

Phytoplankton is an important organism conducting primary production in ocean. Spatial and temporal variability of biomass of phytoplankton and primary production can be detected by ocean color remote sensing. Ocean color remote sensing is a powerful tool to understand the influence of human activity to the ocean.

References

Behrenfeld, M. J., R. T. O'Malley, D. A. Siegel, C. R. McClain, J. L. Sarmiento, G. C. Feldman, A. J. Milligan, P. G. Falkowski, R. M. Letelier and E. S. Boss (2006) Climate-driven trends in contemporary ocean productivity. *Nature* **444**: 752-755.

Falkowski, P. G. and J. A. Raven (2007) *Aquatic Photosynthesis - 2nd Ed.*, Blackwell Science. pp. 500.

Ishizaka, J., Y. Kitaura, Y. Touke, H. Sasaki, A. Tanaka, H. Murakami, T. Suzuki, K. Matsuoka, H. Nakata (2006) Satellite Detection of Red Tide in Ariake Sound, 1998-2001. *J. Oceanogr.* 62:37-45.

Kameda, T. and J. Ishizaka (2005) Size-fractionated primary production estimated by a two-phytoplankton community model applicable to ocean color remote sensing. *J. Oceanogr.* 61, 663-672.

Lalli, C. M. and T. R. Parsons (1995): *Biological Oceanography: an Introduction - 2nd Ed.*, Elsevier Science. pp. 320.

Longhurst, A. (2006): *Ecological Geography of the Sea - 2nd Ed.*, Academic Press. pp. 560.

Mann, K. H. and J. R. N. Lazier (2006): *Dynamics of Marine Ecosystems - 3rd ed.*, Blackwell Pub. pp. 496.

Ryther, J. H. (1969): Photosynthesis and fish production in the sea. *Science* **166**: 72-76.

Siswanto, E., J. Ishizaka, K. Yokouchi, K. Tanaka, C.K. Tan (2007) Estimation of Interannual and Interdecadal Variations of Typhoon-Induced Primary Production: A Case Study for the Outer Shelf of the East China Sea, *Geophysic. Res. Let.*, 34, L03604, doi:10.1029/2006GL028368.

Sverdrup, H. U. (1955): The place of physical oceanography in oceanographic research. *J. Mar. Res.* 14: 287-294.

Tan, C. K., J. Ishizaka, S. Matsumura, F. M. Yusoff and M. I. H. Ibrahim (2006): Seasonal variability of SeaWiFS chlorophyll a in the Maraca Straits in relation to Asain monsoon. *Cont. Shelf Res.* **26**: 168-178.

Yamada, K. and J. Ishizaka (2006) Estimation of Interdecadal Change of Spring Bloom Timing; in the Case of the Japan Sea, *Geophysic. Res. Let.* 33, L02608, doi:10.1029/2005GL024792.

Chapter 5

Zooplankton in the Ocean

Shin-ichi Uye
Graduate School of Biosphere Sciences, Hiroshima University
4-4 Kagamiyama 1 Chome, Higashi-Hiroshima 739-8528, JAPAN
e-mail: suye@hiroshima-u.ac.jp

5.1 Plankton: major components in marine lower trophic levels

Plankton are those organisms that live in the water column and are too small to be able to swim counter to typical ocean currents.

Phytoplankton are photosynthetic protists and plants, and usually consist of single-celled organisms or of chains of cells. Although some may have locomotory organs such as flagella, their movements in the water column are nearly completely controlled by water turbulence and currents and by their own bulk density. Diatoms and dinoflagellates are the most common phytoplankton taxa.

Zooplankton comprise non-photosynthetic planktonic protists and animals, ranging from single-celled forms to small vertebrates, such as larval fishes. Although they may be able to swim, their movements are largely determined by major water currents, turbulence, and their own bulk density. Copepods are by far the largest group of crustaceans among zooplankton, followed by euphausiids. Gelatinous forms such as cnidarians, ctenophores, salps and larvaceans are also common.

Some plankton do not fit either the zooplankton or phytoplankton mold. Some protists, for example, may be photosynthetic, but also can ingest other plankton. Such plankton are said to be mixoplankton.

Meroplankton are zooplankton that spend only part of their lifetime as plankton, and are benthic or nektonic for the remainder. They include the planktonic larval stages of many benthic invertebrate groups and pelagic fishes.

Holozooplankton, by contrast, are those planktonic organisms that spend whole their life-time in the water column.

Neuston are plankton associated with the sea surface, such as bacterial films, and pleuston are plankton that live at the surface and also protrude into the air. The latter include animals that have floats, such as the Portuguese man-of-war.

Planktonic organisms are also classified by their size. The classes are picoplankton (0.2 to 2 μm), nanoplankton (2 to 20 μm, Fig. 5.1), microplankton (20 to 200 μm, Figs. 5.2 and 5.3), mesoplankton (200 to 2,000 μm, Fig. 5.4), macroplankton (2,000 to 20,000 μm, Fig. 5.4), megaplankton (>20,000 μm). Most plankton nets catch plankton of microplankton size and larger.

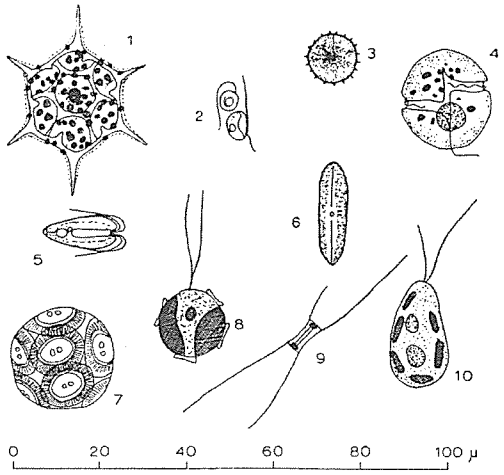

Figure 5.1 Examples of nanoplankton. Flagellates: *Distephanus* (1), *Thalassomonas* (2), *Gymnodinium* (4), *Tetraselmis*(5), *Coccolithus* (7), *Pontosphaera* (8), *Cryptochrysis* (10). Diatoms: centrate (3), pennate (6), *Chaetoceros* (9).

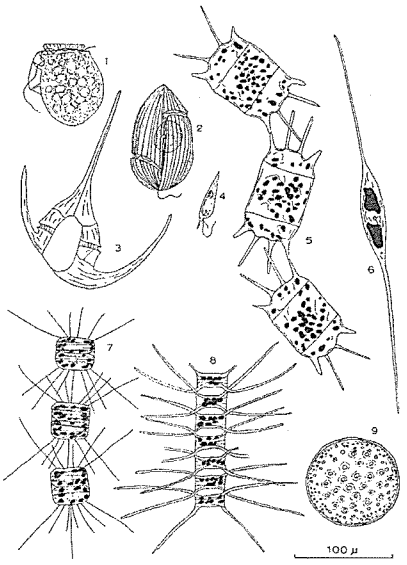

Figure 5.2 Examples of microphytoplankton. Dinoflagellates: *Dinophysis* (1), *Gyrodinium* (2), *Ceratium* (3), *Prorocentrum* (4). Diatoms: *Biddulphia* (5), *Nitzschia* (6), *Thalassiosira* (7),

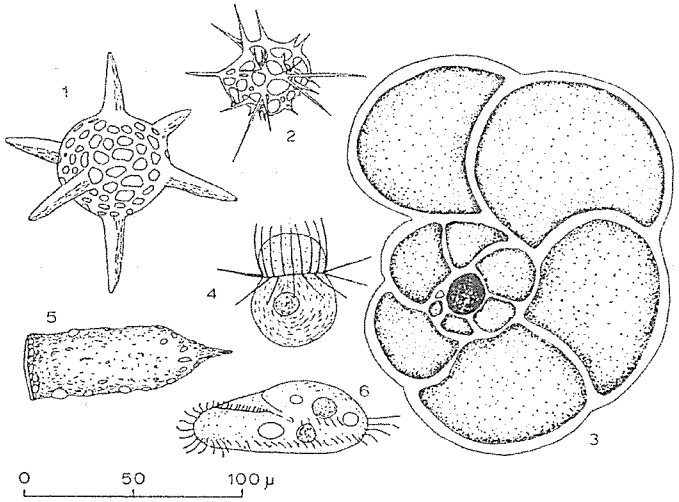

Figure 5.3 Examples of microzooplankton. Radiolarians: *Hexastylus* (1), *Plectacantha* (2).Foraminiferan: *Pulvinulina* (3). Ciliates: *Mesodinium* (4), *Tintinnopsis* (5), *Amphisia* (6).

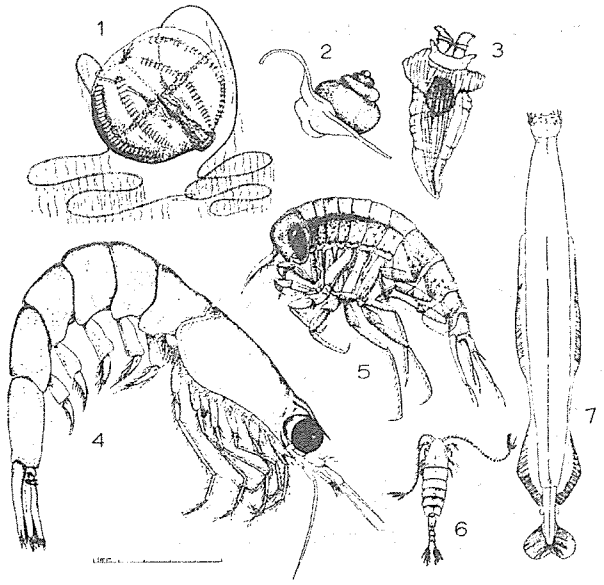

Figure 5.4 Examples of macro- and mega-zooplankton. Ctenophore: *Pleurobrachia* (1). Mollusc pteropods: *Limacia* (2), *Clione* (3). Euphausiid: *Thysanoessa* (4). Amphipod: *Parathemisto* (5). Copepod: *Calanus* (6). Chaetognath: *Sagitta* (7).

5.2 Primary production

Productivity is the amount of living tissue produced per unit time. It is often estimated in terms of carbon contained in living material and expressed, for example, as grams of carbon produced per day, in a one square meter column of water, extending from the sea surface to the sea bed (g C m^{-2}

day^{-1}). The amount of living material present in the water column at any one time is the biomass, expressed as g C m^{-2}.

Phytoplankton are the dominant primary producers in the pelagic realm, converting inorganic materials (e.g. nitrate, phosphate) into new organic compounds (e.g. carbohydrates, proteins) by the process of photosynthesis and thereby starting the marine food chain. The building up of plant tissue by photosynthesis over time is generally referred to as primary production.

Although a number of steps are involved in photosynthesis, the reactions for the synthesis of typical organic compounds can be summarized as:

$$106CO_2+16HNO_3+H_3PO_4+122H_2O \rightarrow (CH_2O)_{106}(NH_3)16H_3PO_4+138O_2.$$

The photosynthetic rate is usually determined by measuring either the carbon dioxide taken up, or the oxygen produced, per unit time. Measurement of ^{13}C- or ^{14}C-uptake is the most commonly employed method in oceans at present.

Primary productivity is strongly affected by light intensity and nutrient supply. As can be seen from Fig. 5.5, light intensity decreases exponentially with depth, while nutrients are scarce in the surface layer, due to uptake by phytoplankton, but highly concentrated in deep layers, due to decomposition of sedimented organic matter. Primary production is only possible at depths where both light and nutrients are adequate.

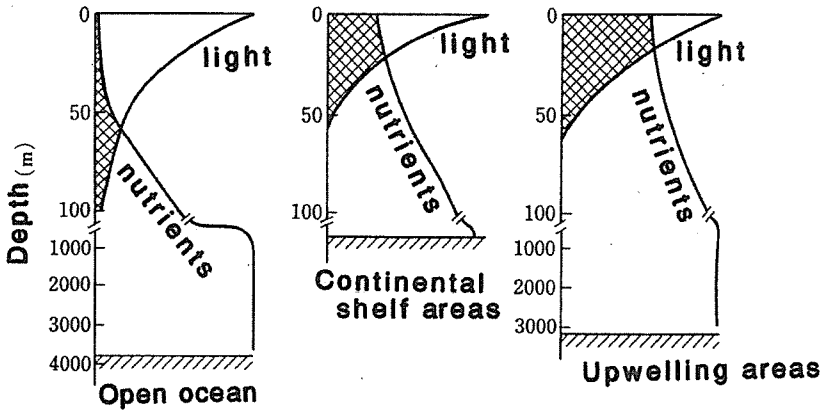

Figure 5.5 Schematic representation of primary productivity (hatched area) in relation to light intensity and nutrient supply in oceanic, continental shelf and upwelling regions.

5.3 Dissolved organic matter and its utilization by bacteria

Various forms of organic compounds (i.e. carbohydrates, amino acids, peptides) are dissolved in

seawater through extracellular exudation by phytoplankton, excretion by animals, and decomposition of detritus. These compounds, referred to as dissolved organic matter, are not utilized directly (e.g. by absorption) by zooplankton such as copepods. Heterotrophic bacteria are the principal consumers of dissolved organic matter in the water column and using it to multiply their populations. These bacteria, though very small (average cell diameter: 0.5 μm), convert the dissolved organic matter into a particulate form, making it available to small predators, such as protozoans. This part of the planktonic food web is known as the microbial loop (see below).

5.4 Zooplankton production

Zooplankton usually increase after the peak of the phytoplankton bloom has passed, owing to a time lag in zooplankton reproduction. Zooplankton such as copepods have a much longer generation time (weeks) than phytoplankton (hours to days), and a large population of zooplankton could graze a phytoplankton population to near-extinction, which would cause a collapse of the zooplankton until the phytoplankton recovered. Such overgrazing would result in marked oscillations in the zooplankton population.

Figure 5.6 shows the relation between the concentration of phytoplankton cells and their ingestion by the copepod *Calanus pacificus*. The ingestion rate increases linearly with cell concentration, but eventually reaches a maximum. Below the maximum, the feeding of the copepod is indicative of an animal that searches for, encounters, and feeds on particles in direct proportion to their concentration. But the maximum appears to be a saturation level, beyond which ingestion can increase no further. This may be because the feeding appendages are saturated with food, or because digestion efficiency would decrease if material were moved through the gut any faster. There is also some evidence for a minimum food level, below which the copepod does not expend energy to search for food and to feed.

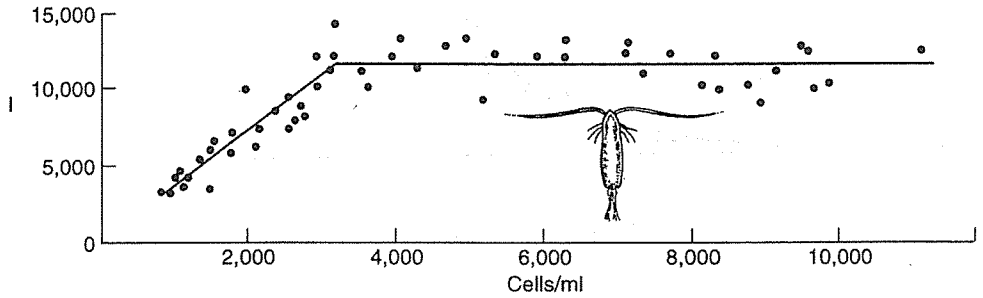

Figure 5.6 Ingestion rate (I) by the copepod *Calanus pacificus* as a function of diatom cell concentration.

Phytoplankton cell size and species also influence feeding in copepods and other zooplankton. Copepods feed at higher rates on diatom species with larger cell size, relative to smaller cells. Many zooplankton avoid toxic phytoplankton.

Ingested food is digested and assimilated through the wall of the digestive tract. Unassimilated food is egested in the form of a fecal pellet. Ingested energy is consumed primarily for metabolism (i.e. respiration) and then used for net growth only if there is a surplus (Fig. 5.7). Net growth takes the form of somatic growth during larval stages, and egg (or sperm) production in mature organisms.

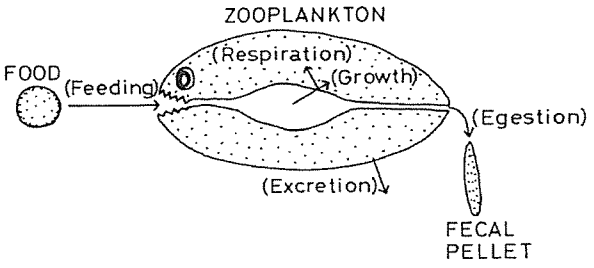

Figure 5.7 Schematic representation of energy flow in zooplankton

When food is not limited, the growth rate of copepods increases exponentially with temperature, as shown in Fig. 5.8.

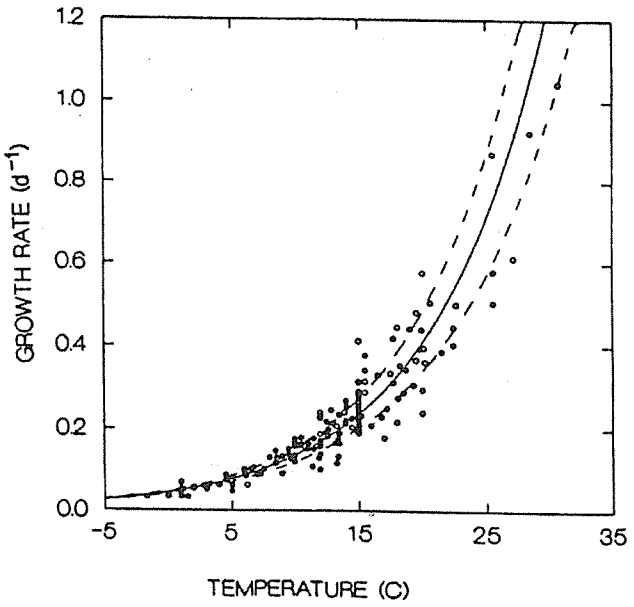

Figure 5.8 Specific growth rate of copepods as a function of temperature.

5.5 Pelagic food chains

A food web is a diagram that shows the overall pattern of feeding among organisms or which eats which. Figure 5.9 shows such a diagram for the North Sea, leading finally to feeding by the herring *Clupea harangus*. These feeding relationships are somewhat complex, but can be simplified into the linear food chain to the left of the figure, which presents the main species through which organic matter cycles. Each species represents a trophic level, which is defined as a species or group of species that feeds on one or more other species (which can be grouped into a lower trophic level).

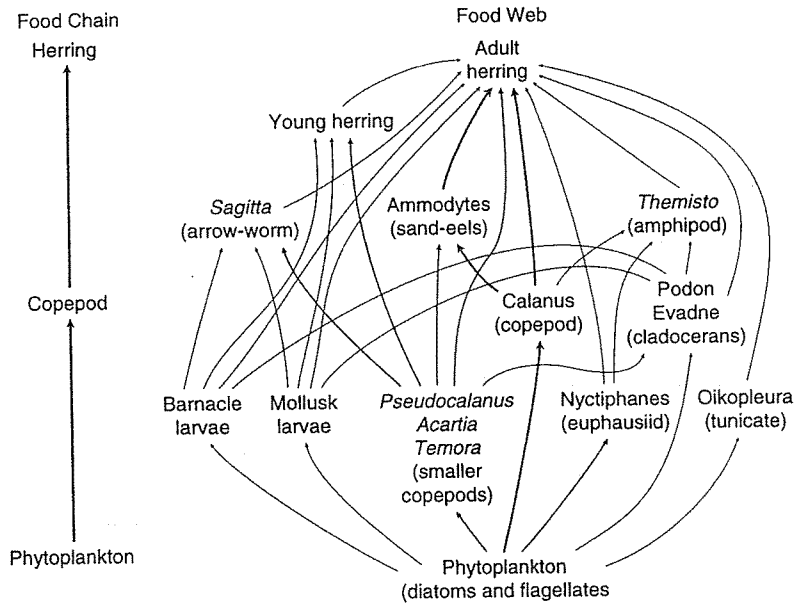

Figure 5.9 Food web constructed from the feeding relationships of the North Sea herring *Clupea harengus* during different life stages. A simplified food chain leading to the adult herring is provided at left.

Figure 5.10 depicts the two major food chains by which a top predator such as fish could meet its nutritional needs. The grazing food chain, in which phytoplankton are the immediate prey of herbivores, is a traditionally recognized chain. The other chain has merged in recent years from intensive study of the role in pelagic food webs of protozoans such as heterotrophic nanoflagellates and ciliates. In this chain, food material for fish production results from the utilization of dissolved organic matter by heterotrophic bacteria which, in turn, become the prey of various protozoans. This food chain stemming from bacteria is called the microbial food chain (or microbial loop). Some of the dissolved organic materials passing into bacteria and then through protozoans are made available again, via mineralization processes, for use by phytoplankton.

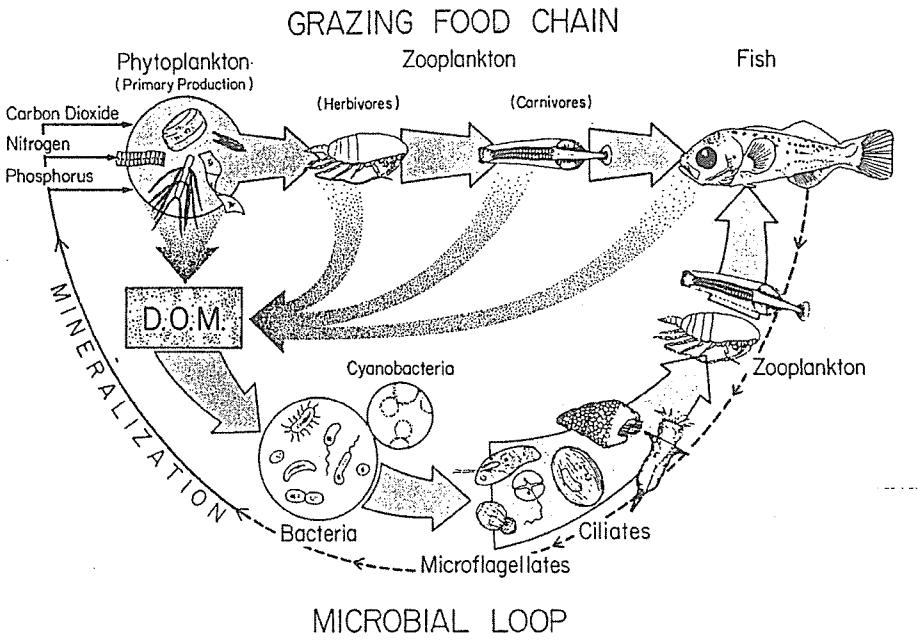

Figure 5.10 Schematic representation of the traditional grazing food chain and the currently emerging microbial loop.

5.6 Food chain in different marine habitats

The number of trophic levels from phytoplankton, the first trophic level, up to commercial fish species, varies depending on the marine habitat, i.e. open ocean, continental shelf or upwelling region (Fig. 5.11). In an oceanic habitat, where the average size of phytoplankton cells is the smallest and the primary productivity is the lowest owing to the lack of nutrients in the photic zone, there are typically 5 trophic levels below commercially-fished species, such as tuna and squid (which constitute the 6th trophic level). In a continental shelf habitat, where both phytoplankton cell size and primary productivity are in the intermediate range, the food chain can be represented by 4 trophic levels, whether it involves pelagic or benthic organisms. An upwelling habitat, such as off Oregon-California and Peru coasts or in Antarctic seas, has the fewest trophic levels in the food chain to the production of tuna or baleen whales. It is known that in this habitat certain fish, such as anchovy, may feed directly on large-celled phytoplankton such as chain-forming diatoms. Primary productivity in this habitat is the highest.

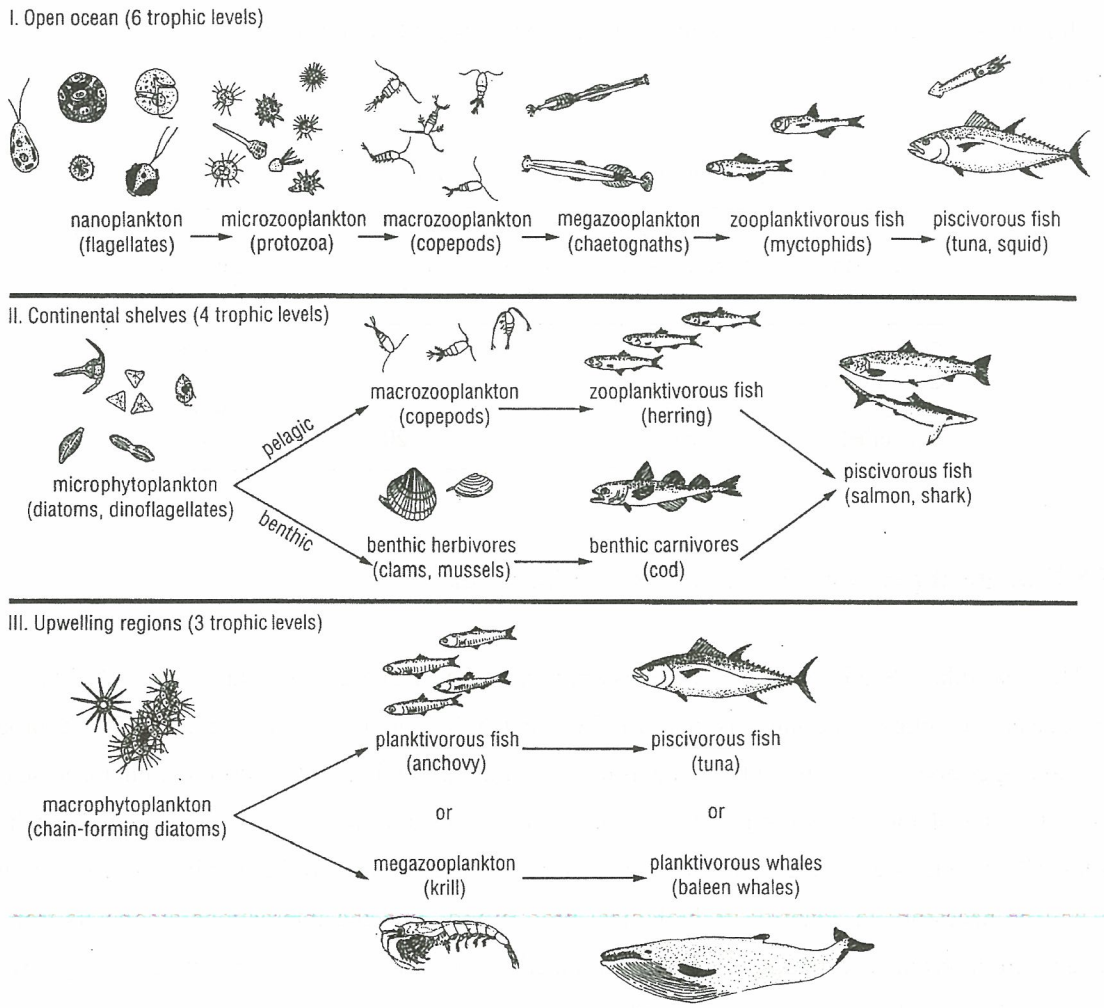

Figure 5.11 A comparison of food chains in three different marine habitats. The organisms representing each trophic level are only selected examples of the many marine species that could be present in that level.

5.7 World fish production

In order to estimate fish production, it is important to know how much energy is produced by the primary producers, the number of trophic levels, and the transfer efficiency between the adjoining trophic levels. Ryther (1969) assigned a 10% overall transfer efficiency to the oceanic food chain, a 15% efficiency to the continental shelf food chain, and a 20% efficiency to the food chain in upwelling areas. The resultant potential fish production is shown in Table 5.1. From these figures, it may be readily concluded that the upwelling regions should produce the largest fisheries, with the continental shelf areas and oceanic regions being of lesser importance. Total annual fish production by the world's oceans is estimated to be 240 million tons. The amount available for sustained harvesting may be assumed to be 100 million tons per year. The world fish catch in 1993 was 84

million tons, which means we are approaching maximum exploitation of the world's ocean fishery resources.

Table 5.1 Estimated fish production in three marine habitats

Marine environment	Mean primary productivity (g C/m^2/yr)	Trophic levels	Efficiency (%)	Fish production mg C/m^2/yr
Oceanic	50	5	10	0·5
Continental shelf	100	3	15	340
Upwelled	300	1·5	20	36 000

5.8 Biological productivity in the Seto Inland Sea

The Seto Inland Sea is situated in the western part of the Japanese archipelago. At 17,107 km^2, its surface area is roughly the same as that of Lake Ontario. It is about 500 km long, 5 to 50 km broad, and averages about 30 m in depth. Though the Seto Inland Sea is highly eutrophic, enclosed sea, it provides one of the world's highest fish catches on a per-unit-area basis (mean annual catch in 1989-1993: 16 tons wet weight km^{-2} yr^{-1}). In order to sustain fishery production in this sea in future, it will be necessary to quantify its biological productivity, and the interactions among its trophic levels, from primary production to fish production. To this end, collaborative surveys were conducted during 4 cruises (in October 1993, and January, April and June 1994) covering the entire Seto Inland Sea. Along with general oceanographic surveys, we measured the phytoplankton primary production rate using the ^{13}C technique, and zooplankton secondary and tertiary production rates using the cumulative growth method. The production rate of the major planktivorous fish, i.e. anchovies, sand eels and sardines, was also estimated based on their annual catch. In this section, I give a brief description of the survey results.

Phytoplankton primary production rate The average primary production over the entire Seto Inland Sea was highest in October (1,300 mg C m^{-2} d^{-1}), followed in descending order by April, June and January (779, 566 and 394 mg C m^{-2} d^{-1}, respectively). The average annual primary production was 781 mg C m^{-2} d^{-1} (*i.e.* 285 g C m^{-2} yr^{-1}). The extremely high rate in October was probably due to large nutrient load associated with high precipitation over the preceding months.

Zooplankton secondary and tertiary production rates Secondary production, which is attributed to the production by microzooplankton and herbivorous or suspension-feeding net-zooplankton, was much higher in October (637 mg C m^{-2} d^{-1}) than in the other months (89, 146 and 94 mg C m^{-2} d^{-1} in January, April and June, respectively). The average annual secondary production was 221 mg C m^{-2} d^{-1} (*i.e.* 81.0 g C m^{-2} yr^{-1}), 64% of which consisted of net-zooplankton.

Tertiary production, which is assigned to the production by carnivorous net-zooplankton, was also much higher in October (120 mg C m^{-2} d^{-1}) than in the other months (22.5, 44.0 and 18.3 mg C m^{-2} d^{-1} in January, April and June, respectively), with a average annual rate of 54.5 mg C m^{-2} d^{-1} (*i.e.* 19.9 g C m^{-2} yr^{-1}).

Planktivorous fish production rate Annual planktivorous fish production rate was estimated as 4.77 mg C m^{-2} d^{-1} (*i.e.* 1.74 g C m^{-2} yr^{-1}), 26% of which was attributed to secondary production, due to herbivory of sardines and anchovies. Fish tertiary production was 3.53 mg C m^{-2} d^{-1} (*i.e.* 1.29 g C m^{-2} yr^{-1}).

Trophic dynamics Figure 5.12 depicts a simplified food chain in the pelagic ecosystem of the Seto Inland Sea. The transfer efficiencies from primary to secondary production and secondary to tertiary production were 28 and 26%, respectively, both higher than the efficiency of less than 20%, commonly recognized by researchers for marine food chains. Production of planktivorous fish accounted for only a small portion (6%) of total tertiary production. The transfer efficiency from primary through secondary to the fish tertiary production was 0.45%.

Conclusion At present, the Seto Inland Sea has high primary production and high transfer efficiency between its lower trophic levels, and no deleterious effects of excessive eutrophication on its pelagic food chains can be detected. However, in stagnant areas such as Osaka Bay, Harima-Nada and Hiroshima Bay, benthic hypoxia or anoxia is prevalent in the summer, and the production of benthos may be significantly affected. Proper environmental measures should be taken in these areas to foster the recovery of their demersal fish populations.

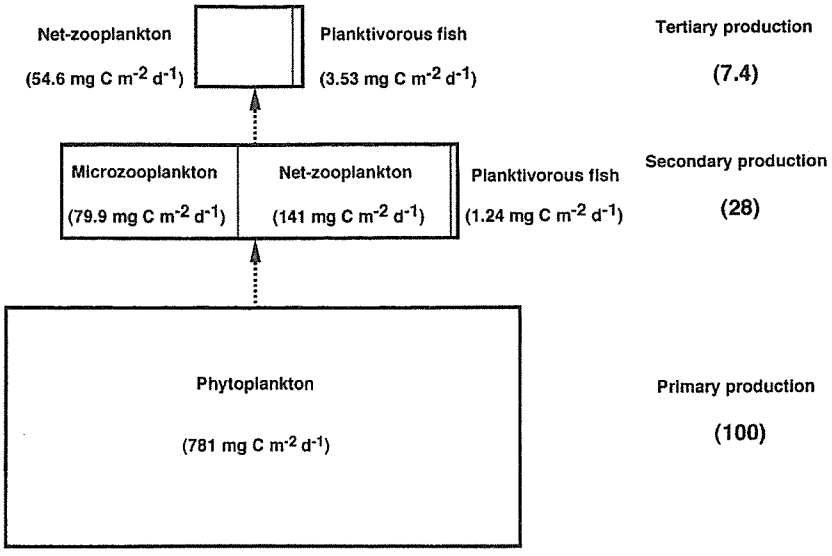

Figure 5.12 Simplified trophic structure of the pelagic ecosystem of the Seto Inland Sea. The compartment area of each trophic level represents roughly the relative magnitude of production rate. The transfer efficiencies from primary producers to secondary and tertiary producers are shown on the right.

References

Azam, F., T. Fenchel, J. G. Gray, L. A. Meyer-Reil and T. Thingstad (1983). The ecological role of water column microbes in the sea. *Mar. Ecol. Prog. Ser.*, 10: 257-265.

Beers, J. R. (1986). Organisms and the food web. In *Plankton Dynamics of the Southern California Bight,* Berlin: Springer-Verlag. (ed. Eppley, R. W.), pp. 84-175.

Frost, B. W. (1972). Effects of size and concentration of food particles of the feeding behavior of the marine planktonic copepod Calanus pacificus. *Limnol. Oceanogr.*, 17: 805-815.

Hashimoto, H., T. Hashimoto, O. Matsuda, K. Tada, K. Tamai, S. Uye and T. Yamamoto (1997). Biological productivity of lower trophic levels of the Seto Inland Sea. In *Sustainable Development in the Seto Inland Sea, Japan-From the Viewpoint of Fisheries,* Tokyo: TERRAPUB. (eds. Okaichi, T. and T. Yanagi), pp. 17-58.

Huntley, M. E. and M. D. G. Lopez (1992). Temperature-dependent production of marine copepods: a global synthesis. *Am. Tat.*, 140: 201-242.

Lalli, C. M. and T. R. Parsons (1993). *Biological Oceanography: An Introduction.* Oxford: Pergamon Press.

Parsons, T. R., M. Takahashi and B. Hargrave (1984): *Biological Oceanographic Processes*, 3rd Edition. Oxford: Pergamon Press.

Raymont, J. E. G. (1980). *Plankton and Productivity in the Oceans. Vol. 1: Phytoplankton.* 2nd Edition. Oxford: Pergamon Press.

Raymont, J. E. G. (1983). *Plankton and Productivity in the Oceans. Vol. 2: Zooplankton.* 2nd Edition. Oxford: Pergamon Press.

Russell-Hunter, W. D. (1970). *Aquatic Productivity.* London: Macmillan.

Ryther, J. H. (1969). Photosynthesis and fish production in the sea. *Science*, 166: 72-76.

Chapter 6

Material Dynamics in the Coastal Seas

Akihiko Morimoto
Hydrospheric Atmospheric Research Center (HyARC),Nagoya University
Furo-Cho, Chikusa-Ku, Nagoya 464-8601, JAPAN
e-mail: amorimoto@hyarc.nagoya-u.ac.jp

6.1 Introduction

Enormous materials such as fresh water, nutrients and harmful material are supplied from land to coastal sea, and a part of materials sink to bottom in the coastal sea or transport to the open ocean. In order to understand and predict environment in the coastal sea, we have to understand material dynamics there. Materials in the ocean are roughly divided 2 materials, one is conservative material such as salinity and the other is non-conservative material such as nutrients and plankton. The conservative material is transported and spread by advection and diffusion. On the other hand, dynamics of the non-conservative material is more complex than that of conservative one because the biochemical processes take place during material transport process. For example, dissolved inorganic nitrogen (DIN) is consumed by phytoplankton. As a result DIN becomes particulate organic nitrogen (PON). Then PON is converted to DIN because of decomposition. Since DIN moves with the water motion but PON moves independently to the water motion owing to sinking process, it is more difficult to understand non-conservative materials dynamics. In this chapter, we will force on only conservative material dynamics in the coastal sea.

The conservative material is transported by advection and diffusion. What is advection and diffusion? The answer to the question is not so easy. Figure 6.1 shows schematically view of spreading of conservative material injected instantaneously at a point I in the coastal sea (Yanagi, 1999) . For the time-scale of a few hours, material is advected by tidal current with diffusion due to turbulence from wind wave, since generally tidal current is dominant and has maximum energy in the coastal sea (Fig. 6.1 (a)). For the time-scale of a few days, material is advected by residual flow with diffusion by oscillation of tidal current although a current speed of residual flow is smaller than that of tidal current (Fig. 6.1 (b)). For the time-scale of several ten days, material returns to near the injected point I with low concentration by advection of residual flow (Fig. 6.1 (c)). For the

time-scale of several hundred days, material spreads to entire bay by diffusion due to residual flow (Fig. 6.1 (d)). As mentioned before, tidal current acts as advection for the time-scale of a few hours while that acts as diffusion for the time-scale of a few days. Namely, the content of advection and diffusion is changed by the temporal and spatial scale of the phenomenon. For example, although current speed of residual flow is much smaller than that of tidal current, for the time-scale of more than a few days material is advected by residual flow but tidal current. Therefore, in order to understand the material transport processes in the coastal seas, it is necessary that physical processes on a wide temporal and spatial scale are revealed.

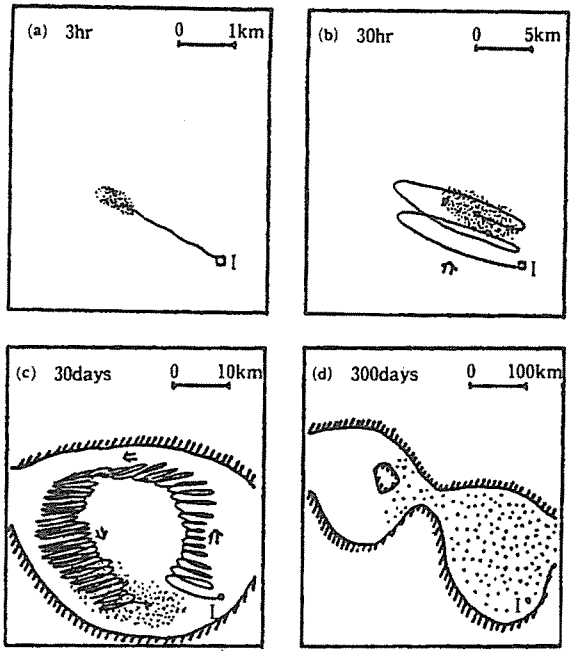

Figure 6.1 Schematic representation of material advection and dispersion injected at I in the coastal sea. The full line denotes the track of center of material and the arrow the residual flow (Yanagi, 1999).

6.2 Basic equation of material transport in the ocean

The temporal variation of conservative material concentration at a point in the ocean is expressed by the advection-diffusion equation. The advection-diffusion equation under the three dimensional Cartesian coordinate is shown as follows

$$\frac{\partial C}{\partial t}+u\frac{\partial C}{\partial x}+v\frac{\partial C}{\partial y}+w\frac{\partial C}{\partial z}=K_h\left(\frac{\partial^2 C}{\partial x^2}+\frac{\partial^2 C}{\partial y^2}\right)+K_z\frac{\partial^2 C}{\partial z^2} \quad . \tag{6.1}$$

Where C denotes the material concentration, t the time, x, y and z the horizontal and vertical axes, u, v and w the velocity components to the x, y and z axes, respectively and K_h and K_z the horizontal

and vertical diffusion coefficients.

The temporal variation of current velocity components u, v and w under the approximations of incompressive fluids, hydrostatic and Bousinesq approximation are expressed by following the momentum and continuity equations,

$$\frac{\partial u}{\partial t}+u\frac{\partial u}{\partial x}+v\frac{\partial u}{\partial y}+w\frac{\partial u}{\partial z}-fv=-\frac{1}{\rho_0}\frac{\partial P}{\partial x}+\frac{\partial}{\partial x}\left(A_h\frac{\partial u}{\partial x}\right)+\frac{\partial}{\partial y}\left(A_h\frac{\partial u}{\partial y}\right)+\frac{\partial}{\partial z}\left(A_z\frac{\partial u}{\partial z}\right) \quad , \quad (6.2)$$

$$\frac{\partial v}{\partial t}+u\frac{\partial v}{\partial x}+v\frac{\partial v}{\partial y}+w\frac{\partial v}{\partial z}+fu=-\frac{1}{\rho_0}\frac{\partial P}{\partial y}+\frac{\partial}{\partial x}\left(A_h\frac{\partial v}{\partial x}\right)+\frac{\partial}{\partial y}\left(A_h\frac{\partial v}{\partial y}\right)+\frac{\partial}{\partial z}\left(A_z\frac{\partial v}{\partial z}\right) \quad , \quad (6.3)$$

$$P=\rho_0 g\eta+\rho_0\int_z^0\frac{\rho-\rho_0}{\rho_0}gdz \quad , \quad (6.4)$$

$$\frac{\partial u}{\partial x}+\frac{\partial v}{\partial y}+\frac{\partial w}{\partial z}=0 \quad . \quad (6.5)$$

Where t denotes time, x and y are the horizontal axes, z directs upward from the mean sea surface, u, v and w the currents in the x, y and z directions, respectively, f is the Coriolis parameter, ρ water density, ρ_0 reference density, P pressure, g gravitational acceleration, η sea surface elevation, A_h and A_z horizontal and vertical eddy viscosity, respectively.

6.3 Tidal current

Tidal current is dominant in the coastal seas because of shallow water depth. Therefore, understanding of tide and tidal current phenomena is necessary to know the material dynamics in the coastal seas. Tide and tidal current is generated by the tide generating forces of moon and sun. The dominant constituents of tide and tidal current are semi-diurnal and diurnal components, that is, M_2, S_2, O_1 and K_1 constituents whose periods are 12.42 hours, 12.00 hours, 23.93 hours and 25.82 hours, respectively. Since horizontal gradient of the tide generating force is small in the coastal seas, there is little tide generated by direct effect of tide generating force. Therefore, tidal phenomenon in the coastal seas is governed by the tide that comes from the Open Ocean.

Let us consider a bay with a depth h and length l. Where tide with a period T enters into the bay from the Open Ocean. In this case, a standing wave is generated owing to combination of an incident wave with reflected wave. When horizontal scale of a wave is much greater than water depth, hydrostatic approximation would be assumed. The momentum and continuity equations under the assumption of linear motion and non-viscosity are follows

$$\frac{\partial u}{\partial t}=-\frac{1}{\rho_0}\frac{\partial P}{\partial x} \quad , \quad (6.6)$$

$$\frac{\partial u}{\partial x}+\frac{\partial w}{\partial z}=0 \quad . \quad (6.7)$$

From the hydrostatic approximation, Eq. (6.6) becomes

$$\frac{\partial u}{\partial t} = g\frac{\partial \eta}{\partial x} \quad . \tag{6.8}$$

Here η denotes a sea level from the mean sea surface. Since the horizontal gradient of sea level is independent with z, horizontal velocity becomes constant vertically as well. Therefore, Eq. (6.7) is integrated from sea bottom to sea surface. Eq. (6.7) becomes as follows

$$\frac{\partial \eta}{\partial t} = -h\frac{\partial u}{\partial x} \quad . \tag{6.9}$$

As a boundary condition, sea level, η, at the bay mouth ($x=l$) is $\eta = Am\cos\varpi t$, and horizontal velocity, u, at the bay head ($x=0$) is 0. Where Am is an amplitude of tide, $\omega=2\pi/T$ is angler frequency. The solutions of Eqs. (6.8) and (6.9) are

$$\eta = Am\frac{\cos kx}{\cos kl}\cos\varpi t \quad , \tag{6.10}$$

$$u = \frac{CAm}{h}\frac{\sin kx}{\cos kl}\sin\varpi t \quad . \tag{6.11}$$

Where $k = 2\pi / L$ denotes wave number, L wave length and $C = \sqrt{gh}$ phase speed of tide. From the above solutions, phase difference between tide and tidal current is 90 degree. Namely high and low water take place at slack tide, while mean sea level take place at food and ebb tide (Fig.6.2(b)). Looking at horizontal distribution of tide and tidal current in the bay, High and low water occur at the same time in the whole bay, and a node appears at the bay mouth. As for the tidal current, maximum velocity appears at the bay mouth while minimum velocity at the bay head and phase of tidal current is same in the bay (Fig.6.2(a)).

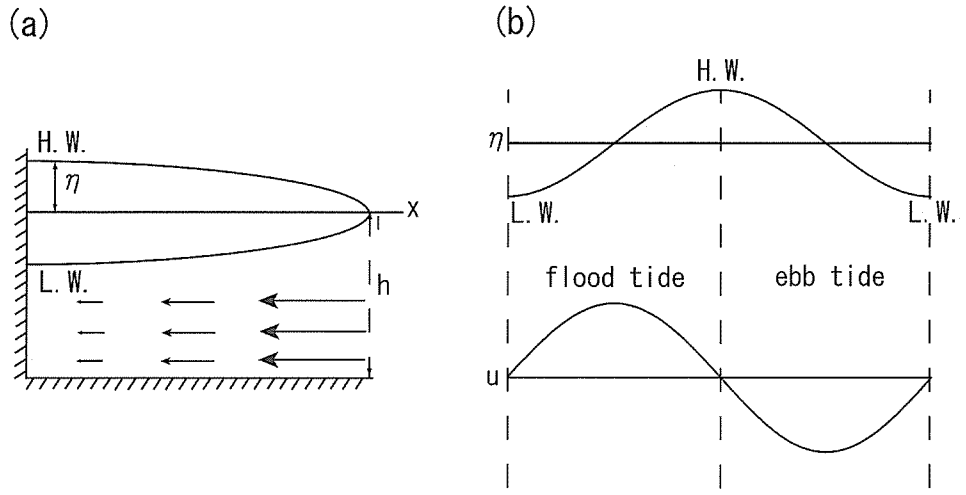

Figure 6.2 Tide and tidal current in the bay (a) and phase relation between sea level and tidal current.

Figure 6.3 shows tidal current amplitude of M_2 constituent in the Bungo Channel, which was calculated by a three dimensional numerical model (Morimoto and Yanag, 2000). At the entrance of Bungo Channel, tidal current is relatively small while in the Bungo Channel tidal current is strong with an amplitude more than 50cm/s.

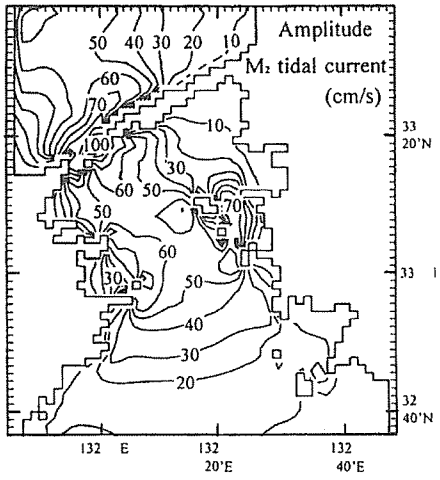

Figure 6.3 Co-range chart of M_2 tidal current amplitude at the sea surface calculated by a three dimensional numerical model (Morimoto and Yanagi, 2000)

6.4 Residual current

As mentioned in 6.3, tidal current is dominant in the coastal seas. In general, residual flow is weaker than tidal current in the coastal seas. However, when you consider relatively long-term material transport, residual flow becomes important. Since tidal current is oscillation flow, the position of material after one tidal cycle becomes almost same in original point if there is no horizontal distribution of tidal amplitude. Therefore, materials are transported by the residual flow. Main components of residual flow are tide-induced residual current, density-driven current and wind-driven current. In this section, I will explain each components of residual flow.

6.4.1 Tide-induced residual current

When you take average of current data over one tidal cycle, constant flow is derived. The constant flow generated by both non-linearity of tidal current and topographic effect is called the tide-induced residual current. It is assumed that the currents consist of linear combination of tidal current with tide-induced residual current. In this case, horizontal current velocities u and v and vertical vorticity are expressed as follows

$$u = u_T + u_R, \qquad v = v_T + v_R, \qquad \varsigma = \varsigma_T + \varsigma_R \ , \tag{6.12}$$

$$\varsigma = \frac{\partial v}{\partial x} - \frac{\partial u}{\partial y} \ . \tag{6.13}$$

Average over one tidal cycle of u_T, v_T and ζ_T are zero. As tide-induced residual current makes circulation, we focus on vorticity. Vorticity equation under the assumption of f=0 and non-viscosity is follows

$$\frac{\partial \varsigma}{\partial t}+u\frac{\partial \varsigma}{\partial x}+v\frac{\partial \varsigma}{\partial y}=-\frac{\beta}{h}\varsigma+K_h\nabla^2{}_H\varsigma \quad . \tag{6.14}$$

Eq. (6.12) puts into Eq. (6.14), then it takes average over one tidal cycle. Eq. (6.14) converted as follows

$$F_T+F_R-\frac{\beta}{h}\varsigma_R+K_h\nabla^2{}_H\varsigma_R=0 \quad , \tag{6.15}$$

$$F_T=\frac{\partial}{\partial x}(-\overline{u_T\varsigma_T})+\frac{\partial}{\partial y}(-\overline{v_T\varsigma_T}) \quad , \tag{6.16}$$

$$F_R=\frac{\partial}{\partial x}(-u_R\varsigma_R)+\frac{\partial}{\partial y}(-v_R\varsigma_R) \quad . \tag{6.17}$$

The first term indicates conversion of vorticity from tidal current to tide-induced residual flow due to non-linearity. In order to generate vorticity by the first term, divergence or convergence of vorticity transport is necessary. The second term indicates vorticity transport by tide-induced residual current. The third term indicates bottom friction and the last term shows damping due to horizontal viscosity. Namely, tide-induced residual current is generated by the balance among generating of vorticity by tidal current, vorticity transport by residual flow and dissipation of vorticity by friction.

Figure 6.4 shows tide-induced residual flow at 10m water depth in Bungo Channel. In the entrance of Bung Channel, the residual flow is week but strong near narrow strait because of strong non-linearity of tidal current near strait.

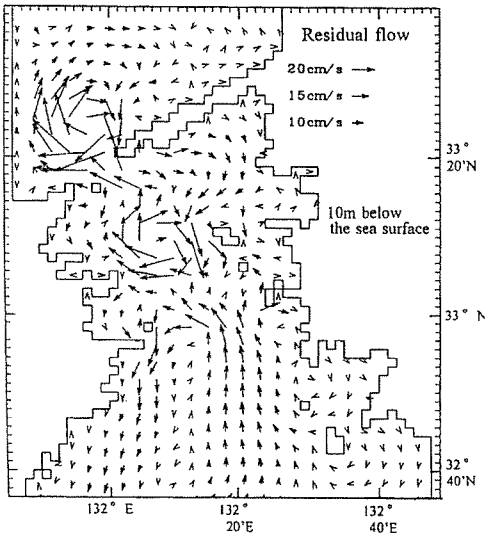

Figure 6.4 Tide-induced residual flow 10m below the sea surface in Bungo Channel calculated by a three dimensional numerical model (Morimoto and Yanagi, 2000).

6.4.2 Density-driven current

Density of sea water is function of water temperature, salinity and pressure. Since water temperature varies seasonal cycle in the mid latitude, density changes same as water temperature as well. Moreover, in the coastal seas salinity also changes due to river discharge. Therefore, density in the coastal seas is changed by both water temperature and salinity variations.

Spatial gradient of density generates flow that is called the density-driven current. In this section, I will explain estuarine circulation and the current due to the topographic effect as the example of density-driven currents.

6.4.2.1 Estuarine Circulation

In the estuarine, fresh water supplies from land while sea water enters from ocean side. As a result, since horizontal pressure gradient is generated due to input of buoyancy, currents occurs to adjust density field. Namely, low density water flows out from surface layer while high density water flows into from the bottom layer. Consequently, vertical circulation develops in the estuarine, which is called the Estuarine Circulation.

Let us consider rectangle area with water depth h, length l shown in Fig.6.5. Here density of left side is ρ_1 and that of right side ρ_2, and mean density is ρ. ρ_2 is less than ρ_1 and ρ_2-ρ_1=$\Delta\rho$. Total pressure P_1 acts from left side and P_2 from right side. Here as we do not consider wind stress, only bottom friction F_b acts at the sea bottom. Under the steady state, balance of forces is as follows

$$P_2 - P_1 = F_b \quad . \tag{6.18}$$

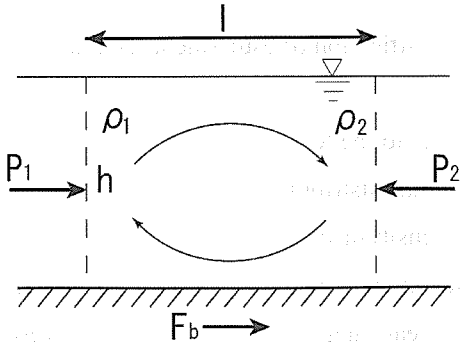

Figure 6.5 Schematic representation of estuarine circulation

Considering unit length, it is assumed that representative velocity is U and vertical eddy viscosity is K_z. In this case, magnitude of each term becomes

$$P_1 \approx \rho_1 g h^2, \quad P_2 \approx \rho_2 g h^2, \quad F_b \approx \rho K_z U l / h \quad . \tag{6.19}$$

Substitution above equations to Eq. (6.18), the following relation is derived

$$U \approx \frac{\Delta\rho g h^3}{\rho K_z l} \quad . \tag{6.20}$$

From the above relation, when density difference is large estuarine circulation develops. On the other hand, when the vertical mixing and the length of area are large, the circulation does not develop. If topographic feature is same, strength of the circulation would depend on $\Delta\rho/K_z$. $\Delta\rho$ and K_z is relation with river discharge and amplitude of tidal current, respectively. Therefore, the estuarine circulation is able to classify a few type based on both river discharge and strength of tidal current. The classification is shown in Fig. 6.6.

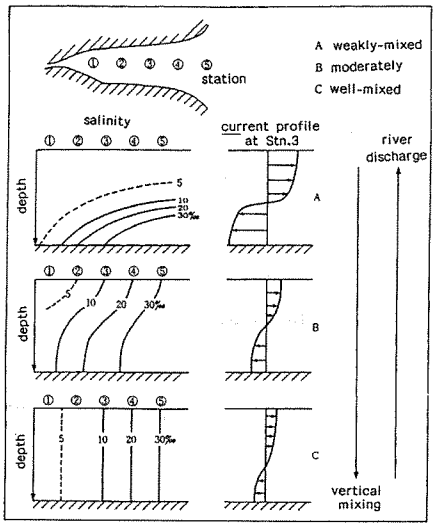

Figure 6.6 Classification of estuarine circulation (Yanagi, 1999)

6.4.2.2 Density-driven current due to the topographic heat accumulation

In the coastal seas, horizontal distribution of heat flux, evaporation and precipitation are homogenous generally. Hence density-driven current accompanied with inhomogenous distributions of those does not develop. However, if there is water depth variation, vertical circulation would develop due to the difference of heat capacity although the area receives constant cooling or heating. Let us consider that sea surface is heated uniformly. In this case, since the sea water in the shallow area becomes light, vertical circulation, off shoreward in the surface layer and shoreward in the lower layer, is generated as shown in Fig. 6.7 (a). Then let us consider that sea surface is cooled uniformly. In this case opposite circulation develops, that is, shoreward in the surface layer and off shoreward in the lower layer as shown in Fig. 6.7 (b).

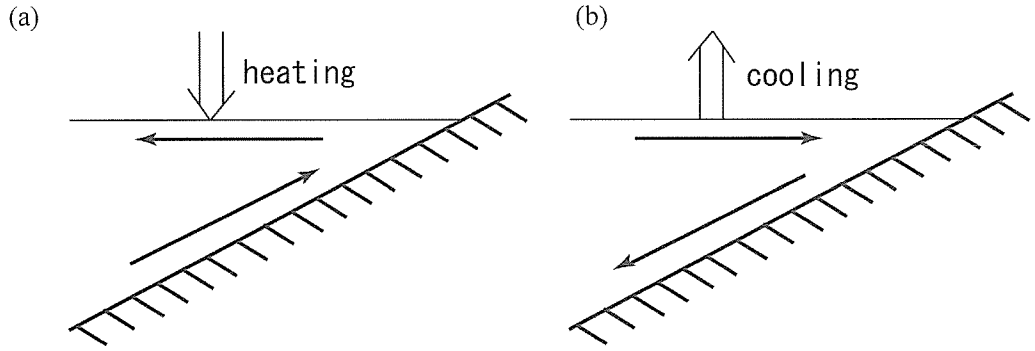

Figure 6.7 Density-driven current due to the topographic heat accumulation.

6.4.3 Wind-driven current

When wind blows over the sea, current is generated in the surface layer, which is called the wind-driven current. In this section, I will explain wind stress on the sea, the Ekman spiral and the Ekman transport.

Wind stress on the sea surface τ is given by

$$\tau = \rho_a C_d W^2 \quad . \tag{6.21}$$

Where ρ_a denotes the air density, C_d the drag coefficient and W the wind speed 10m above the sea surface. How much wind-driven current is generated by the wind stress? When wave develop fully by long-term wind blowing, it is able to assume that drag force from the air to sea surface and that from the sea to the air bottom are equal. Therefore, the following relation is derived

$$\tau = \rho_a C_d W^2 = \rho C'_d U^2 \quad . \tag{6.22}$$

Where ρ indicates density of sea water, C'_d the drag coefficient at the boundary between air and sea, U velocity of wind-driven current. Here we assume that C_d is equal to C'_d, the following equation is derived

$$U = \sqrt{\frac{\rho_a}{\rho} W} \approx 0.035W \quad . \tag{6.23}$$

Eq. (6.23) indicates that current of 3.5 % of wind speed is generated.

In order to understand effect of Coriolis force to the wind-driven current, let us consider sea with infinity area and constant water depth, and uniform wind is blowing. Since there is no horizontal boundary like land, pressure gradient force does not appear in the momentum equation. Basic equation for wind-driven current is follows

$$\frac{\partial u}{\partial t} - fv = \frac{\partial}{\partial z}\left(K_z \frac{\partial u}{\partial z} \right), \quad \frac{\partial v}{\partial t} + fu = \frac{\partial}{\partial z}\left(K_z \frac{\partial v}{\partial z} \right) \quad . \tag{6.24}$$

Here wind blows y direction.

Under the steady state and followings boundary condition,

$$z=0:\ \rho K_z\frac{\partial u}{\partial z}=0,\ \ \rho K_z\frac{\partial v}{\partial z}=\tau$$

$$z=\infty:\ u=v=0$$

we obtain the following solutions of Eq. (6.24)

$$u=\frac{\tau}{\rho\sqrt{K_z f}}\exp\left(-\frac{\tau}{D}z\right)\cos\left(\frac{\tau}{D}z+\frac{\pi}{4}\right)$$

$$v=\frac{\tau}{\rho\sqrt{K_z f}}\exp\left(-\frac{\tau}{D}z\right)\sin\left(\frac{\tau}{D}z+\frac{\pi}{4}\right)$$

$$D=\frac{1}{\tau}\sqrt{\frac{2K_z}{f}}$$

Wind-driven current at the sea surface is $\tau/(\rho\sqrt{K_z f})$. Therefore, sea surface current is proportion to wind stress and current direction deflects by 45 degree to the wind direction. Current speed exponentially decreases in vertical like a spiral and current speed at $z=D$ becomes 1/e of surface current speed. Here D is called the Ekman layer and Fig.6.8 shows the Ekman spiral.

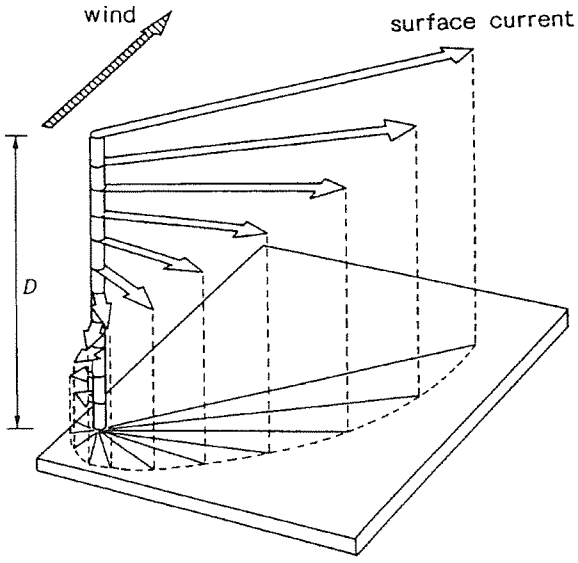

Figure 6.8 Ekman spiral (Yanagi, 1999)

Integration of u and v from sea surface to the sea bottom, volume transport in unit becomes as follows

$$Q_x=\int_{-\infty}^{0}u\,dz=\frac{\tau}{f\rho},\quad Q_y=\int_{-\infty}^{0}v\,dz=0\quad . \tag{6.25}$$

There is no volume transport in the direction of wind while total volume transport is normal to wind direction. This volume transport is called the Ekman transport.

6.5 Diffusion and Dispersion

Once materials are injected in a beaker, the materials spread over a long period of time. This is due to the Brownian motion of the water particles. This material spreading is called the molecular diffusion. In the ocean, we can see the almost same phenomenon but there is a discrepancy. Since there are a lot of eddies and turbulence in the ocean, materials injected into the ocean spread faster than molecular diffusion. The spreading of materials by eddies and turbulence is called the eddy diffusion. In the real ocean with eddies of many sizes, diffusion of materials are contributed by eddies which have same scale of spreading of materials. Eddies with larger scale make transport materials. Therefore, spreading of materials depend on a spectrum of turbulence. Horizontal eddy viscosity or diffusivity changes within 10-10^8 cm^2/s and becomes large in proportion to the 4/3 powers of the horizontal scale (Fig.6.9). Vertical eddy viscosity and diffusivity depend on the stability of water column and current shear. The value of vertical eddy viscosity and diffusivity changes within 0.1-100 cm^2/s.

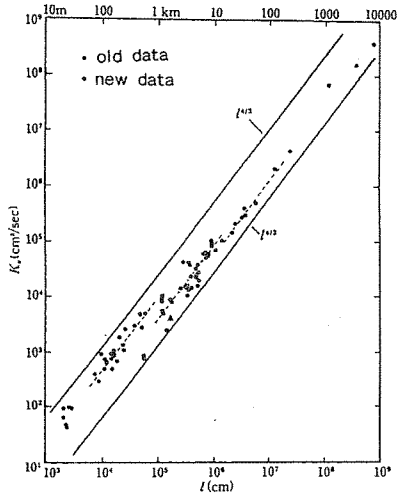

Figure 6.9 Relation between the apparent horizontal eddy diffusivity and the horizontal scale (Okubo, 1974).

If current has a shear, other type of diffusion would take place combination of current shear with eddy diffusion in the direction normal to the current shear. This diffusion is called the dispersion. Schematic figures of the eddy diffusion and the dispersion are shown in Fig.6.10. Both of vertical mean of current velocities are same U but constant flow in Fig6.10 (a) and shear flow in Fig.6.10 (b). In the case of Fig.6.10 (a), materials are advected by U and spread by horizontal eddy diffusivity. On the other hand, in the case of Fig.6.10 (b), we consider only vertical eddy diffusivity for simplification. Therefore, vertical mixing is done during time step τ which is longer than vertical diffusive time. At the time τ, materials spread over $2U\tau$. Since τ is longer than vertical diffusive time,

materials are well mixed vertically during period τ. As a result, materials spread wider area compare to Fig. 6.10 (a) although horizontal eddy diffusion is not considered. Namely, spreading of materials by the dispersion is 1 or 2 order larger than the eddy diffusion.

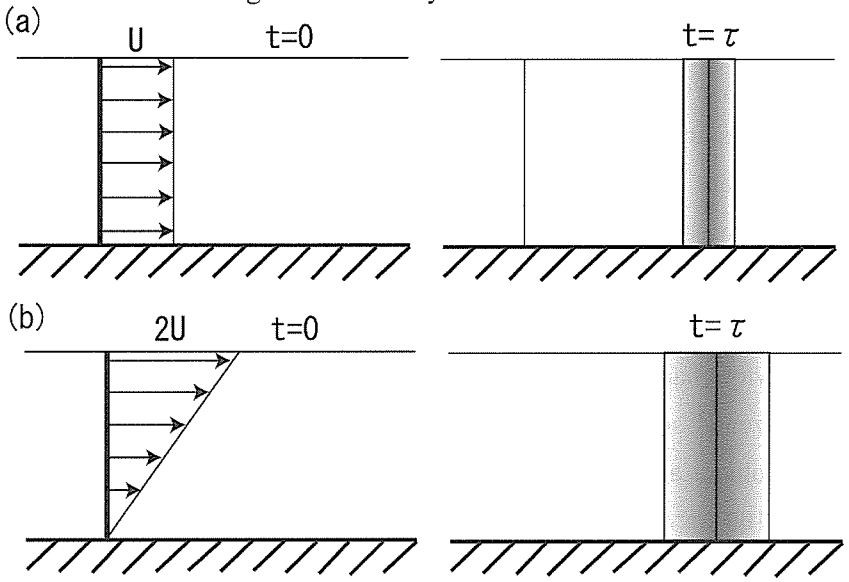

Figure 6.10 Eddy diffusion (a) and dispersion (b).

References

Okubo, A. (1974): Oceanic diffusion diagrams. Deep-Sea Research, 18, 789-802.

Morimoto, A. and T. Yanagi (2000): Relationship between the sand waves and the current field in the Bungo Channel, Japan. Interactions between Estuaries, Coastal Seas and Shelf Seas. Ed. by T. Yanagi, 217-232.

Yanagi, T. (1999): Coastal Oceanography. Terra Scientific Publishing Co., Tokyo.

Chapter 7

Biogeochemical Cycles in the Ocean

Toshiro Saino
Hydrospheric Atmospheric Research Center (HyARC), Nagoya University
Furo-Cho, Chikusa-Ku, Nagoya 464-8601, JAPAN
e-mail: tsaino@hyarc.nagoya-u.ac.jp

7.1 Why study ocean biogeochemical cycle

7.1.1 Biogeochemical cycles may be changing

The first slide is taken from the presentation of Dick Feely which was given here in Nagoya 3 years ago at the time of the final JGOFS North Pacific Synthesis meeting. You can see that temperature is increasing in accordance with increasing greenhouse gasses.

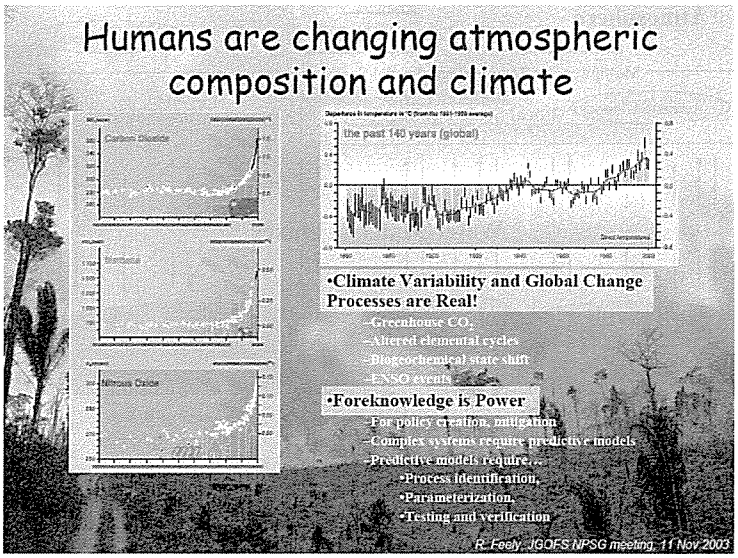

Slide 1 Human's impact on atmosphere and climate

These changes are real, and we already see some adverse effect on our daily life. To cope with these changes and to keep stay living on this planet, we need to have capability to predict the future climate in order to take right action. For that purpose we need to have mechanistic understanding to improve model to predict climate change.

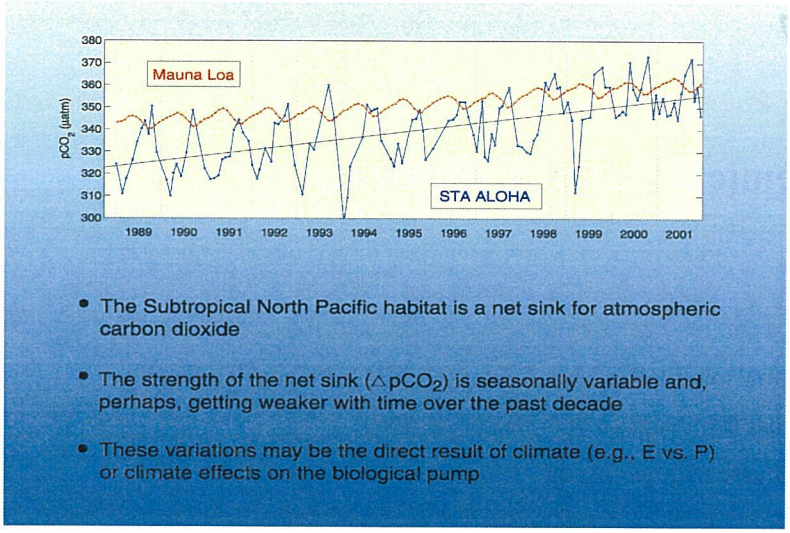

Slide 2 Increase of pCO_2 in the atmosphere and the ocean

The next slide shows that CO_2 increasing in the atmosphere and ocean. The CO_2 increasing speed is higher in the ocean. We will be not going into detail, but this clearly shows that it is important to know how, where, to what extent, the oceans are taking up carbon dioxide from the atmosphere.

7.1.2 Ocean in global cycles of water and materials

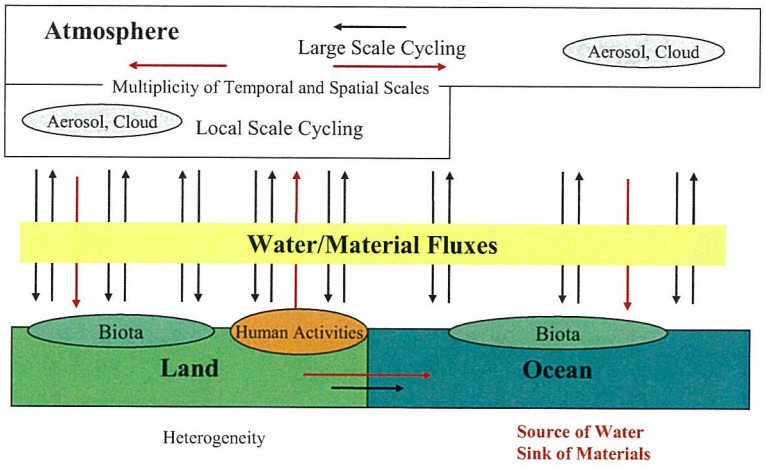

Slide 3 Schematics of global water and material cycles

This slide shows a very much simplified schematic diagram of water and carbon cycles on the Earth surface. Black arrows depict water cycles. Each pair of upward and downward black arrows corresponds to small scale water cycle in each region. Note smaller numbers of pairs in the ocean compared to land are implying less heterogeneity over ocean surface than over the land surface. Horizontal black arrows in the atmosphere and that connects land and ocean is in opposite direction,

indicating global scale water cycle from the ocean to land and back to the ocean through land surface. Red arrows are for fluxes of materials introduced by human activities (e.g., carbon dioxide etc.). It is emitted by human activities being intensified in the land-ocean interface, and transported into the ocean either via land through river water or via atmosphere through dry fallout or wet deposition. We have biology in the surface of ocean and land. Since biota requires water and materials the biota stands in the interface of water and material cycles. Ocean is the largest sink of water as well as carbon cycle. It is important to note that the water cycle has two meanings; one is as energy (heat) cycle and the other is as material cycle. This is due to water's capability to dissolve materials in it. How fast is the water cycle? Slide 4 shows schematics of global water cycle. Out of the total annual evaporation of 320 x 10^3 km^3 most of water is precipitated back to the ocean surface and only about 10 percent is transported to land.

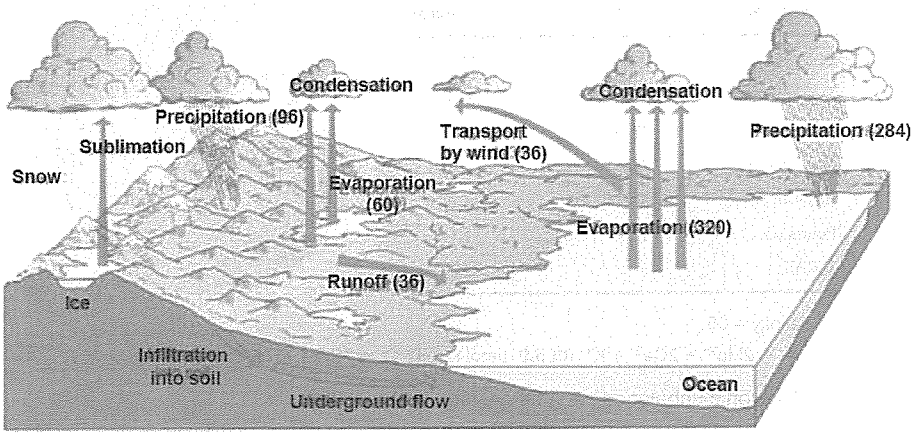

Processes of Water Cycle on the Earth Surface: Numbers are for Annual Fluxes ($10^3 km^3$)

Slide 4 Schematics of global water cycle

Table 1 shows abundance of water in various reservoirs on Earth surface. Note that the ocean has 97% of total water on Earth surface, and the residence time of water is calculated to be 1350 x 10^6 km^3/320 x 10^3 km^3 y^{-1} = ca. 4000 y.

Table 1 Volume of water in various reservoirs on Earth surface

Reservoir	Volume (10^6 km^3)	Per cent
Oceans	1350	97.3
Glaciers	29	2.1
Aquifers	8	0.6
Lakes and Rivers	0.1	–
Soil moisture	0.1	–
Atmosphere	0.013	–
Biosphere	0.001	–

7.2 Characteristic of the Ocean

7.2.1 Ocean Chemistry

Ocean is the one single largest water pool on Earth. As stated earlier it contains all of the materials transported into ocean as sea salts since its formation some 10 billion years ago. Given the residence time of the water of about 4000 years, the seawater is well mixed during the time. Because of this the seawater contains almost all elements on Earth and the composition is very much similar in the entire ocean. Among the sea salts major constituents are listed in Slide 5,

TABLE 4–3
Major Constituents of Sea Salts

Constituent	*Chemical Symbol*	*Percent by Weight*
Chloride	Cl^-	55.07
Sodium	Na^+	30.62
Sulfate	SO_4^{--}	7.72
Magnesium	Mg^{++}	3.68
Calcium	Ca^{++}	1.17
Potassium	K^+	1.10
TOTAL		99.36

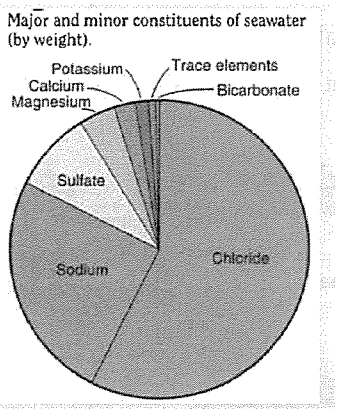

At Salinity = 35,

$Na^+ + 2Mg^{2+} + 2Ca^{2+} + K^+$ (605.0 mmol kg^{-1}) > $Cl^- + 2SO_4^{2-}$ (602.8 mmol kg^{-1})

This ionic unbalance must be adjusted by weak acids.

Slide 5 Major constituents of sea salts and unbalance of major cations and anions

where more than 99% of sea salts is consisted of only 6 ionic forms of strong acids and bases; 2 anions (Cl^- and SO_4^-), mostly derived from volcanic gases, and 4 cations (Na^+, Mg^{++}, Ca^{++} and K^+) , mostly derived from weathering of volcanic rocks. It is important to note that these ionic species are not in balance. In fact, at a salinity of 35, total cations are 605.0 mole kg^{-1} and total anions are 602.8 mole kg^{-1}, hence this imbalance should be adjusted by weak acids. The amount of excess cations is called alkalinity.

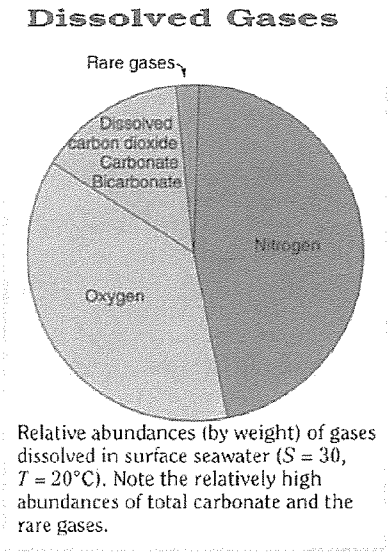

Slide 6 Relative abundance of dissolved gasses in seawater

Slide 6 shows relative abundances of gases dissolved in seawater at temperature of 20 ℃ and salinity of 30. It should be noted here that the solubility of gases are high in low temperature. Seawater contains very large amount of carbon dioxide. This is because carbon dioxide, together with boric acid, serves to compensate the ionic imbalance, and hence being called as the major agent in total alkalinity defined as follows;

$$\text{Total alkalinity} = CO_3^- + 2CO_3^{2-} + B(OH)_4^- + OH^- - H^+.$$

Being a weak acid, the carbon dioxide in seawater exists in several chemical species making the following equilibrium and hence it is called a carbonate system;

$$\underset{\text{Carbon dioxide + water}}{CO_2 + H_2O} \rightleftarrows \underset{\text{Carbonic acid}}{H_2CO_3} \rightleftarrows \underset{\text{Bicarbonate ions}}{H^+ + HCO^{3-}} \rightleftarrows \underset{\text{Carbonate ions}}{2H^+ + CO^{3-}}$$

Among the component of total alkalinity, contribution by carbonate system differs along with chemical equilibrium. When the seawater becomes more acidic, there will be more bicarbonate ion (one electron) resulting in lower alkalinity, and more alkaline there will be more carbonate ion (two electrons) resulting in higher alkalinity.

Biology affects the carbonate system in two ways; one is photosynthesis which converts carbon dioxide gas to organic carbon, and the other is to form calcium carbonate precipitation. The former process has nothing to do with strong acid and bases, hence it does not change alkalinity, whereas the latter process causes reduction of calcium ion concentration, hence it reduces alkalinity.

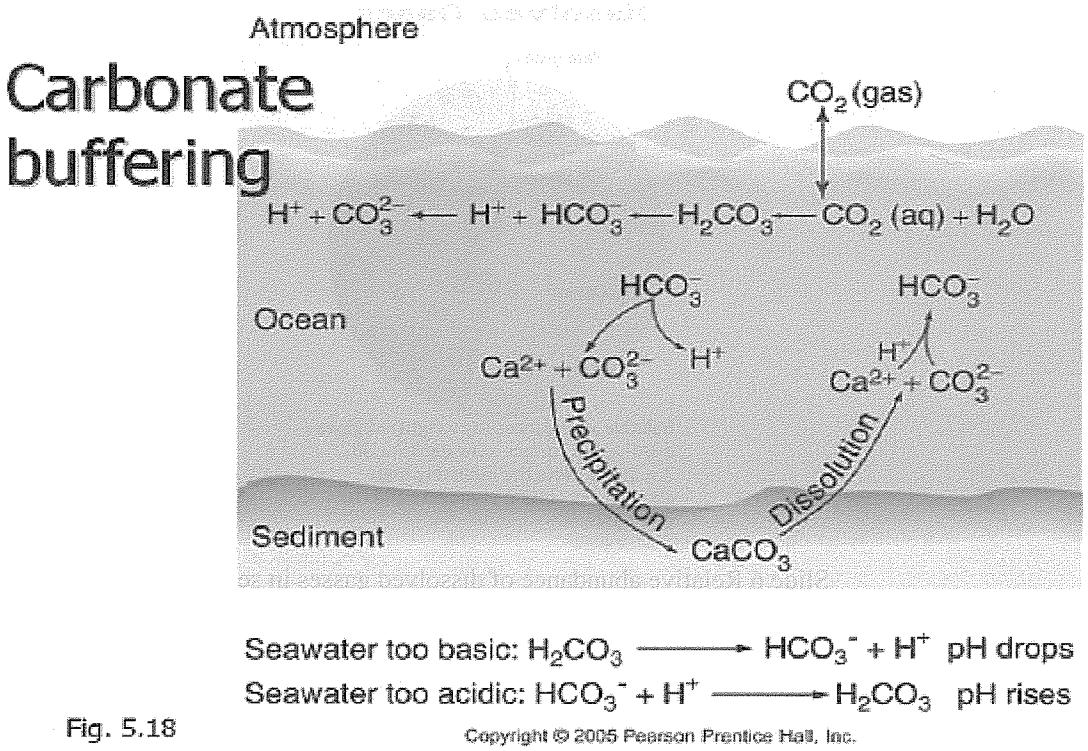

Slide 7 Carbonate system in seawater

When the alkalinity is reduced, the equilibrium of the carbonate system shifts to produce more bicarbonate ion, and results in lower pH and elevated pCO_2 in seawater. In this context, ocean acidification is becoming a major concern as a result of increasing atmospheric pCO_2. In that, increased dissolution of atmospheric CO_2 into seawater results in lowering pH and dissolution of calcium carbonate, which may be fatal to some calcium carbonate shell bearing organisms such as pteropods, foraminifera, sponges, corals, etc.

7.2.2 Ocean Physics

Though in this training course you may already have heard about the physical aspects of the ocean, two important features need to be stressed here: one is that the seawater is stratified by density, and the other is that the ocean can be thought of as composed of two boxes, one shallow and the other deeper boxes.

Slide 8 shows ranges of temperature and salinity of seawater. It is shown that the temperature ranges from -1.5 ℃ to 30 ℃, and salinity from 33 to 37. The reason that salinity has narrow range was given previously. It is important to note that 75 % of entire seawater falls in very small range of temperature and salinity. Since the density of seawater is determined by temperature and salinity the cold saline water is dense and hence it locates in deeper layer.

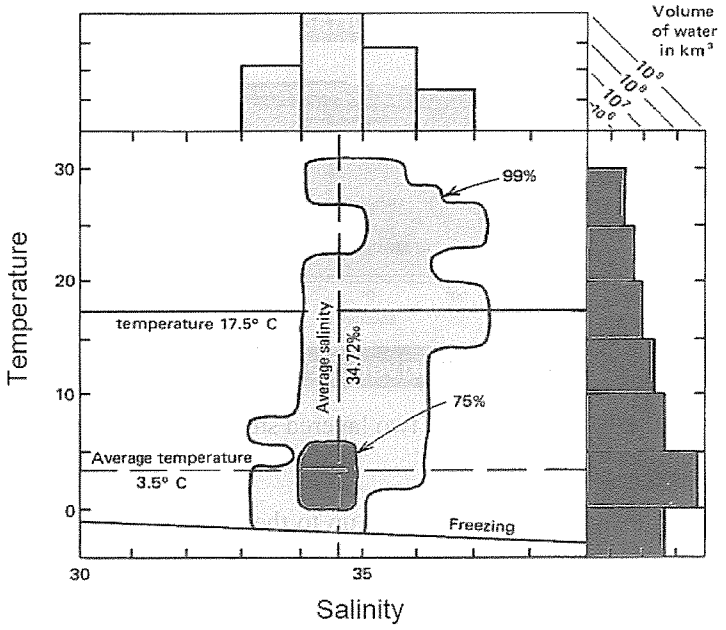

Slide 8 Temperature and Salinity characteristics of sea water

In other words about 3/4 of the entire seawater is in the deep and well mixed. When we see vertical profiles of temperature, salinity, and density it is evident that the seawater can be thought as making two layers. The interface of the upper and lower layers makes sharp gradient with depth and called a thermocline, halocline and phycnocline, respectively.

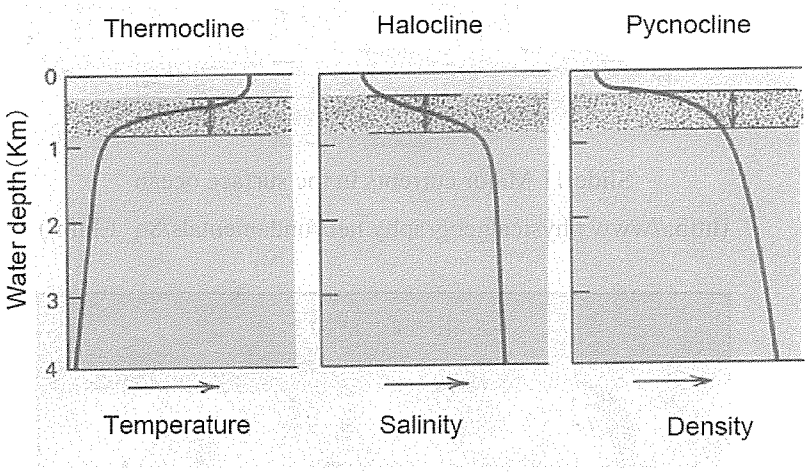

Slide 9 Vertical profiles of temperature, salinity and density

In Slide 8 temperature shows wide range of variation. This partly results from the seasonal and latitudinal variation of surface water in contact with atmosphere. This is depicted in Slide 10.

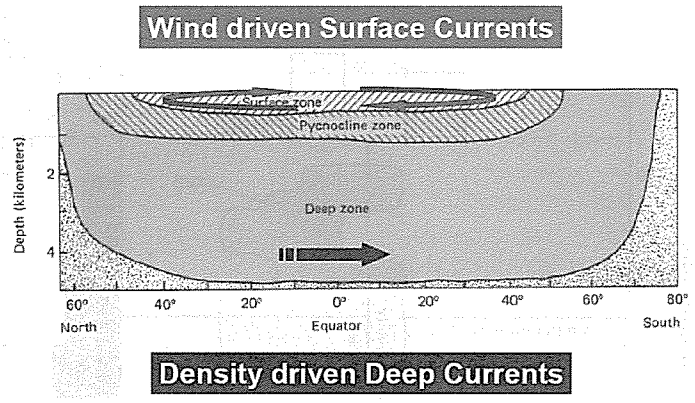

Slide 10 Schematics of two layered structure of the ocean

It is shown that the deep mixed water comes up to the surface only in high latitude polar seas. The upper layer is driven by winds, and the deeper layer by convective overturn. Please refer to the previous lectures for details of the mechanisms of ocean currents generation. Shown here are only the horizontal patterns of surface major currents and the deep water circulation.

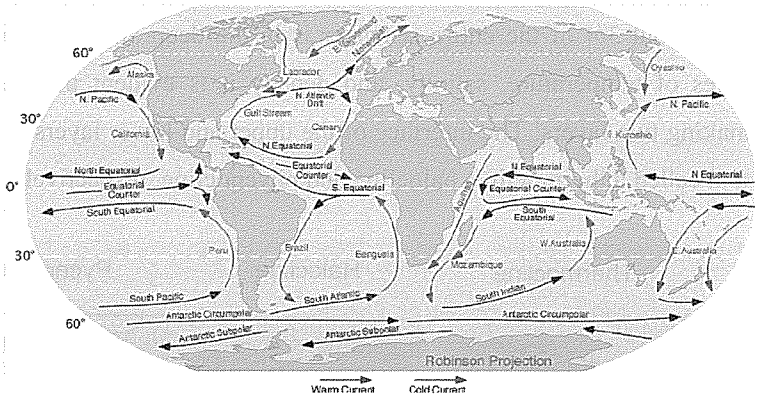

Slide 11 Major currents in the surface ocean
(http://www.physicalgeography.net/fundamentals/8q_1.html)

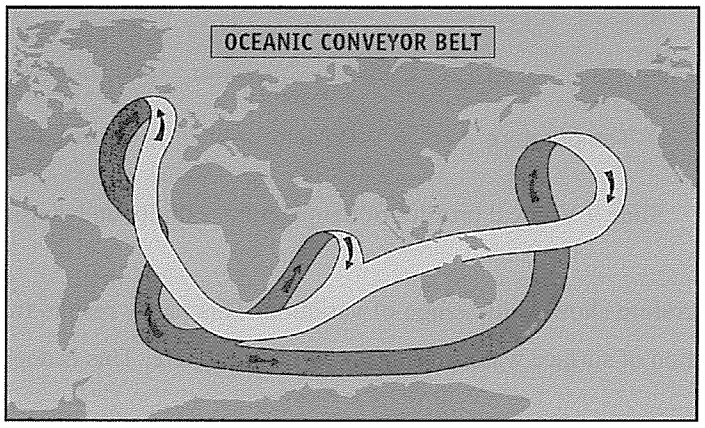

Slide 12 Schematics of deep water circulation (great ocean conveyor belt)

7.2.3 Ocean Biology

7.2.3.1 Plankton are small

Slide 13 compares the land and ocean ecosystems. On land, plants stick out roots into soil for water and nutrients which are needed for primary production utilizing sunlight. Hence all life on land, depending on primary production by plants, is on a relatively thin land surface, where production and decomposition of organic matter takes place together. In the ocean, contrastingly, there is no plane to hold plants in the sun lit shallow layers. Because of this, free floating marine plants, called phytoplankton, adapted their life in several ways to be able to stay in the ocean surface. Amongst them, the most important strategy is to make their body small, and some of them have flagellae to move, have rough surface or even spines to increase drag to water. Being small, phytoplankton have higher surface to volume ratio. This provides advantage for phytoplankton that they could grow (increase their population) rapidly with small amount of resources which are available at low level in shallow seawater. The other contrasting difference to land ecosystem is that the production takes place only in the sun lit shallow layers whereas the decomposition takes place at all depths down to the bottom more than 5000 m deep.

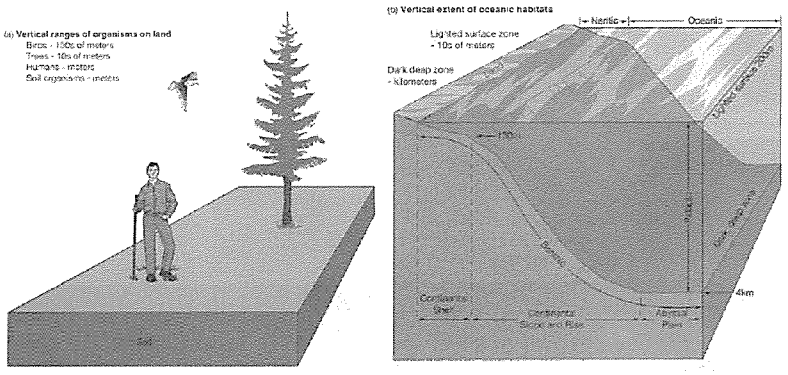

Slide 13 Comparison of Land and Ocean Ecosystems

Similar to the land ecosystem there are organisms which are depending on their energy source for food produced by the primary producers phytoplankton. Since the phytoplankton are small in size, animals must also be small to feed on phytoplankton efficiently.

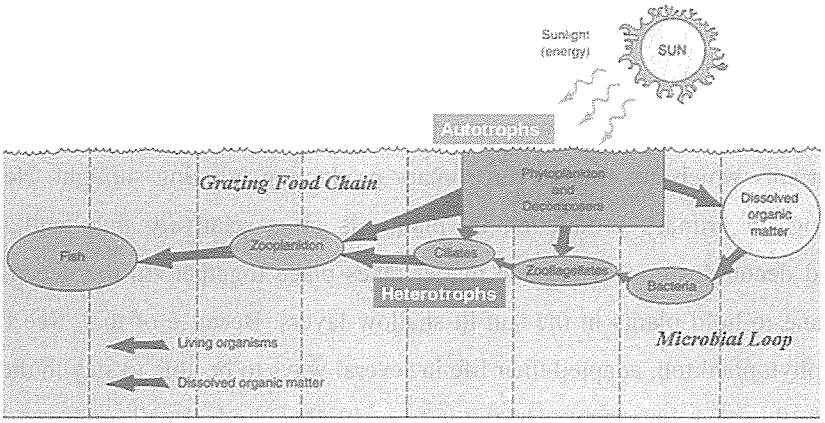

Slide 15 Life in the ocean

Slide 15 shows schematics of energy flow from phytoplankton to zooplankton and fish. Horizontal axis ranges, from right, roughly 0.01 μm to 1m, to the left, on a logarithmic scale. It is important to note that the primary producers (autotrophs) are in the same size range with decomposers such as bacteria, zooflagellates, and ciliates (heterotrophs). Some of the phytoplankton as well as zooplankton are shown in Slide 16.

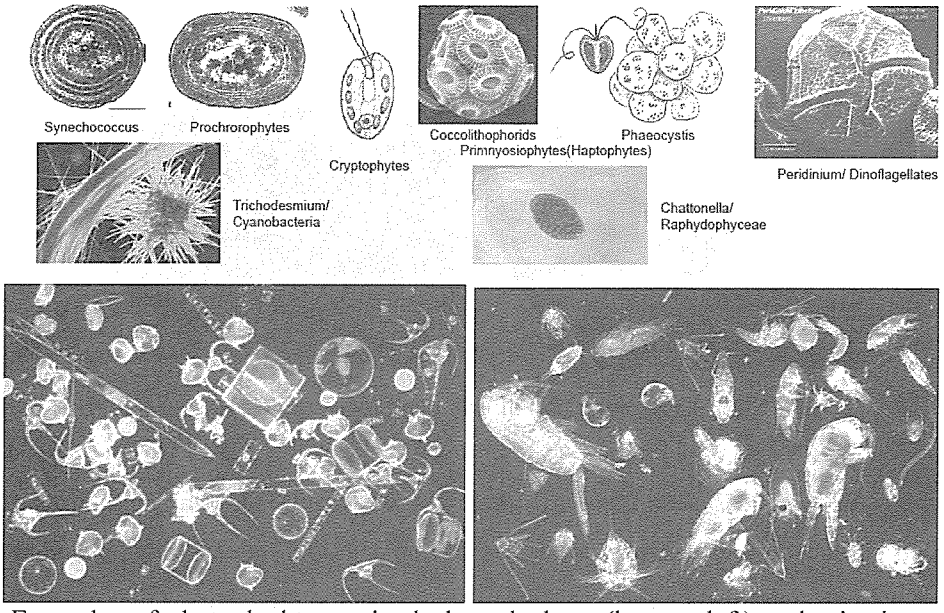

Slide 16 Examples of phytoplankton, mixed phytoplankton (bottom left) and mixed zooplankton (bottom right)

Among them, Prochrorococcus is discovered roughly only 10 years ago and now known as the most abundant phytoplankton in the ocean. The other group of small phytoplankton, Synecococcusis is the second abundant phytoplankton. They are less than one micron diameter and are called picoplankton. A cyanobacterium, Trichodesmium, is famous for its nitrogen fixation. Coccolithophorids are calcium carbonate bearing phytoplankton sometimes form large scale blooms.

7.2.3.2 Production and decomposition are almost in balance

Since the primary producers (phytoplankton) are living together with consumers (heterotrophic organisms) in the euphotic zone, the production (photosynthesis) and decomposition (respiration) are taking place in a coupled manner (bottom left of Slide 17). The standing stock of phytoplankton as seen in the ocean color satellites imagery is the result of its production and consumption by heterotrophs (upper left of Slide 17), and hence it is necessary to have primary productivity data to understand the biogeochemical dynamics in the surface ocean.

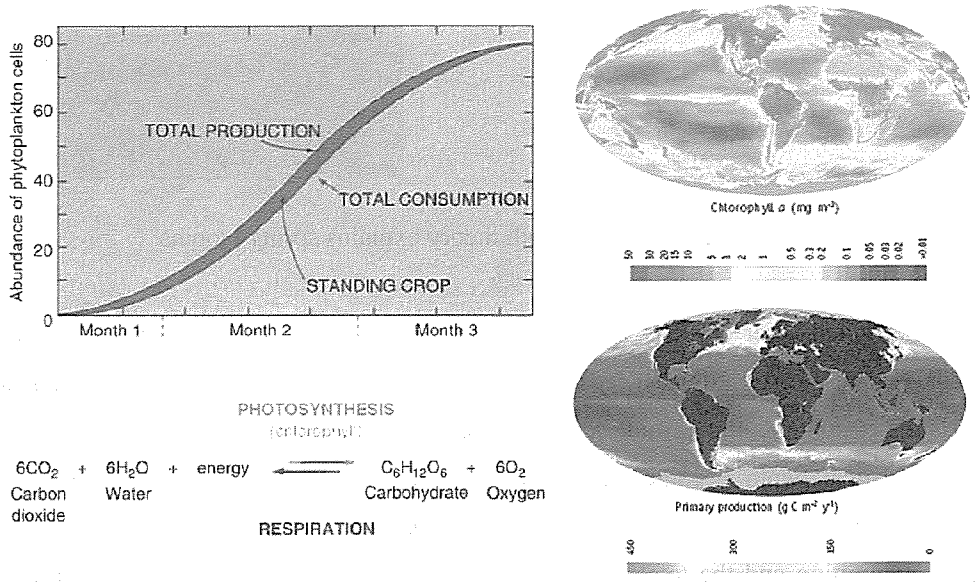

Slide 17 Phytoplankton standing stock result from balance of production and consumption

As stated before, in a water column the photosynthesis takes place only in the euphotic zone, but respiration takes place at all depth range. When we consider the fate of mixed population in a region of question, we need to compare total primary production and respiration integrated in an entire water column. In this way we can define a depth, at that depth the water column integrated production and respiration equals, called the critical depth. While the production takes place in the shallow depths, respiration is mostly carried out by bacteria and hence distribute evenly throughout the water column.

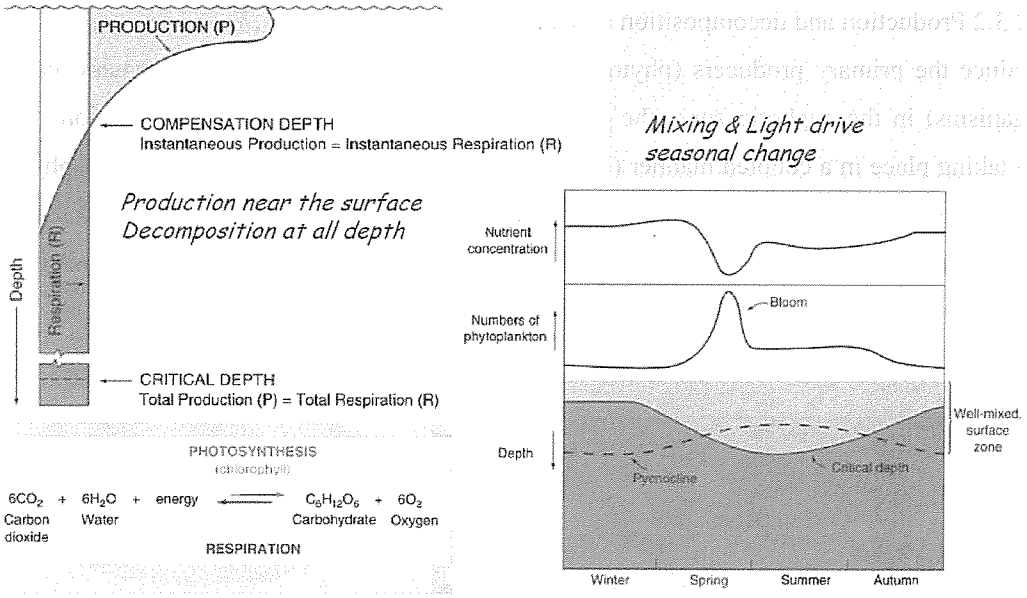

Slide 18 Critical depth theory explains spring blooms

When the mixed layer exceeds the critical depth, produced materials distribute evenly in the mixed layer and respiration exceeds the production, hence total population should decrease. This is the case in the mid latitude seas in winter. In spring the water column becomes stratified and the critical depth become deeper with increasing solar radiation and the mixed layer becomes shallower than the critical depth. This leads to the water column integrated production exceed respiration and the total population increases. This is the so called Sverdrup's critical depth theory, which is satisfactory applied in many cases of bloom formations.

7.2.3.3 Plankton transform materials

Every planktonic organism is a particle, which takes up materials from seawater outside and converts them to high molecular weight cell materials, disintegrate to low molecular weight materials, and then regenerate them again into seawater. Those processes are depicted in the Slide 19, as an idealized cell showing uptake processes in the left, biosynthesis and decomposition in the middle, and regeneration processes in the right. The carbon metabolism is often called an energy metabolism, and is coupled with phosphate metabolism. It is important to note here that phosphate is taken up and regenerated by phytoplankton in the same form, phosphate, whereas the nitrogen is taken up in the forms of nitrate, nitrite, and ammonium, but is regenerated mostly as ammonium.

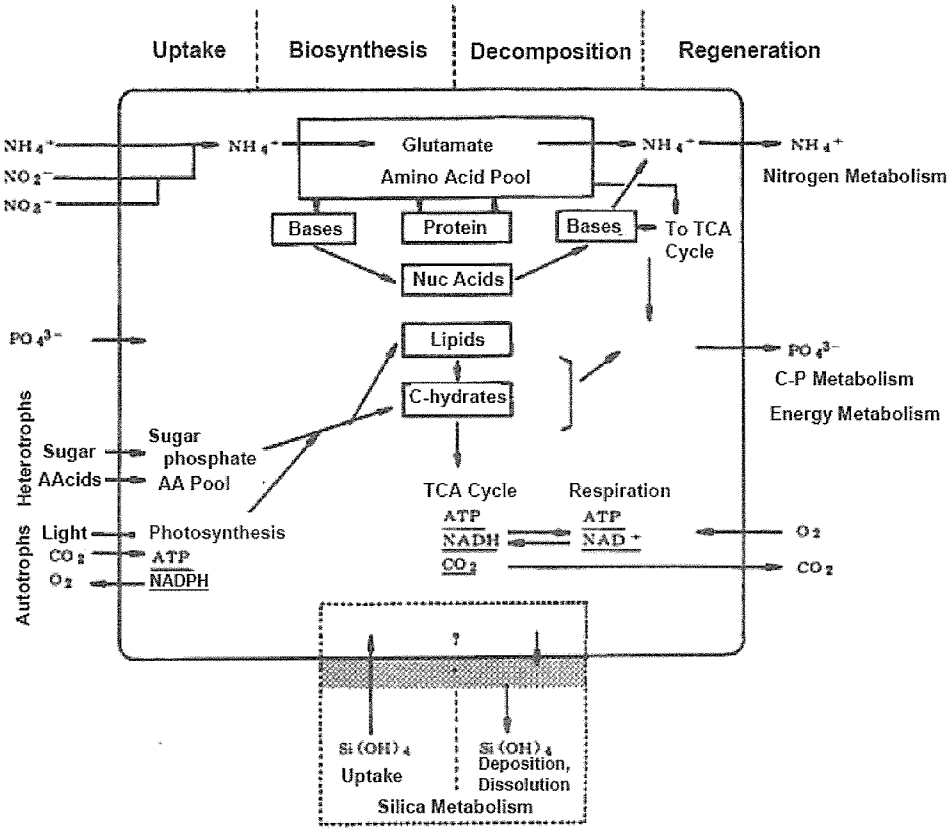

Slide 19 Idealized phytoplankton metabolism

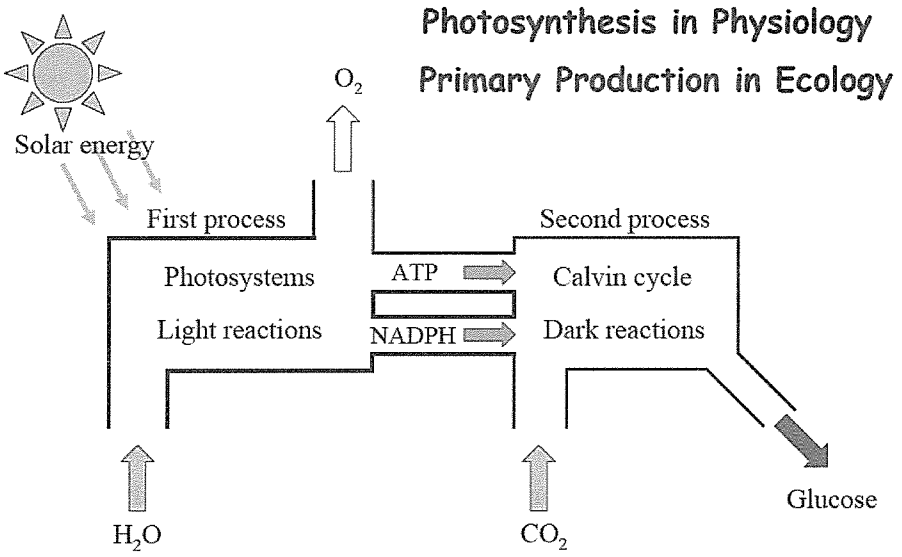

Slide20 Light and dark reactions of photosynthesis

Photosynthesis is the most important process in the biogeochemical cycles in the ocean. The product of the photosynthesis, namely phytoplankton cell by themselves, supports all of the lives in

the ocean. This is why the photosynthesis is called primary production in ecology as well as biogeochemistry. The photosynthesis comprises of two steps of reaction sequences; light reactions and the dark reactions. The light reactions are for energy conversion from sunlight to chemical energy, ATP and highly reactive reducing power, NADPH. In light reactions, oxygen is also evolved from water. The dark reactions are for fixation of carbon dioxide into carbohydrate. The dark reactions take place in cytosol of chloroplast, while the light reactions take place on thylakoid membrane in chloroplast.

For phytoplankton to double their cells they need to take up other resources such as nitrogen, phosphorus, etc. As stated earlier, phosphorus is mostly utilized as phosphate, but nitrogen takes several forms such as nitrate, nitrite, or ammonia. Since most of the seawater is oxygenated, nitrate is the most abundant form in seawater. When phytoplankton utilize nitrate, they need to take up nitrate molecule from outside the cell to inside, and then reduce to the most reduced form, ammonia, before using it for biosynthesis of high molecular weight materials such as protein and nucleic acids. To the contrary, ammonia is the most readily available form of nitrogen to be utilized for biosynthesis. It is important here to note that the nitrogen uptake and reduction requires energy acquired by photosynthesis.

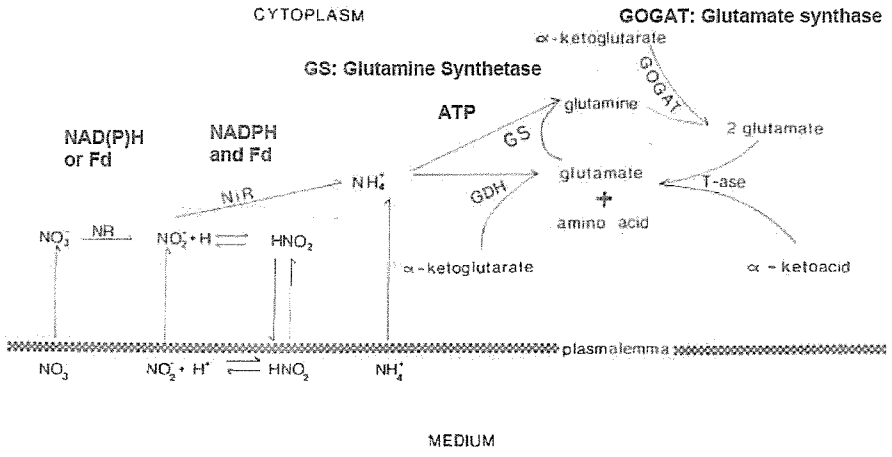

Slide 21 Nitrogen uptake and metabolism in phytoplankton cells

7.2.3.4 Particles sink

In the context of biogeochemical cycles, the most important role of organisms in the ocean is to produce sinking particles that transport materials from the surface production regime to deeper layers. It is thought that the fecal pellets of zooplankton may serve as important carrier in this vertical materials transport.

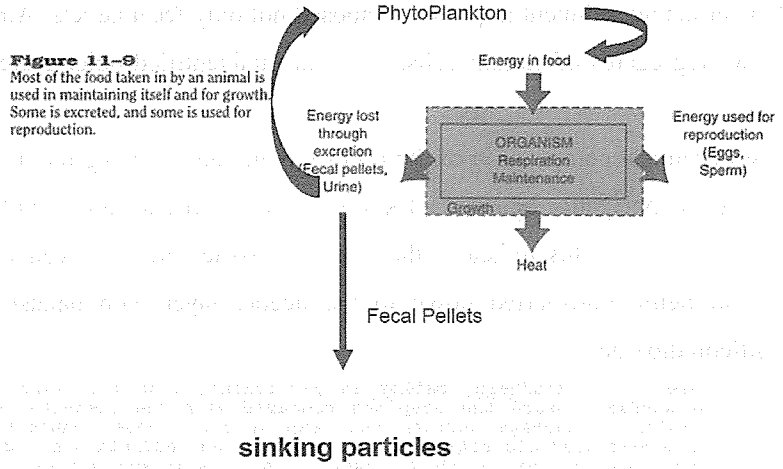

Slide 22 Relationship between phytoplankton and zooplankton.

Slide 22 shows how the energy of phytoplankton eaten by zooplankton is utilized for growth, reproduction, excretion of zooplankton. The important point here is that the fecal pellets sink but urine, in most cases ammonia, is utilized again by phytoplankton in the euphotic zone. The sinking particles can be collected by devices called sediment traps. Slide 23 shows one of the sediment traps together with a result showing very sporadic nature of the vertical flux obtained in highly productive subarctic Pacific off Japan in spring.

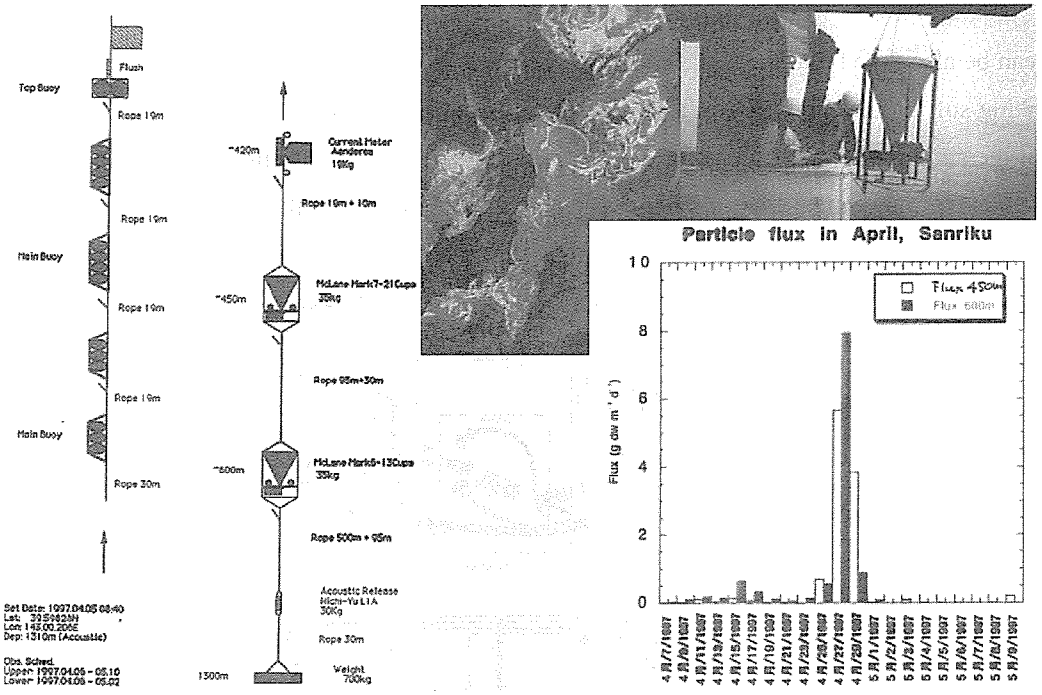

Slide23 A sediment trap experiment off Sanriku, Japan

The collected materials by sediment traps are composed not only fecal pellets. Amorphous materials like marine snow, aggregates of diatom cells, and other unidentified objects are often seen in the trapped samples.

Slide 24 shows chemical composition of the trapped materials. The organic materials, making up the soft tissues, have C:N:P ratios of 105:15:1 known as the Redfield Ratio, and the hard parts have C:Ca:Si ratios of 26:26:50. This indicates that the soft tissues are produced in the near surface euphotic zone and being transported down to the deeper layer with ballast made of calcium carbonate and silicon dioxide.

Table 1-2. "Redfield" ratios in particulate debris falling from the surface toward the deep sea compared with the elemental composition of average surface and deep water. These compositions are termed Redfield ratios in honor of Alfred Redfield who did the early work on this subject (346). For comparison actual P:N:C ratios measured in material sieved from surface waters are shown. These latter results were taken from a summary by Goldman (692).

		P: N: C : Ca:Si
Particulate Debris	Soft Tissue	1:15: 105: 0: 0
	Hard Parts	0: 0: 26: 26:50
	Composite	1:15: 131: 26:50
Sea Water	Deep	1:15:1000:5000:50
	Warm Surface	0: 0: 869:4974: 0

	P: N: C
Western North Atlantic (Jan. '62	1: 5: 59
Western North Atlantic (Apr. '62)	1:13: 68
Equatorial Atlantic	1:21:163
North Pacific Gyre	1:29:410
Central North Pacific	1:18:152

Slide 24 Composition of sinking particles compared with sea water and particulate materials in surface waters of various parts of the world oceans

It can be also noted that the C:N:P ratio of 1000:15:1 in deep water has same proportion of N:P with sinking soft tissues, and the surface warm water is deprived of phosphate and nitrate. This indicates that the sinking particles are responsible for the distribution of nutrients in sea water. In the bottom of Slide 25, the vertical flux of sinking particles is combined with the deep water current along with the Great Conveyor Belt.

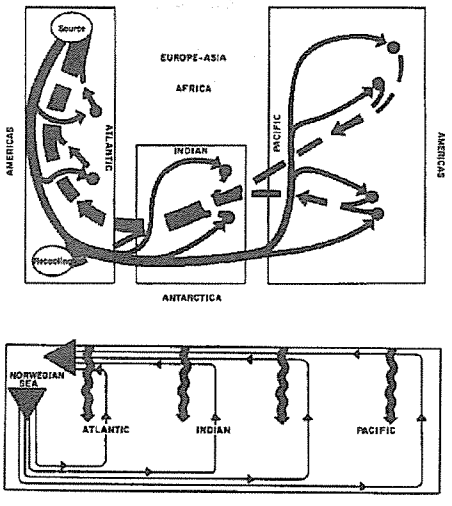

Slide25 Sinking particle fluxes combined with Great Conveyor Belt

Implication from this is that the organic matter in the soft tissues and minerals of hard parts (calcium carbonate and opal) are added onto the conveyor belt by the vertical fluxes and decomposed on it when it moves downstream. The results will be increases of regenerated nutrients such as phosphate, nitrate, silicate and decrease of dissolved oxygen from the upstream to downstream. In fact the above trend can be clearly seen in Slide 26.

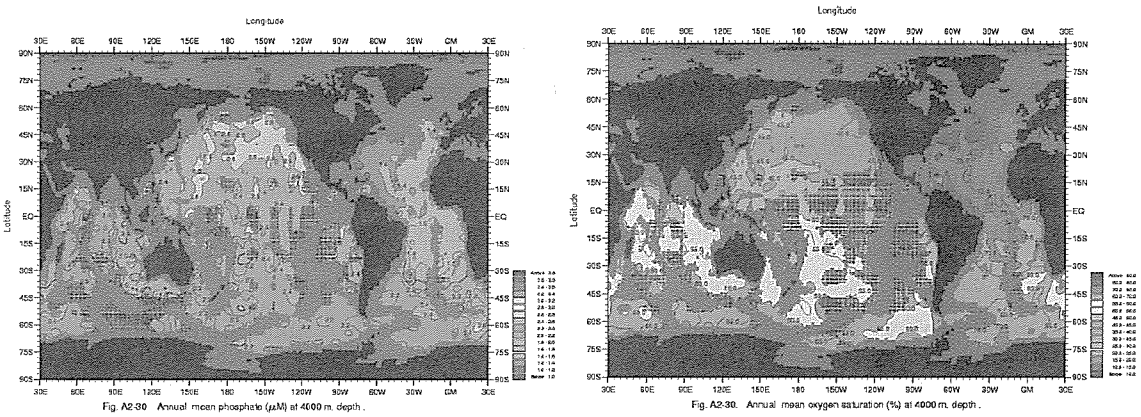

Slide 26 Annual mean phosphate (left) and per cent saturation of oxygen (right) at 4000m depth

7.3 Global Carbon Cycle

3.1 Outline

Slide 27 shows schematics of global carbon cycle averaged for 1980s. In the context of the land and the ocean comparison of the primary productivity, land primary productivity is 60.0 PgC/y and the ocean productivity is 45 PgC/y.

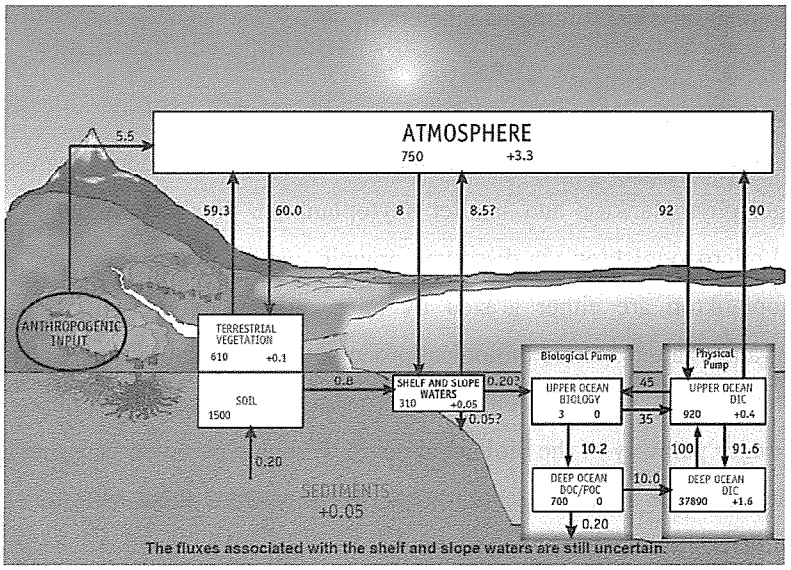

Slide 27 Average global carbon cycle in 1980s.

The land biomass (610 PgC) is ca. 200 times larger than that of ocean (3 PgC), and hence the turnover time of land biomass is ca. 10 years, 200 times slower than that of the ocean (less than one month). In this lecture let's look over the shelf and slope water just for simplicity. As previously shown the ocean is divided into two layers; the upper ocean and the deep ocean. Two mechanisms are shown for the transport of atmospheric carbon dioxide to the deep ocean, the biological pump and the physical pump.

The biological pump is consisted of two steps, one to convert dissolved carbon dioxide into organic carbon by primary productivity, and the other to transport organic matter to the deep ocean as sinking particles flux. In Slide 27 the annual vertical flux of organic carbon is estimated to be 10 PgC/y, approximately 20% of the primary production. The air-sea exchange of carbon dioxide is carried out by the physical pump. The physical pump is also called a solubility pump, where the solubility of carbon dioxide in seawater is higher in cold water and the lower in warm water. Since the cold water is heavy, the cold surface water rich in carbon dioxide resulted from vigorous sea-air heat flux sinks down to the deep ocean, and as a result transport atmospheric carbon dioxide to the deep ocean. It should be noted however that the air-sea CO_2 flux is dependent on the difference of partial pressure of carbon dioxide (pCO_2) in air and surface water, and the sea surface pCO_2 is determined not only by temperature but by primary productivity.

Slide 27 also shows that the net air-sea flux of carbon dioxide (ca. 2 PgC/y) is a small difference of CO_2 fluxes from the atmosphere to the ocean (92 PgC/y) and from ocean to the atmosphere (90 PgC/y). Though the quantitative estimates of the net air-sea flux is a prerequisite for any kind of climate change models, it is extremely difficult to obtain the quantitative estimate of air-sea fluxes of carbon dioxide on a global scale. This is mainly because of large spatial and temporal variability of air-sea fluxes of carbon dioxide resulting from complex behavior of regional scale biological pumps to regional physical forcing parameters.

7.3.2 Biological Pump

Slide 28 shows components of the biological pump. Primary producers are divided into two size classes, larger phytoplankton and smaller phytoplankton. Smaller phytoplankton are coupled with bacteria and microzooplakton via dissolved organic matters in a way known as the microbial loop. Large phytoplankton are either grazed by microzooplankton or enter into microbial loop via dissolved organic matters. These biological processes in upper layers lead to generation of dissolved and particulate organic matter. Though in a previous section only the sinking particle flux is dealt with as the major pathway of the biological pump, it should be noted here that the dissolved organic matter generated in the upper layer are transported downward along with the concentration gradient due to eddy diffusivity.

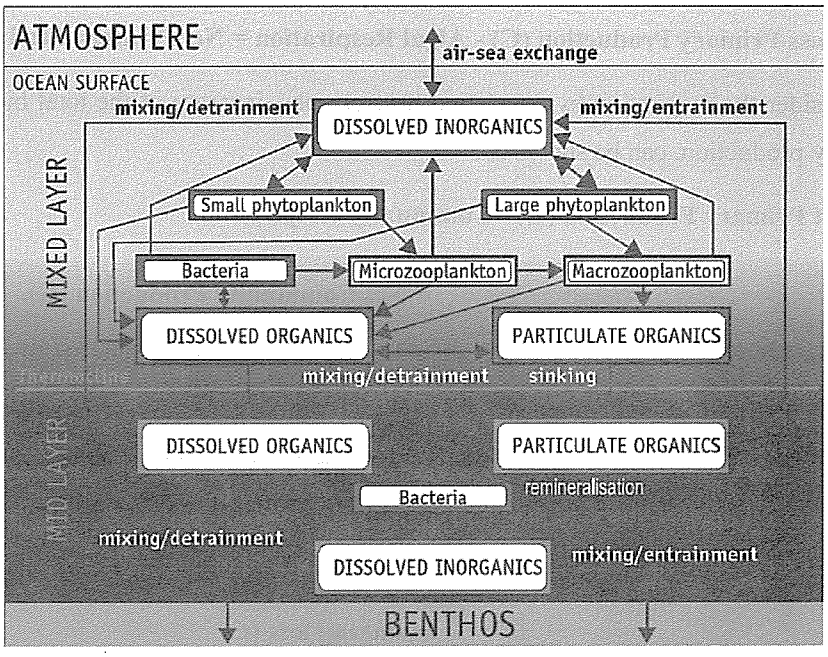

Slide 28 Biological Pump and its components

It is now widely accepted that when the microbial loop prevails in the upper layer, as is the case in oligotrophic open oceans, vertical transport of organic carbon via dissolved organic matter occupies major portion of the flux which is normally small as compared with the particle flux. Contrastingly when the large phytoplankton predominates and the grazing food chain is enhanced, as is the case in spring bloom in temperate seas, the particulate flux will result in the high downward transport of organic carbon. Since the population dynamics of phytoplankton is regulated by the way of supply of nutrients and light, and the co-habiting zooplankton populations, those factors affect the relative importance of vertical flux of organic matter via dissolved organic matter and the particulate organic matter. Amongst those factors the water column stratification is the most important factor regulating the growth condition of phytoplankton in euphotic zone.

7.3.3 Efficiency of the Biological Pump

In terms of carbon cycle, the biological processes in the euphotic zone can be seen as the tight coupling of primary production and respiration. Here we consider the efficiency of the biological pump in the upper ocean. The efficiency is defined as the ratio of organic carbon transported out of the upper ocean to the amount of organic carbon transferred to heterotrophs from autotrophic phytoplanktonic algae. Since phytoplankton do respiration as well as photosynthesis, some part of the total organic matter produced by photosynthesis, the gross primary production, is respired back to carbon dioxide. Thus the organic carbon transferred to heterotrophs from phytoplankton, the net primary production, can be written as;

Gross Primary Production (C) - Algal Respiration = Net Primary Production (C).

When we consider the respiration by coexisting heterotrophs, increase of the total biomass, *i.e.* the net community production, can be shown as;

Net Primary Production (C) - Community Respiration

= Net Community Production (C).

If the net primary production (C) equals to the community respiration, the net community production (C) becomes 0, hence the total biomass will be kept constant. In the real ocean, part of the produced organic matter is lost from the surface productivity regime as a sinking loss. Therefore the net community production is diverted to gain in and loss from the upper ocean as follows;

Net Community Production (C) = Increase of total euphotic biomass (C)

+ sinking loss (C)

Primary production is not limited to carbon production. It is always associated with uptake of nutrients such as nitrogen, phosphorus, etc. Among the nutrients nitrogen is often considered as the limiting nutrients in the ocean. Nitrogenous nutrients in sea water are in the forms of nitrate, nitrite, and ammonia, and nitrate is the most abundant in oxygenated seawater. As shown previously while ammonia is regenerated in the upper ocean, nitrate is produced from ammonia only below the euphotic zone. Hence, in terms of nitrogen, the gross production can be divided into to categories, new and regenerated production, as

Gross Primary Production (N) = New Production (N)

+ Regenerated Production (N),

where in most cases

New Production (N) = Nitrate Uptake

Regenerated Production (N) = Ammonia Uptake.

Since algal respiration does not result in excretion of ammonia,

Gross Primary Production (N) = Net Primary Production (C).

When the heterotrophic respiration leading to ammonia excretion equals to algal uptake of ammonia,

Community Respiration (C) = Regenerated Production (N),

and then,

Net Community Production (C) = Increase of total euphotic biomass (C)

+ sinking loss (C)

= New Production (N).

Since the total euphotic biomass (C) can be considered being kept constant in a proper temporal and spatial scale, the above equation means that the new production, *i.e.* in most cases nitrate uptake, equals to the sinking loss term (C).

The efficiency of the biological pump can be written as,

Efficiency of biological pump = Sinking loss (C) /Net primary production (C)

Since the sinking loss (C) term equals to new production (N) in steady state, the efficiency of the biological pump can be given by,

Efficiency of biological pump = New Production (N) /(New Production (N)+Regenerated Production (N))

= f-ratio,

which is known as the f-ratio. The sinking loss (C) term includes loss both by dissolved and particulate organic matters. If we measure the sinking loss (C) by the sediment trap experiments, the efficiency of the biological pump by the sinking particles flux can be defined as the e-ratio,

e – ratio = Export particle flux (C) / Net primary production (C).

The e-ratio equals to f-ratio when the contribution of the dissolved organic carbon flux is very small compared to the sinking particles flux.

In the current consideration only the organic carbon is dealt with. As stated earlier the biologically produced particles contain inorganic carbon as well. Because of this the biological pump can be classified further into hard tissue (carbonate) pump and soft tissue (organic carbon) pump. In the hard tissue pump, when the calcium carbonate is formed it leads to the decrease of alkalinity, decrease of the pH, and hence increase of pCO_2. This is in the opposite direction to the soft tissue pump. The ratio of fluxes of calcium carbonate to organic carbon is called a rain ratio,

Rain ratio = [calcium carbonate flux] /[organic carbon flux].

It is important to know the rain ratio to assess the role of the biological pump in the global carbon cycle especially on geological time scales.

7.3.4 Air-Sea Exchange of CO_2

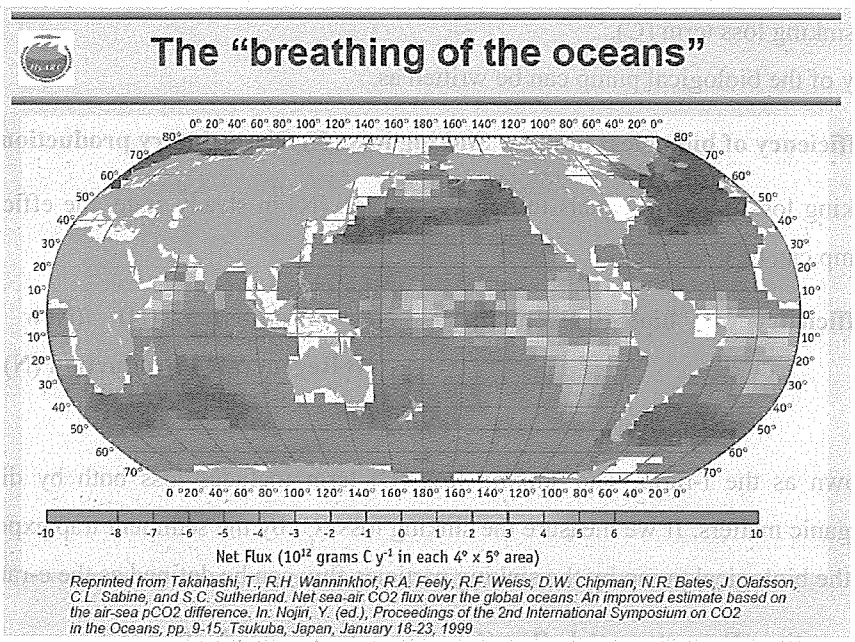

Slide 29 The breathing of the oceans

The air-sea exchange of CO_2 is primarily dependent on the difference of the CO_2 partial pressures between the atmosphere and the ocean. Due to large temporal and spatial variability of the biological and physical pumps, the air-sea exchange of CO_2 shows great temporal and spatial variability. The large spatial variability can be seen in Slide 29, showing the air-sea flux estimated from the compiled ship-based observations.

Considering the oppositely directed hard tissue and soft tissue pumps of the biological pump, it is important to know the effect of rain ratio on the air-sea exchange of CO_2. The Revelle factor, named after Roger Revelle, is the ratio of relative change in atmospheric [CO_2] to the relative change in DIC in seawater;

$$\mathbf{RF = d[CO_2]/[CO_2]\ /d[DIC]/[DIC].}$$

The Revelle Factor varies from 8 to 15 with realistic values of temperature, salinity, alkalinity, and pCO_2, and is affected by the rain ratio. If the rain ratio parameter (γ) is defined as,

$$\textbf{Rain ratio parameter } (\gamma) = \mathbf{CaCO_3 \text{ flux} / (POC \text{ flux} + CaCO_3 \text{ flux})},$$

The Revelle Factor will be 0 (neutral) at $\gamma = 0.63$, positive (uptake) at $\gamma > 0.63$ and negative (out gassing) at $\gamma < 0.63$ under realistic conditions of temperature (25 C), salinity (35), DIC (2 mM) and pCO_2 (360 μ atm). It is predicted that the larger calcium carbonate flux reduces CO_2 uptake to the ocean and leads to CO_2 out gassing from the ocean to the atmosphere if the rain ratio exceeds certain level.

References

Climate Change (1995): The Science of Climate Change, Cambridge University Press. ISBN-0521 56436 0.

Climate Change (2001): The Scientific Basis, Cambridge University Press. ISBN 0521 01495 6

CO_2 in Seawater: Equilibrium, Kinetics, Isotopes: R.Z. Zeebe, and D. Wolf-Gladrow, Elsevier. ISBN-0-444-50946-1.

Ocean Biogeochemistry and Global Change: B.M.Baliño, M.J.R. Fasham and M.C. Bowles (eds.), IGBP. ISSN-1650-7770

Ocean Biogeochemical Dynamics: J.L. Sarmiento and N. Gruber, Princeton University Press. ISBN-13: 978-0-691-01707-5.

The Physiological Ecology of Phytoplankton: I. Morris (ed), U. California Press. ISBN-978-0520043084

The Oceanography: A view of the Earth, 5th edition. M.G. Gross, Prentice Hall. ISBN-0-13-62974-0.

The Oceanography: A view of the Earth, 7 th edition. M.G. Gross and E. Gross, Prentice Hall. ISBN-0-13-231788-5.

Tracers in the Sea: W.S. Broecker and T.-H. Peng, El Digio Press. ISBN-978-0961751104

Chapter 8

Changes of Biogeochemical Cycle in the Ocean

Hiroya Sugisaki
National Research Institute of Fisheries Science, Fisheries Research Agency
2-12-4 Fukuura, Kanazawa, Yokohama, Kanagawa 236-8648, JAPAN
e-mail: sugisaki@affrc.go.jp

8.1 Introduction

On the earth, carbon transportation is controlled not only by physical process but also biological process. In the biological process, organic carbon made from atmospheric carbon by photosynthesis is transported by migrations of creatures or through food web. In the ocean, organic carbon is transported not only horizontally but also vertically by creatures' passive or active movements. This vertical transportation makes separate carbon from atmosphere. Therefore, the ocean has an important role to absorb carbon dioxide (the most serious greenhouse gas) through various biological processes. Phytoplankton synthesize carbon dioxide in the surface layer and are mainly consumed by zooplankton. The subsequent destination of the carbon depends on the species and ecology of the zooplankton. Small zooplankton distributing only shallow layer produce small fecal pellets and they usually degrade in the shallow layer. Therefore carbon dioxide is regenerated around the sea surface/atmosphere interface. Large zooplankton produce larger fecal pellets which quickly sink into the deep layer. Large plankton are also selectively consumed by large predators, such as fish, whales and sea birds. Large predators can extensively swim both horizontally and vertically, and their bodies sink rapidly after their death. In these processes, inter-specific relationships affect the potential effect of the ocean to absorb carbon dioxide into the deep layer. Besides, many species of zooplankton and micronekton, which are abundant organisms in the ocean, performs vertical migration. Vertical migration has an effect for rapid vertical transportation of organic carbon between sea surface and deep layer.

Outline of biological processes of carbon cycle in the ocean, especially the role of vertical migration of zooplankton, long-term variation of zooplankton community, and frontier research on mesopelagic ecosystem, are introduced in this section.

8.2 Zooplankton vertical migration

8.2.1 Ontogenetic vertical migration

In the subarctic area of the North Pacific, genera *Neocalanus* and *Eucalanus* are dominant copepods. They perform characteristic vertical migration. They are spawned in the deep layer and the eggs ascend to shallow layer and hatch. The hatched larvae grow in the phytoplankton rich shallow layer (shallower than 100m depth) from early spring to early summer, highly productive season in the subarctic ocean. The larval stage copopepods consume primary producer, phytoplankton, and then, they sink to the deep layer (deeper than 500m depth) after summer season. From late summer to winter, they stay in deep layers (often deeper than 1000m depth), being in dormant stage. It means that they eat nothing anymore and prepare to mature. After they spawn, they die and their body may be consumed in deep layer. This is the lifecycle of ontogenetic vertical migrant. Consequently, this ontogenetic vertical migration has an effect to transport the organic carbon which is produced in the shallow layer by phytoplankton to deep layer. Harrison *et al* (2004) estimated that 0.16GtC/year was transported by ontogenetic migration of *Neocalanus* copepods in the world.

8.2.2 Diurnal vertical migration

It is well known that many species of zooplankton perform diurnal vertical migration. Usually, diurnal vertical migrant ascend to shallow layer and consume low trophic level organisms during night, and descend to deep layer during daytime. The range of migration is narrow compared to the ontogenetic migration generally, and it has the effect of not only to draw down but also draw up the carbon flux. Even though the efficiency of vertical transportation by diurnal migration are lower than that by ontogenetic vertical migration, the mass of transported carbon is not negligible, because of high frequency of migration (once a day) and high abundance of diurnal vertical migrant.

Metridia copepods are representative diurnal vertical migrant in the subarctic water. The amount of downward transportation to 150m depth of carbon by diurnal vertical migration of *Metridia* copepods is estimated to be as good as that by ontogenetic migration of *Neocalanus* copepods (Kazutaka Takahashi, Tohoku National Fisheries Research Institute, Fisheries Research Agency, in preparation).

8.3 Long term variation of zooplankton community

In the long-range view, the biological process in the ecosystem is not constant. The long-term variations of abundance or species composition of zooplankton are observed generally in the world ocean (*e.g.* Roemich and McGowan 1995; Edwards and Richardson 2004; Richardson and

Schoeman 2004). Since it is thought that there are interactions between climate change and ecosystem structure, research on the mechanisms of long-term variation of zooplankton ecosystem affected by climate change is necessary. In order to monitor the relationships between climate change and biological processes, extensive zooplankton samples which have been collected over a long time period are necessary. Such zooplankton collections are quite rare in the world. In Asian areas, especially, only a few data sets have been known. One of the zooplankton sample sets that have been collected in the western North Pacific is called the Odate Collection. As an example of research on the approach of long term variation of ecosystem in relation to physical oceanography or climate change, the outline of the research project using Odate Collection is introduced in this paragraph.

More than 20000 zooplankton samples called the Odate Collection have been collected off eastern Japan over a period of for more than 50 years since the 1950s (Fig.8.1). All of them have been assembled in Tohoku National Research Institute, and the report on long term variation of wet weight of these zooplankton was published by Dr. Kazuko Odate (Odate 1994)(Fig.8.2) . This is the first report on the long-term variation of zooplankton biomass in the western North Pacific.

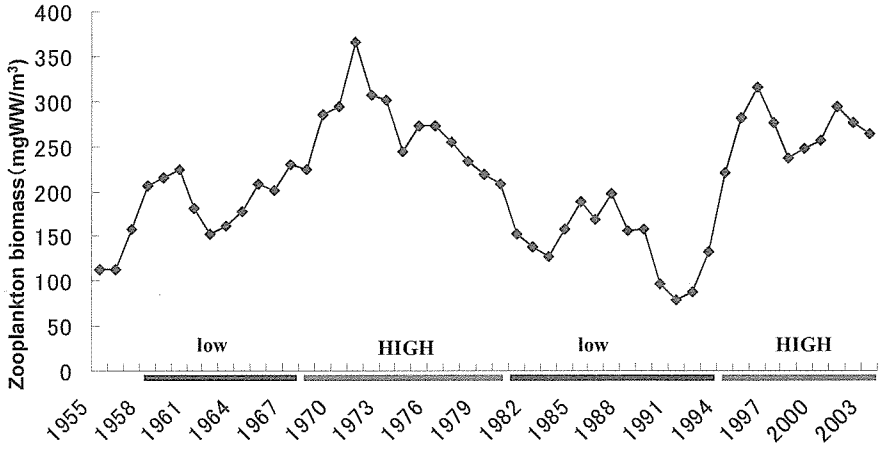

Figure 8.1 Long-term variation of zooplankton biomass collected in Oyashio cold water region (revised from Odate,1994)

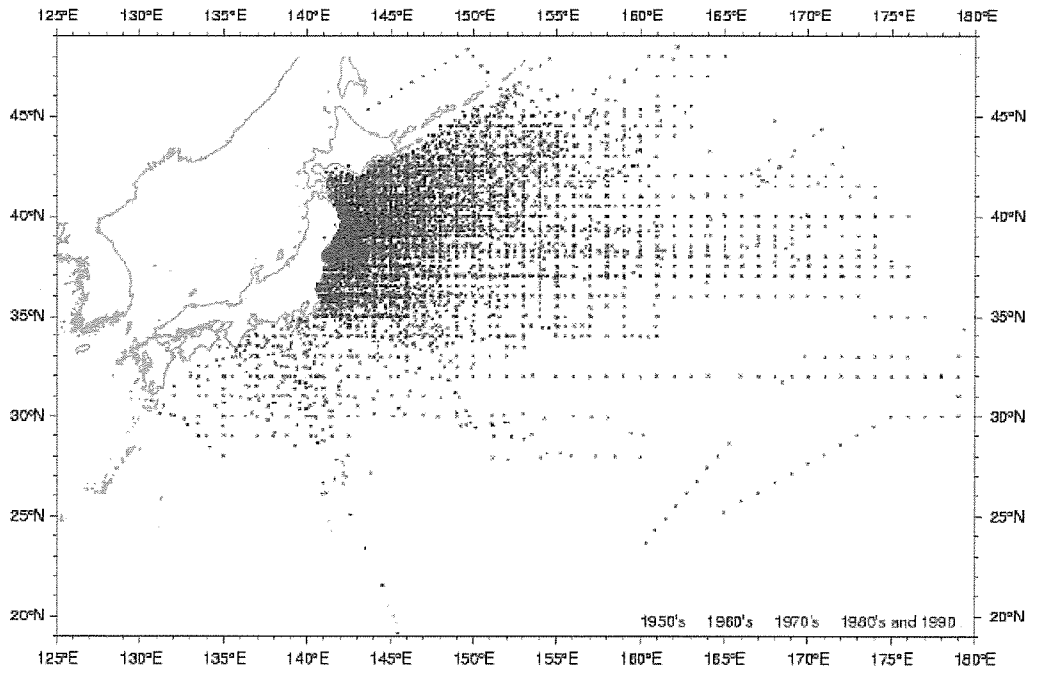

Figure 8.2 Sampling stations of Odate Collection.

Zooplankton of the Odate Collection were collected obliquely from 150m depth using conical zooplankton net (0.33mm mesh size, 45cm mouth diameter). From more than 20000 samples have been accumulated and stocked at Tohoku National Fisheries Research Institute, Fisheries Research Agency (3-27-5 Shinhama-cho, Shiogama city, Miyagi. 985-0001, Japan). Out of these samples, 2885 samples were selected for species composition analysis. 1527 samples were collected in the Oyashio region (water temperature at 100m depth was less than 5 °C) during 1960 and 2002. Other 1358 samples were collected in Kuroshio-Oyashio transition region (5°C< water temperature at 100m depth< 15°C) during spring and summer season (from April to September). Copepods were sorted from these samples, and classified into species, or into growth stages of copepodite larvae for abundant species (genus *Noocalanus*, *Eucalanus, Metridia* and *Calanus*) and counted. Body length of 10 specimens of three dominant species (*Neocalanus plumchrus*, *N.flemingeri* and *N.cristatus*) from each zooplankton samples were measured. From the 1527 zooplankton samples collected in Oyashio region, 174 species of copepods were detected, and 236 copepods species were detected from 1358 samples collected in Kuroshio-Oyashio transition region. Finally, the more than 40 year database of species composition of zooplankton was established. This is the biggest and precise database of biological monitoring in the western North Pacific. The database of this research is planned to be open to the public being available for anyone who is researching on ocean ecosystems. When the database system will have been completed and it will be open to the public, information of long-term variation of oceanic zooplankton community will be useful for the various researches of

global ecosystem scientists in the world.

Using the dataset of zooplankton established in this research project, the mechanism of long term variation of oceanic ecosystem induced by climate and geophysical processes has been analyzed. Decadal variation of copepod biomass was well observed and biomass has relatively low during 1980s compared with 1970s and 1990s. It was found that the biomass of *Neocalanus* spp., dominant copepods in Oyashio region, was relatively low during 1980s, on the other hand, the abundance of small copepods, *Metridia* spp., has been high during 1980s. The coincidence of the climate regime shift and the timing shift of peak season of copepod production was observed. The most variations match climate regime-shift, and there may be a knock-on effect such as climate change affecting physical oceanography which affects biological production and subsequently species composition (Fig.8.3). We found some long term increase trend of biomass some cold water group of copepod species. It is consistent with that the cooling trend has been observed in the mid latitude (35-45°N) of western North Pacific (Levitus *et al.* 2005). Therefore, this trend may be an effect of earth warming condition. Duration of the peak season of copepod production was relatively short during mid 1970s and late 1980s because of cold winter and hot summer. On the other hands, water temperature was low after early 1990s and preferable season for biological production (mild spring to early summer season) was long (Fig.8.4). The long term variation of the effect of intrusion of the oligotrophic Okhotsk Sea water into the Oyashio sea area induced in 18.6 year tidal cycle caused by the oscillation of the axis of the earth was thought to be a part of the reason of the low abundance of *Neocalanus*. This low nutrient trend may be caused by dominant Okhotsk water in the mesopelagic layer. The low nutrient concentration during 1980s in Oyashio region may affect the low production of *Neocalanus* spp. (Fig.8.5). Another reason of low abundance of *Neocalanus* during 1980s is thought to be the top-down control of predation by abundant pelagic fish, because the Pacific sardine had been quite abundant in the western North Pacific during mid 1980s (Fig.8.6).

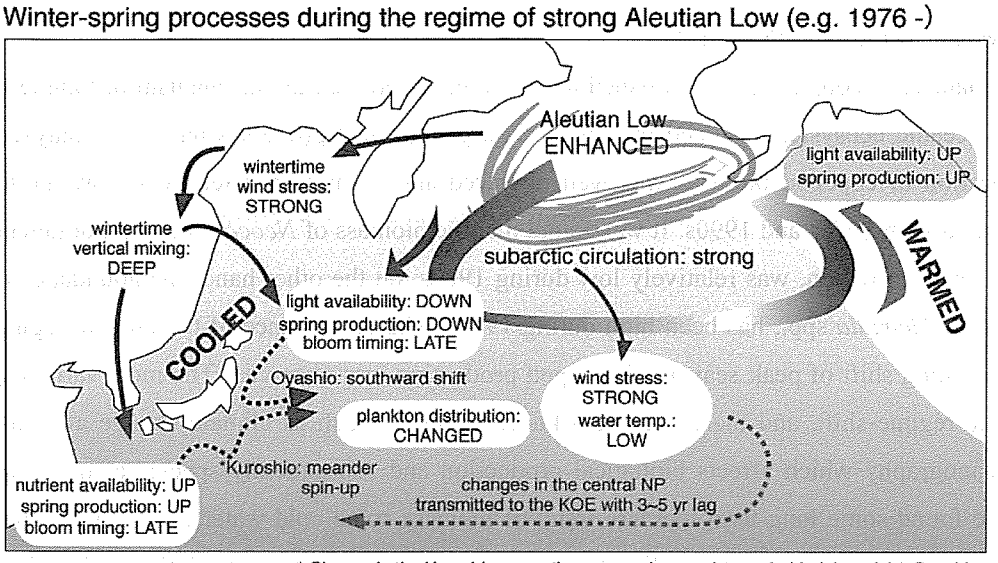

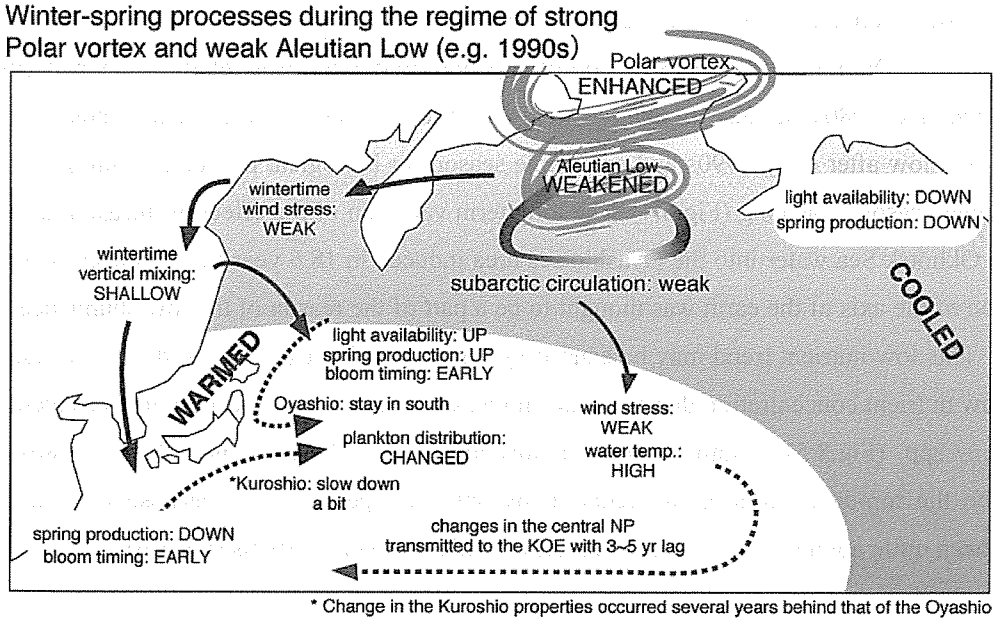

Figure 8.3 Schematic figures of the mechanisms of long-term variation of zooplankton community in relation to climate change. (Summery report of research results under GERF (Global Environment Research Fund) in FY2005 edited by Global environment bureau, Ministry of the environment of Japanese government)

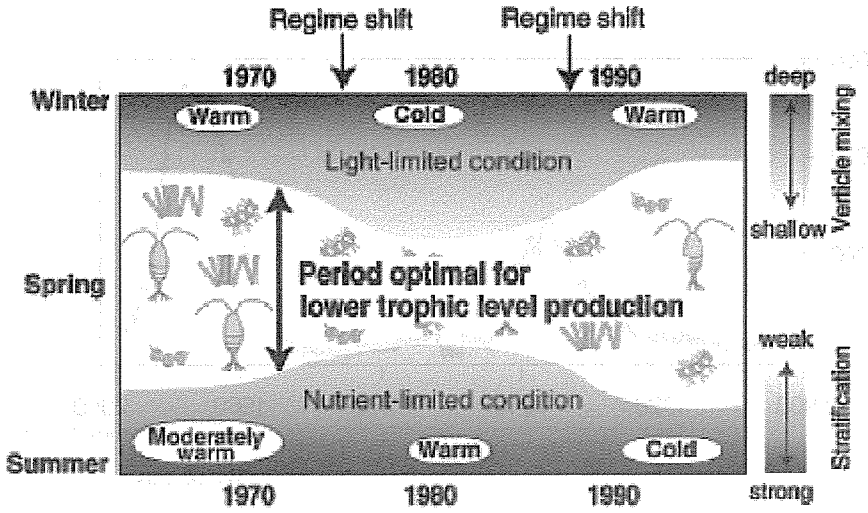

Figure 8.4 Phenological hypothesis on low abundance of zooplankton during 1980s.

(Chiba *et al.* 2006)

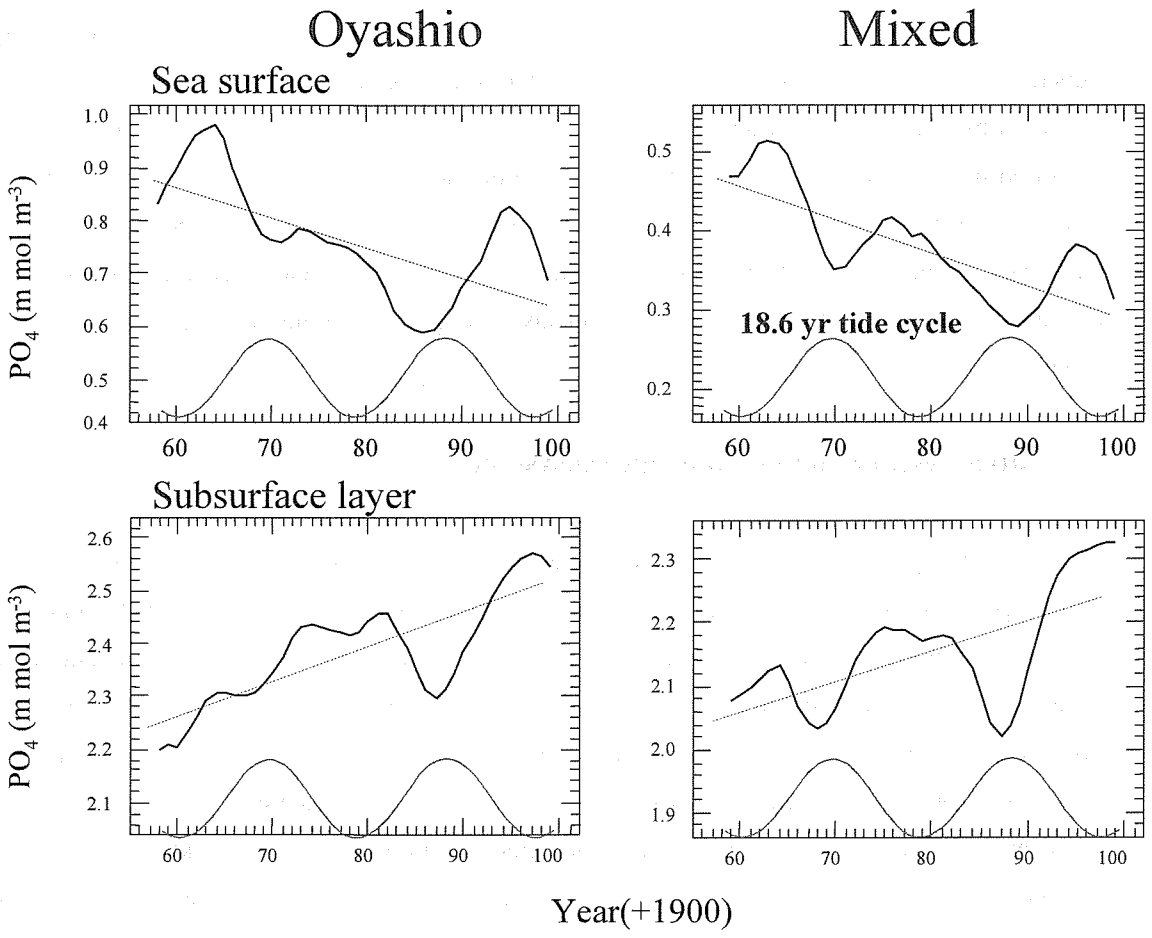

Figure 8.5 Long-term variation of nutrient (PO_4) concentrations and 18.6 year tidal cycle induced by oscillation of earth's axis.

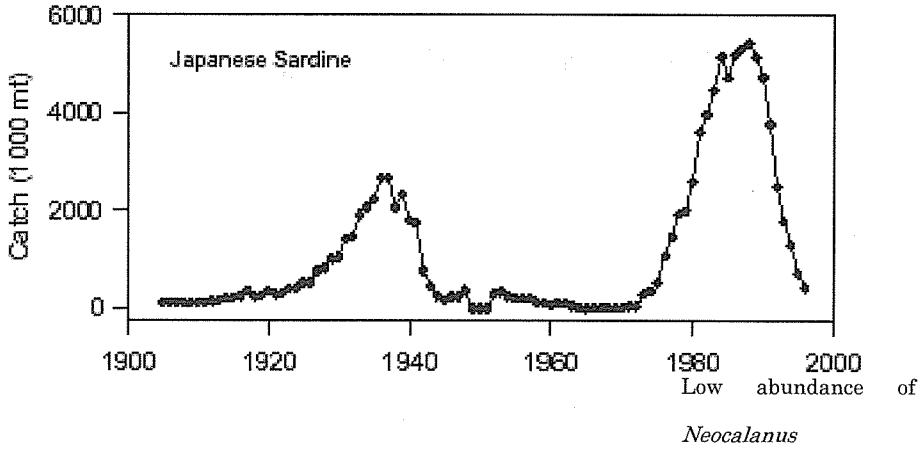

Figure 8.6 Long-term variation of landing weight of Japanese sardine.

In order to assess the effect of vertical transport of carbon by the seasonal vertical migration of dominant zooplankton species especially *Neocalanus* spp., the information of vertical migration (*e.g.* range of depth, seasonal timing of descend and seasonal variation of feeding activity to the primary production) of various copepod species was researched. It is revealed that 4.3g Carbon $m^{-2}year^{-1}$ was transported by the seasonal vertical migration of *Neocalanus* spp. And 0.81g Carbon $m^{-2}year^{-1}$ was transported by *Eucalanus bungii*. In the subarctic North Pacific, 0.12Gt of carbon were transported annually to deepwater from the surface by the seasonal vertical migration of copepods species in total. Based on the data set of this project, biomass of *Neocalanus* species varied highly, therefore the estimation of vertical transportation by zooplankton migration should be varied highly, 1.2-8.0 Gt $year^{-1}$.

8.4 Frontier research on mesopelagic ecosystem

Since the sunlight does not reach to deep water, there is no photosynthesis in mesopelagic and bathypelagic ecosystems (deeper than ca.200m depth). Although such a no primary production area, various and abundant animals are living in mesopelagic layers. Micronekton is the dominant group of mesopelagic animals. Micronekton is not a taxonomical category but a category of living type. They are including both vertebrates and invertebrates, larger than usual zooplankton size (ca.20mm-ca.200mm). Though their swimming abilities are weak compared to usual nekton, they can swim and escape from plankton net collection. Representative micronekton animals are myctophid fish (lantern fish) some species of squids or shrimps living in deep pelagic layers. Although their biomass thought to be high and their vertical and horizontal distributions are wide, their ecological information has been quite restricted, because most of micronekton is not important

species for fisheries. Since the vertical transportation of organic materials through biological processes is thought to be important for analysis of global change of ecosystem, it is necessary to analyze the ecology (e.g. life history or feeding habit) and quantitative data on distribution and biomass. In recent years, sampling gears for larval and juvenile fish are well developed, because the sampling data collected by plankton net are underestimated. Those sampling gears are suitable for collecting micronekton quantitatively. Using those gears, micronekton research have been conducting in recent years. From the result of these researches, their vertical distributions are classified into following patterns (Watanabe *et al*, 1999).

1) Diurnal migrant

They perform diurnal migration clearly. They ascent to shallow layers during night, and they sink and stay in deep layers during daytime. Some species ascent to surface or subsurface layers (shallower than 100m depth) where primary production exist, while other species ascent but not reach to euphotic zone (200m depth). In the North Pacific, *Diaphus theta* and *Caratoscoperus warmingii* are representative species of diurnal migrants to euphotic zone, and *Lampanictus jordani* is also representative diurnal migrant but does not reach to euphotic zone.

2) Partly diurnal migrant

The daily behaviors are flexible for each individual. Some individuals perform diurnal vertical migration and some stay in deep layer during night within same species (maybe same population). The reason of this separated behavior within same species has not been well revealed. In the North Pacific, *Stenobrachius leucopsarus* is representative species of partly diurnal migrants.

3) Mesopelagic residence

They do not perform clear diurnal vertical migration and stay in deep layer even in night time. In the North Pacific, *Stenobrachius nannochir* and *Protomyctophum thompsoni* are representative species of mesopelagic residences.

The vertical migrant usually consume their prey in shallow layer during night. It means that their feeding area is highly productive zone compared to deeper layer where they stay during daytime. Since they excrete or are consumed by higher trophic animals in deep layer during daytime, their vertical migration plays a role to transport organic production in shallow layer to deep layer. This ecological function is called "biological pump". Biological pump is though to have an effect to drawdown carbon to deep layer. Therefore, not only zooplankton but also micronekton may have an important role for biochemical cycle process in the ocean. Although mesopelagic residence does not drawdown organic matters by itself behavior, they often consume ontogenetic migrant, *Neocalanus* copepods. Consumption of ontogenetic migrant by mesopelagic migrant implies the role of vertical

migration of zooplankton for ecosystem of deep layers as biological pump.

In recent years, Fisheries Research Agency of Japan have conducted routine sampling cruises once a season throughout a year, and micronekton were quantitatively collected at fixed stations of western North Pacific during both day and nigh by newly developped midwater trawl net systems, *e.g.* 4m^2 MOCNESS (Wiebe 1985), MOHT (Oozeki *et al.*, 2004). Vertical and horizontal distribution of dominant species of micronekton and their feeding habits have been precisely analyzed. From the results of series of this analysis, food-web structure of mesopelagic ecosystem in the western North Pacific (Fig.8.7). This food-web map will be useful information on vertical transportation of carbon by biological processes in the deep ocean.

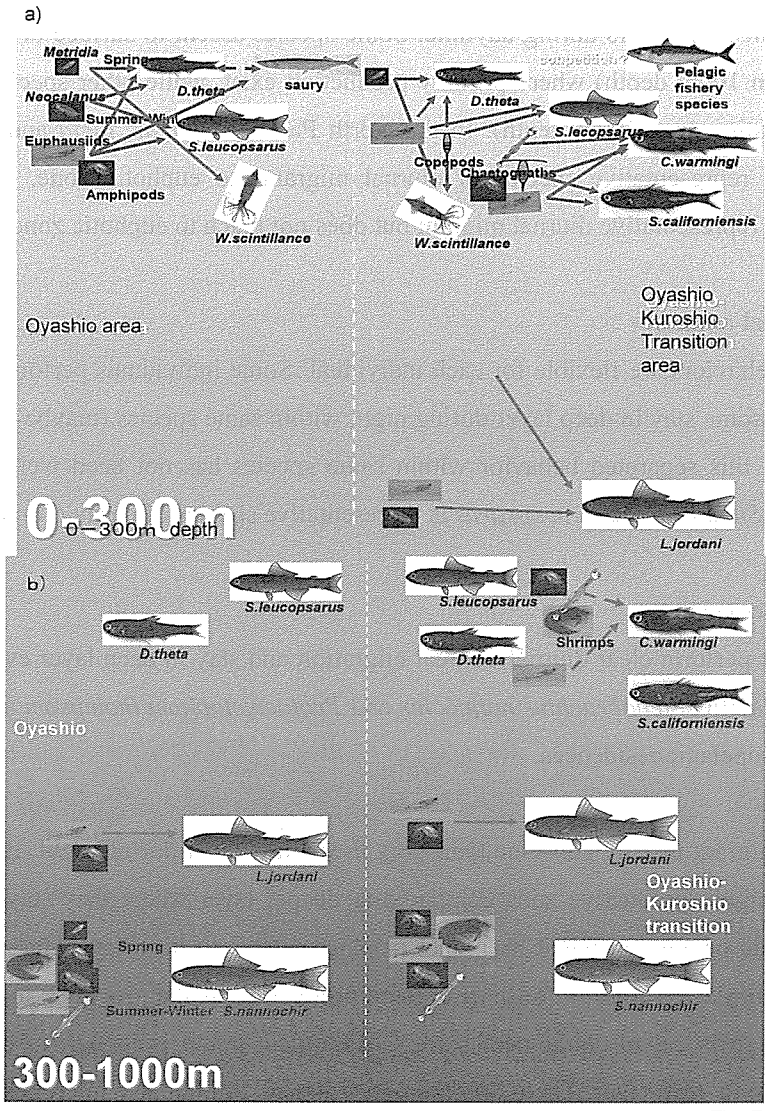

Fig. 7

Figure 8.7 Food web structures of micronekton communities in Oyashio cold water region (left) and Oyashio-Kuoshio transition region (right) in 0-300m depth layer (a) and 300-1000m depth layer (b).

8.5 Conclusions

- Many species of oceanic zooplankton and micronekton perform vertical migration.
- Ontogenetic (seasonal) vertical migration of some species (e.g. *Neocalanus* copepods) may play a role of draw down the organic carbon in shallow layer to deep layer (more than 1000m depth).
- Diurnal vertical migration may also play some role to transport organic carbon vertically.
- Long term variation of zooplankton communities has been observed and it may cause the flexibilities of draw down effects of carbon by biological processes.
- In order to research on the mechanisms of long term variations of ecosystem and climate change, long term field monitoring activities are necessary.
- There are some hypotheses on the mechanism of ecosystem variation, phonological process, top down control, bottom up control.
- In the mesopelagic layer micronekton and zooplankton have high biomass even though there is no primary production.
- In recent years, mesopelagic ecosystem research has been explored, because new research gears are developed.
- Micronekton may play an important role for carbon transportation to deep layer because they widely distribute vertically over the world ocean.

The quantitative data of transportation of carbon in mesopelagic layer is not enough, but it has been accumulating now. The function and long-term variation of carbon cycle by biological process in the ocean will be well advanced near future.

References

Chiba S., Tadokoro, K., Sugisaki, H., and Saino, T. (2006) Influence of the North Pacific decadal oscillation on plankton phenology in the western subarctic North Pacific based on the 50 yr zooplankton data set, the Odate Collection, Global Change Biology

Edwards, M. and Richardson, A. J. (2004) Impact of climate change on marine pelagic phenology and trophic mismatch. Nature 430, 881-884

Harrison P.J., Whitney, F.A., Tsuda, A., Saito, H., and Tadokoro, K. (2004) Nutrient and Plankton Dynamics in the NE and NW Gyres of the Subarctic Pacific Ocean. *Journal of Oceanography*, 60, 93-117

Levitus,S., Antonov, J. and Boyer, T. (2005) Warming of the world ocean 1955-2003. Geophysical Research Lettres

Odate,K. Zooplankton biomas and its long-term variation in the western north Pacific Oceam, Tohoku sea area, Japan Bull. Tohoku. Natl. Fish. Res. Inst. (1994)

Oozeki,Y., Hu,F., Kubota, H. Sugisaki, H., and Kimura, R. (2004) Newly designed quantative frame trawl for sampling larval and juvenile pelagic fish. Fisheries Science 70,223-232

Richardson, A.J. and Schoeman, D.S. (2004) Climate impact on plankton ecosystems in the

Northeast Atlantic. Science 305, 1609-1612

Roemich, D. and McGowan, J. (1995) Climatic warming and the decline of zooplankton in the California Current. Science 267, 1324-1326

Watanabe, H., Moku, M., Kawaguchi, K., Ishimaru, K., and Ohno, A.(1999) Diel vertical migration of myctophid fishes (family Myctophidae) in the transitional waters of the western North Pacific. Fisheries Oceanography 8, issue2, 115-127,

Wiebe, P.H., Morton, A.W., Bradley, A.M., Craddock, J.E., Barber, V., Cowles, T.J., Flierl, G.R. (1985) Newly developments in the MOCNESS, an apparatus for sampling zooplankton and micronekton. Mar. Biol. 87, 313-323

Chapter 9

Role of Coastal Sea in Climate System

Tetsuo Yanagi
Research Institute for Applied Mechanics, Kyushu University
6-1 Kasuga-kouen Kasuga, Fukuoka 816-8580, JAPAN
e-mail: tyanagi@riam.kyushu-u.ac.jp

9.1 Decrease of tidal current amplitude in Tokyo Bay

The shallow sea area along the coast of Tokyo Bay has been reclaimed in recent years due to the rapid urbanization and industrialization as shown in Fig.9.1.

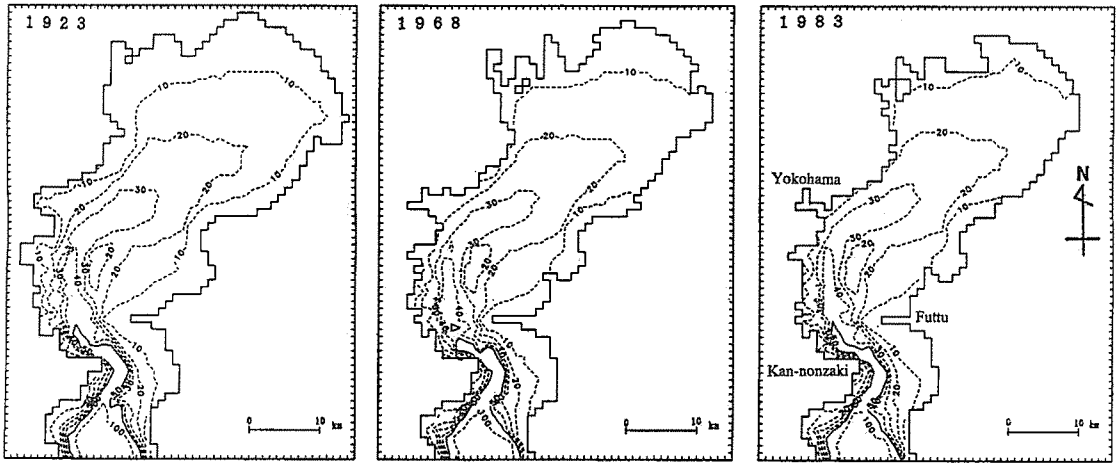

Figure 9.1 Geometry and bottom topography of Tokyo Bay in 1923, 1968 and 1983. Horizontal mesh size is 1 km x 1 km. Numbers show the depth in meters.

The changes of sea surface area, area with the depths shallower than 5 m, volume, bay length and mean depth of Tokyo Bay from 1923 to 1983 are shown in Fig.9.2. When we normalize their values in 1923 as 100 %, the sea surface area reduced to 75 %, the area with depths shallower than 5 m 19%, the volume 92 %, the bay length 93 %, but the mean depth increased to 124 % in 1983.

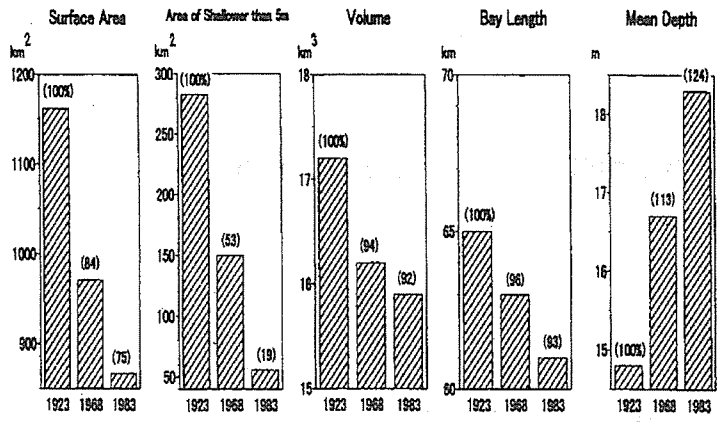

Figure 9.2 Changes of sea surface area, area with depths shallower than 5 m, volume, bay length, and mean depth of Tokyo Bay from 1923 to 1983.

The changes in tide and tidal current by such changes of geometry and topography of Tokyo Bay were investigated by using the three-dimensional numerical model developed by Guo and Yanagi (1994). The momentum equation is linear, the horizontal mesh size is 1 km x 1 km and it is devised into 10 layers vertically by the sigma coordinate. Time step is 45 s, the Coriolis parameter 8.47 x 10^{-5} s^{-1}, the horizontal viscosity 10^5 cm^2 s^{-1} and the vertical eddy viscosity is 50 cm^2 s^{-1}.

Only the M_2 tide, which is the most dominant constituent in Tokyo Bay, was calculated. The boundary conditions of amplitude and phase along the open boundary are fixed from 1923 to 1983 with 36-38 cm and 147.5°, respectively. The calculated changes in co-range and co-tidal charts from 1923 to 1983 are shown in Fig.9.3. The amplitude decreased and the phase progressed in the inner part of Tokyo Bay though they did not change in the outer part.

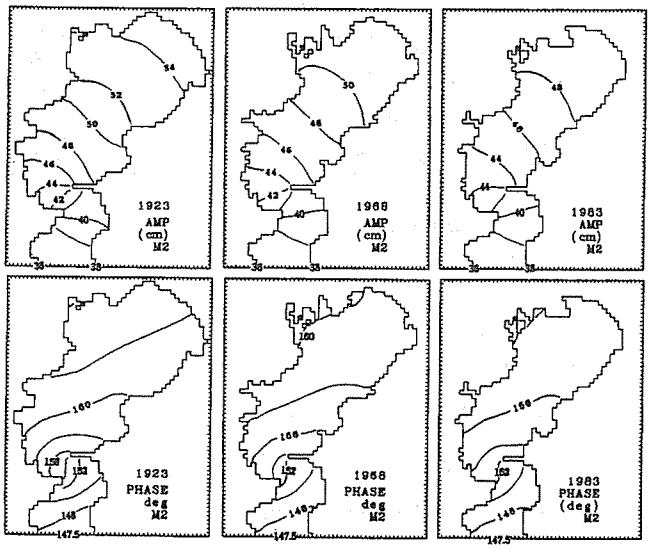

Figure 9.3 Calculated co-range and co-tidal charts of M_2 tide fro Tokyo Bay in 1923, 1968 and 1983. Phase is referred to 135 °E.

The comparisons between observed and calculated amplitude and phase of M_2 tide at Tokyo Harbor (its position is shown by a circle in Fig.9.3) are shown in Fig.9.4. As for the amplitude, their values in 1968 and 1983 agree well though those in 1923 differ a little.

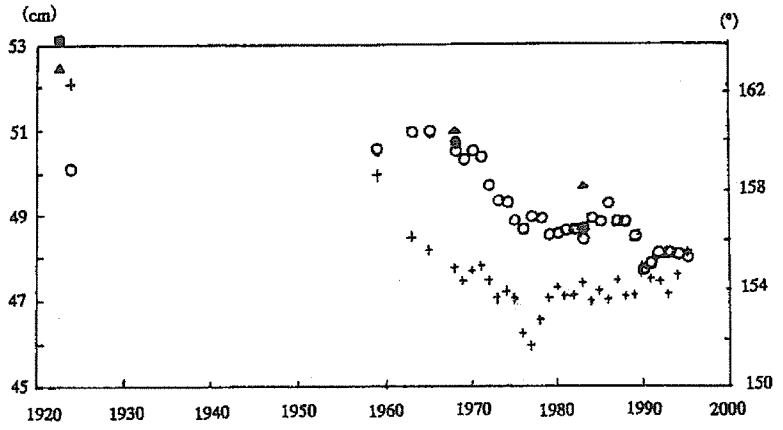

Figure 9.4 Year-to-year variations in observed tidal amplitude (open circle) and phase (plus) of M_2 tide (after Unoki and Konishi, 1998) and those in calculated amplitude (closed circle) and phase (closed triangle).

The changes in the average amplitude in the inner part of Tokyo Bay and the volume transport across the bay mouth in half tidal cycle (tidal prism) are shown in Fig.9.5. The averaged tidal amplitude decreased to 92 % and the tidal prism 65 % from 1923 to 1983. The decrease of tidal prism (65 %) is explained by the multiplication of the decrease of tidal amplitude (92 %) and the decrease of sea surface area (75 %) shown in Fig.9.2.

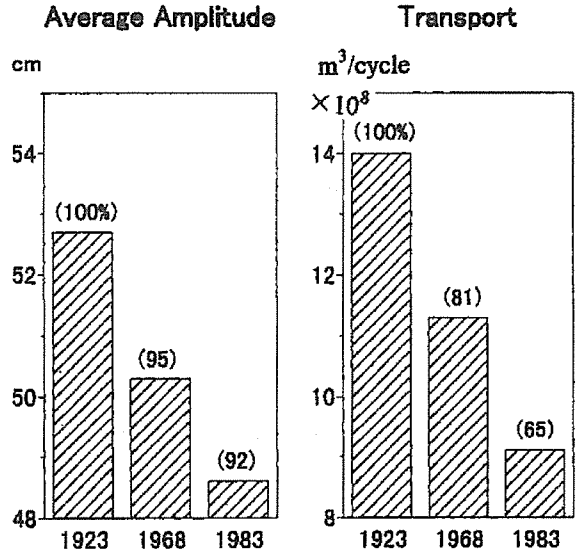

Figure 9.5 Changes of average amplitude of M_2 tide and water exchange volume by M_2 tidal current across the bay mouth in Tokyo Bay from 1923 to 1983.

The change in calculated M_2 tidal current amplitude in the surface layer from 1923 to 1983 is shown in Fig.9.6. The area with larger amplitude than 20 cm s^{-1} in the northern part of the bay mouth has shrank and tidal current amplitude decreased by 10-20 cm s^{-1} near the bay mouth from 1923 to 1983.

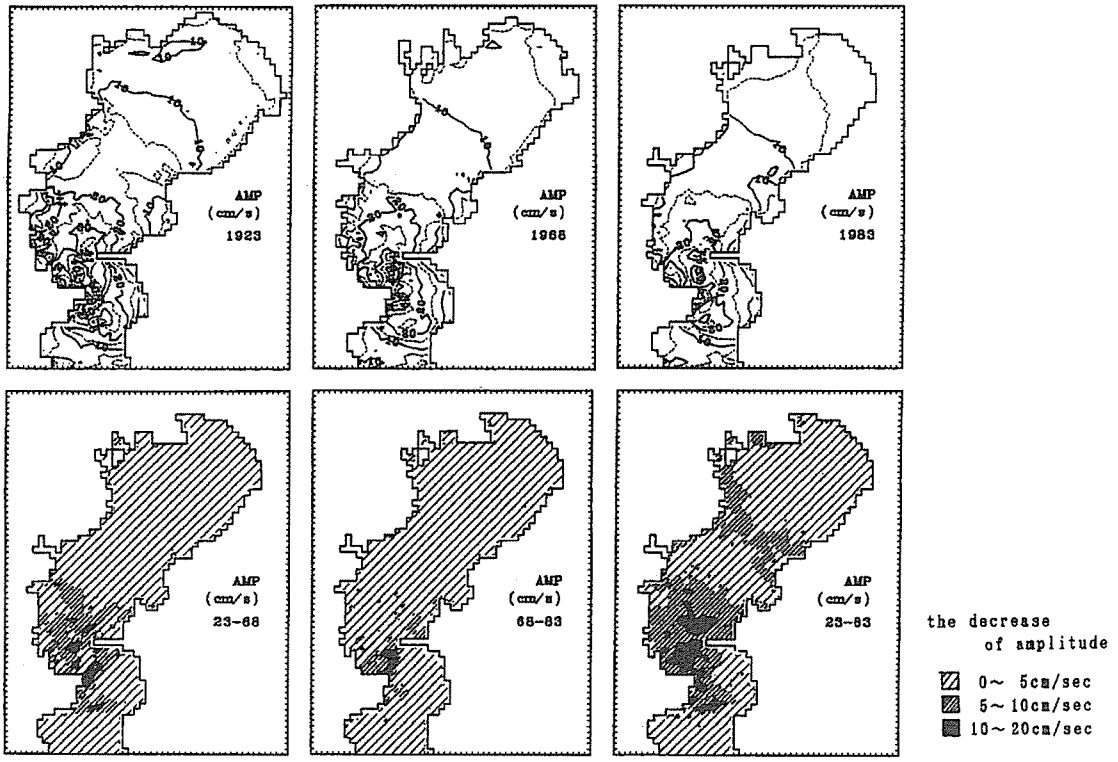

Figure 9.6 M_2 tidal current amplitude in Tokyo Bay in 1923, 1968 and 1983 (upper) and the difference of M_2 tidal current amplitude between 1923 and 1968 (lower left), 1968 and 1983 (lower center) and 1923 and 1983 (lower right).

The vertical distribution of M_2 tidal current ellipse at the northern part of the bay mouth (water depth of 8 m and the position is shown in the right panel of Fig.9.7) in 1923 is shown in the left panel of Fig.9.7. It amplitude decreased from 15 cm s^{-1} 1 m below the sea surface to 6 cm s^{-1} 1 m above the bottom. The amplitude of 6 cm s^{-1} in 1923 has decreased to 2 cm s^{-1} in 1983 from the right panel of Fig.9.7. The bottom sediment around this region was sand in 1965-1972 but it changed to be mud in 1988 (Saito and Kayane, 1991). Such change of bottom sediment was induced by the decrease of tidal current amplitude there as shown in Fig.9.7.

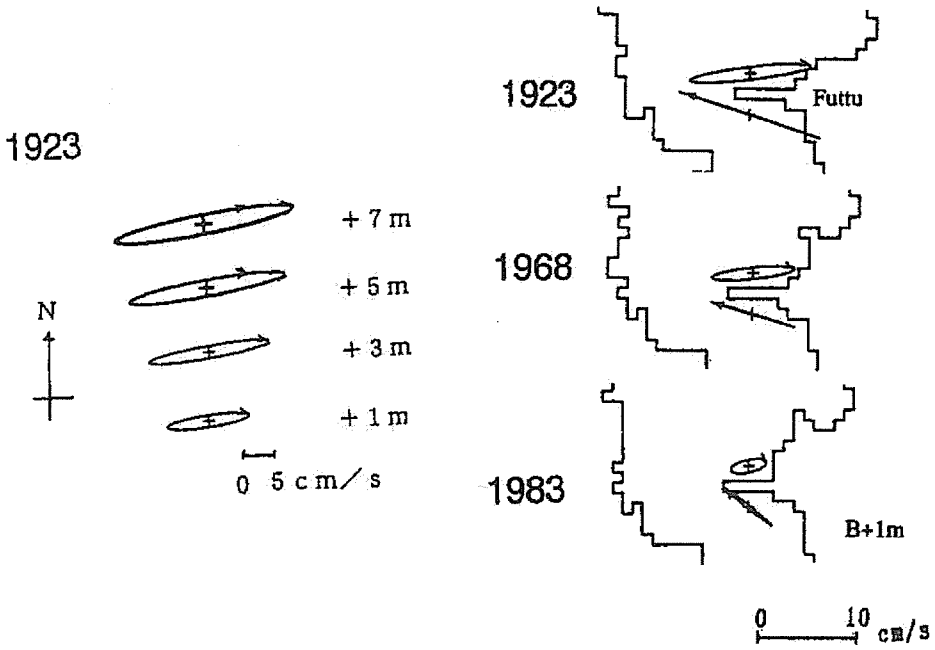

Figure 9.7 Vertical distribution of M_2 tidal current ellipses at the station with the depth of 8 m north of Futtu point (left). M_2 tidal current ellipses 1 m above the sea bottom near Futtu Point in Tokyo Bay in 1923, 1968, and 1983 (right).

The natural oscillation period of the bay (T_n) is calculated by the following equation.

$$T_n = 4\,L / (gh)^{1/2},$$

where L denotes the bay length, g gravitational acceleration (9.8 m s^{-2}) and h the mean depth. T_n of Tokyo Bay was 6.0 hours in 1923 and 5.1 hours in 1983. T_n in 1983 is more far from the M_2 tidal period of 12.4 hours than that in 1923 and it resulted in the decrease of tidal amplitude in Tokyo Bay.

The reason of decreasing tide and tidal current from 1923 to 1983 is due to the increase of natural oscillation period by decreasing bay length and increasing mean depth because of the large scale of reclamation.

9.2 Increase of density-driven current in Tokyo Bay due to the increase of water use in Metro Tokyo

Edo River is the largest among the rivers which empty Tokyo Bay (Fig.9.8) and its river discharge has increased in recent years as shown in Fig.9.9 due to the increase of water use by the increasing population in Metro Tokyo (Fig.9.9)

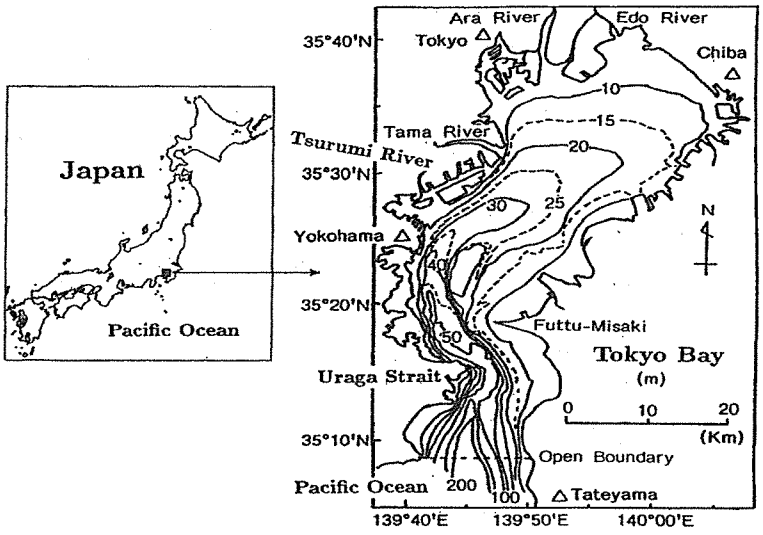

Figure 9.8 Topography and rivers in Tokyo Bay. Numbers show the depth in meters and Δ's denote the wind observation stations.

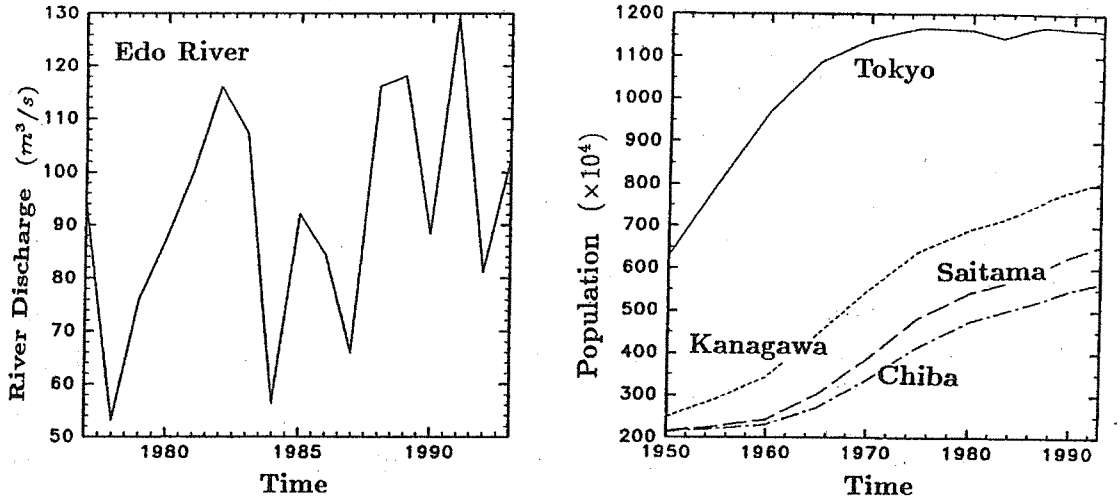

Figure 9.9 The annual variation of the river discharge of Edo River and the annual variation of the population around Tokyo Bay

The change in density-driven current by the increase of river discharge was examined by three-dimensional prognostic numerical model. The residual flow in August, when the density-driven current is most developed, in 1979 (small river discharge) and in 1989 (large river discharge) were calculated. The wind and solar radiation conditions in both years were nearly the same as shown in Fig.9.10. Tidal stress based on the tidal current in 1979 was given in 1979 and 1989.

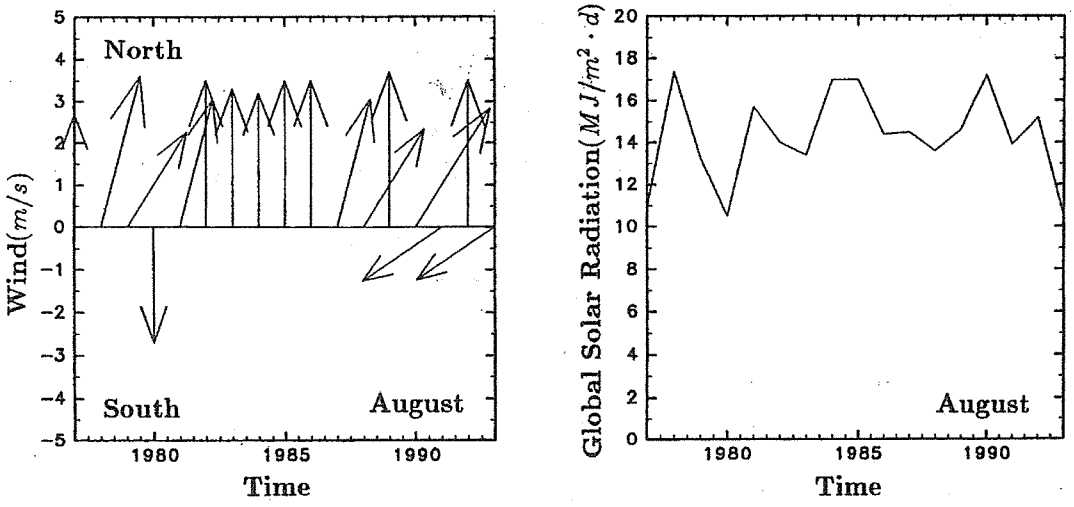

Figure 9.10 The annual variation of monthly means of the wind and the solar radiation at Tokyo.

Calculated water temperature, salinity and density in the surface and bottom layers in 1979 (Case79) are shown in Fig.9.11 and observed ones in the summer of 1979 in Fig.9.12. The comparison of observed and calculated water temperatures, salinity and density at the observed points are shown in Fig.9.13. The agreement is good from Fig.9.13.

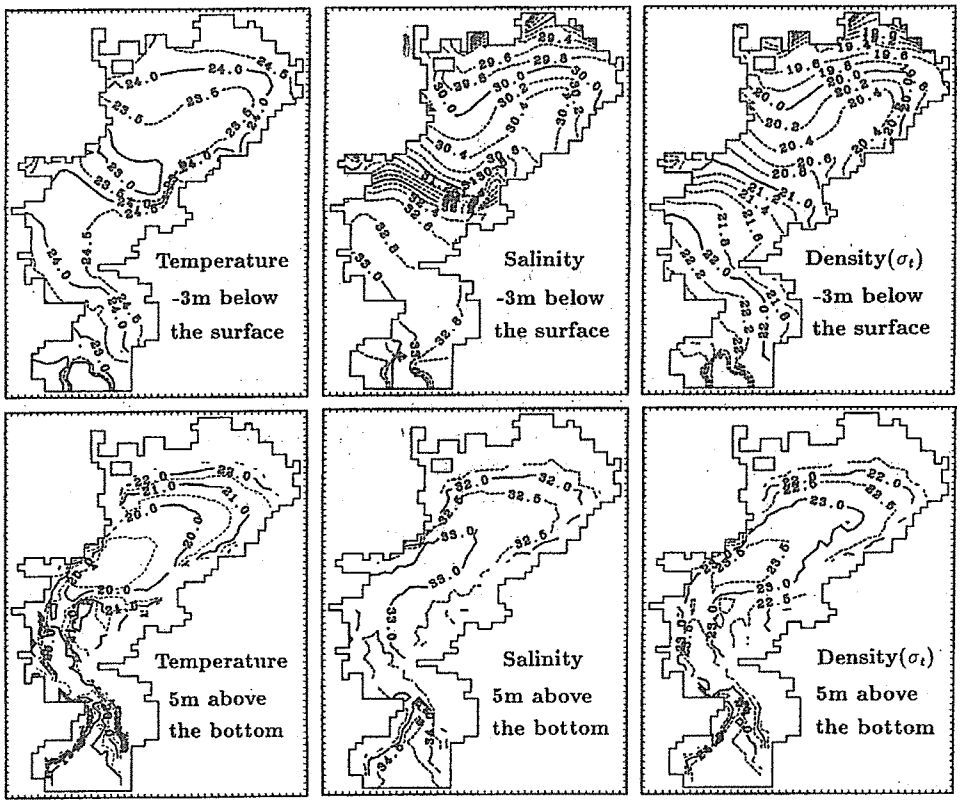

Figure 9.11 Calculated water temperature, salinity and density in CASE79.

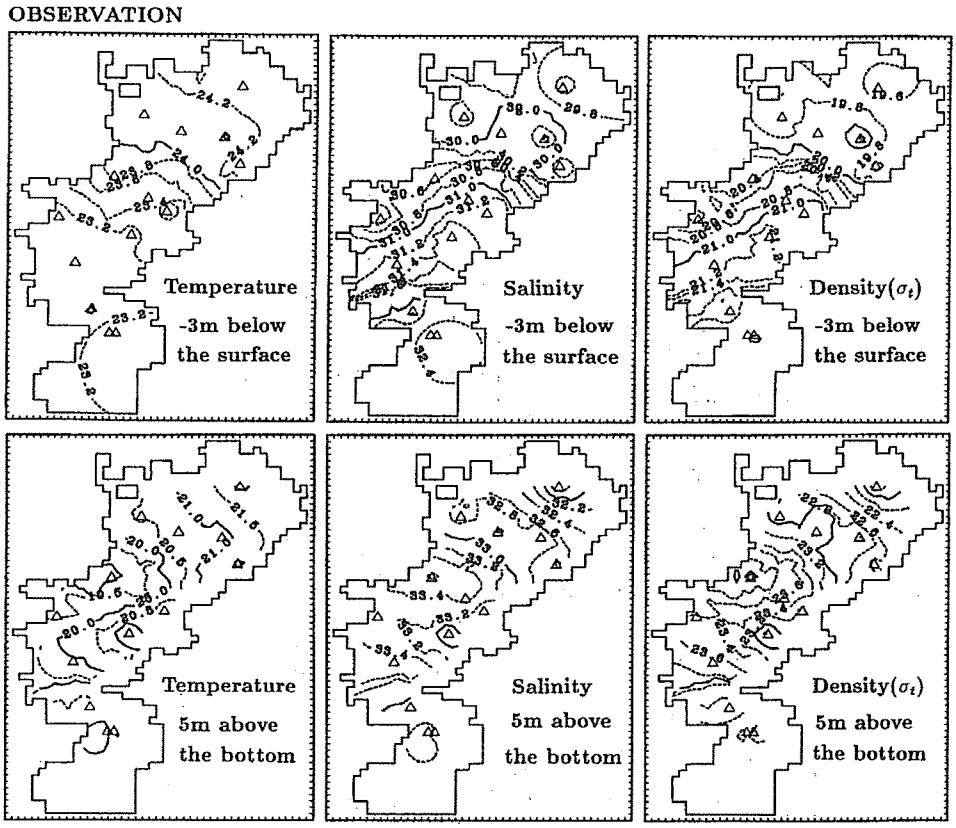

Figure 9.12 Observed water temperature, salinity and density in the summer of 1979. The triangles show the observed points.

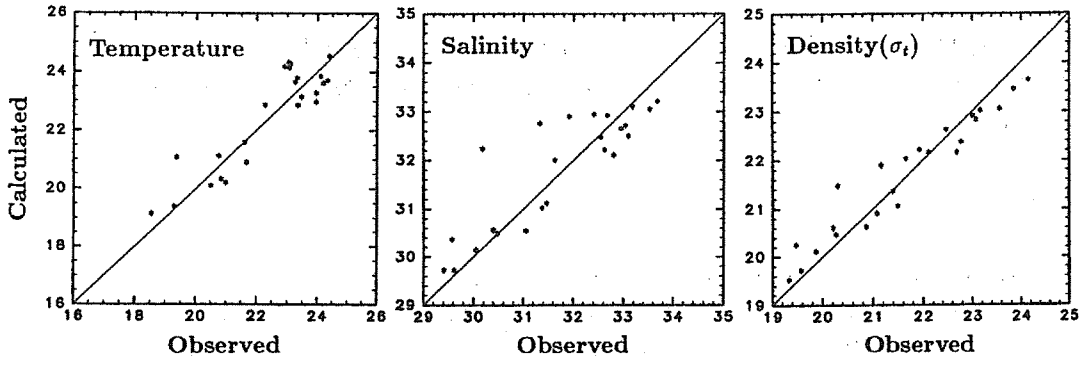

Figure 9.13 Comparison of observed and calculated water temperature, salinity and density at the observed points.

Calculated and observed residual currents are shown in Fig.9.14. In the upper layer, the calculated results show two eddies existing in the head region and the central part of the bay, which are also suggested by the observed current measurements. In the lower layer, the calculated results coincide well with the observed pattern.

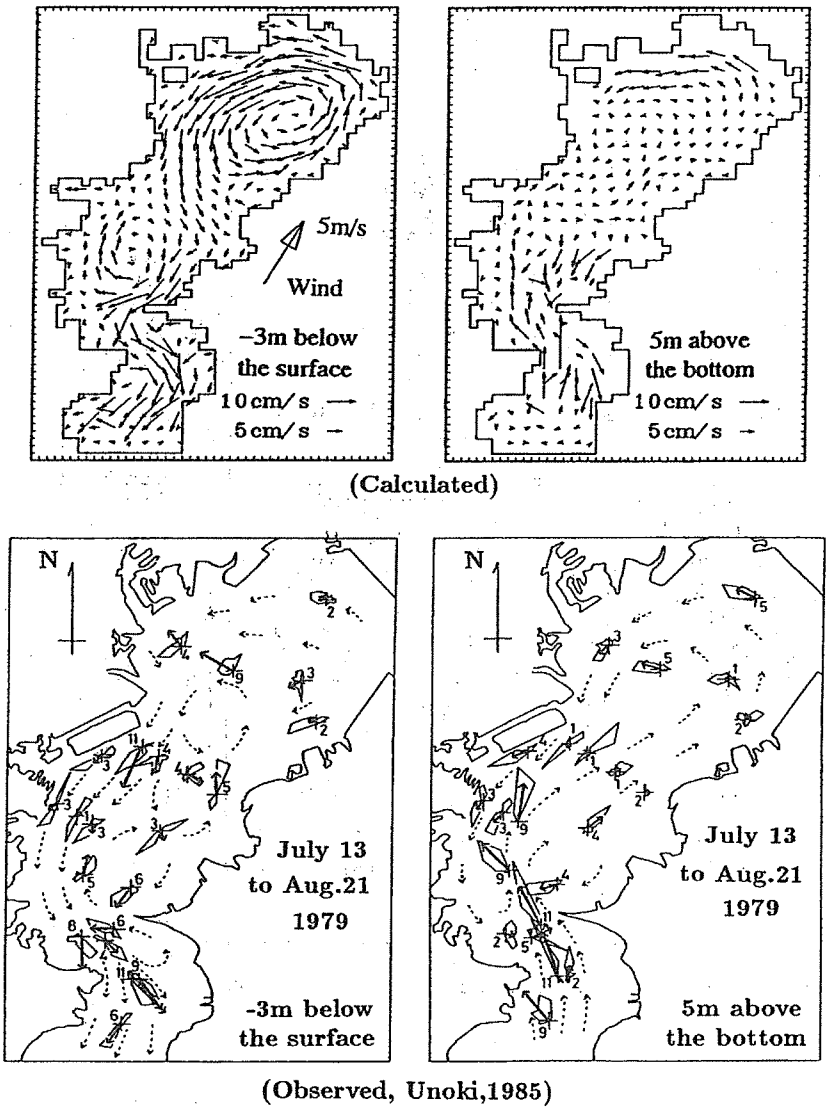

Figure 9.14 Calculated and observed residual currents in the summer of 1979. The dotted lines in the observed results are the estimated flow pattern and the numbers show the speed of the flow in cm s^{-1}.

For a deeper insight into the three-dimensional structure of the residual current in Tokyo Bay, the distribution of the residual current across four sections are shown in Fig.9.15. At the mouth of the bay (section 1), a gravitational circulation of about 5 cm s^{-1}, with maximum speeds of 10 cm s^{-1} develops. In the central part of the bay (section 2), the clockwise circulation can be found at all depths. In the head region of the bay (sections 3 and 4), the anti-clockwise circulation exists throughout the water column.

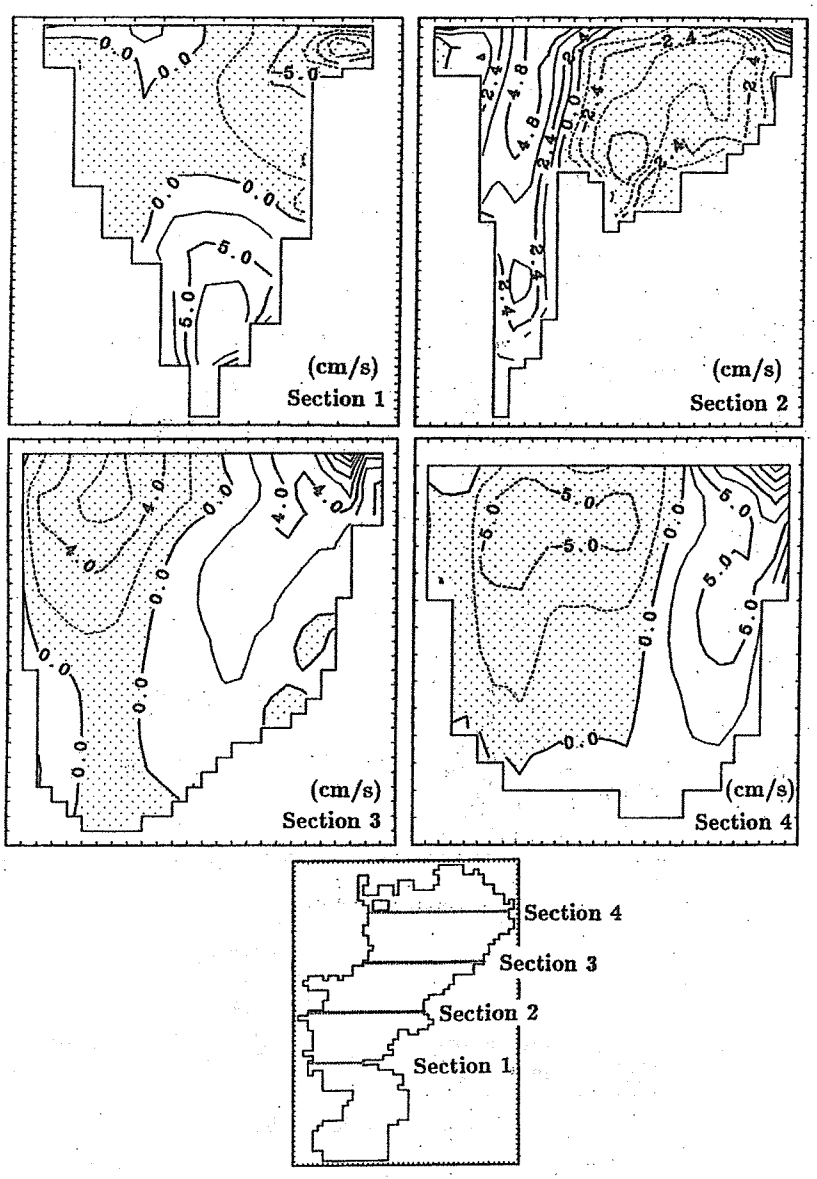

Figure 9.15 Distribution of the residual current through four sections. Positive values show northward currents and negative values southward currents.

Next we used the numerical model to calculate the currents in the summer of 1989 (CASE89). The only changes are that the river discharges are increased to the level of the summer of 1989. The calculated water temperature, salinity and density distributions are shown in Fig.9.16.

As expected, the water temperature varied little from the 1979 case but the salinity in the head region of the bay decreased greatly. Because this decrease does not change the basic pattern of salinity distribution, the calculated residual current is very similar to that calculated for 1979.

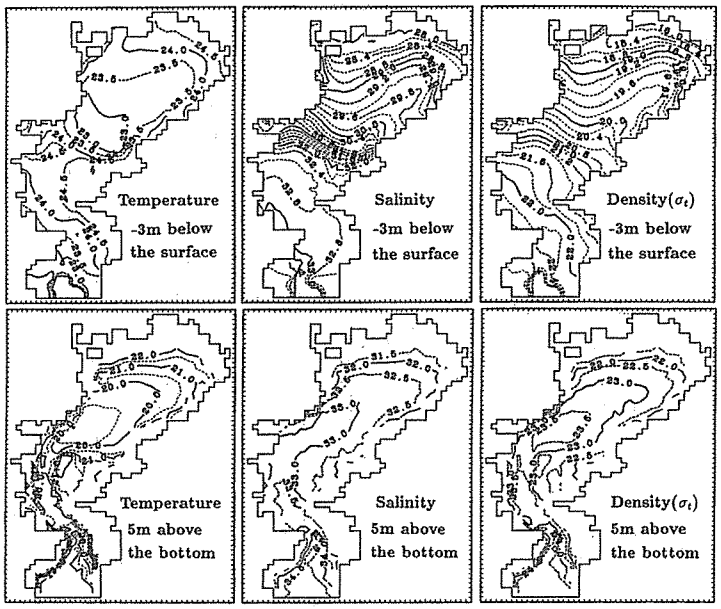

Figure 9.16 Calculated water temperature, salinity and esnity in CASE89.

Figure 9.17 shows the difference between the residual currents for CASE79 and CASE89 (CASE89 – CASE79) at three depths. The influence of the increase in fresh water discharge on the residual current is strongest in the head region of the bay where the anti-clockwise circulation seems to be decreased.

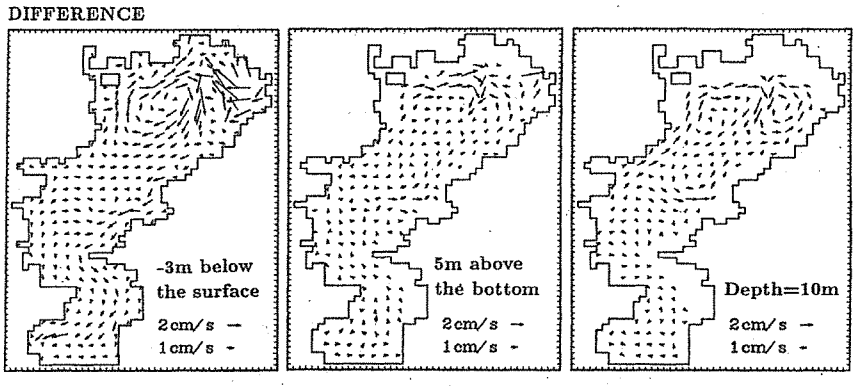

Figure 9.17 Difference of the residual current between CASE79 and CASE89.

The differences between the residual currents for the two cases are shown across four sections in Fig.9.18. It is interesting that the form of the residual current difference is very different in each section. In the head region, the residual current difference form two eddies from the sea surface to the bottom. But at the mouth of the bay, the residual current difference forms a gravitational circulation. Our calculations show that the gravitational circulation at the mouth of the bay is enhanced by up to 0.5 cm s^{-1} by the increase of the fresh water discharge as shown in Fig.9.18.

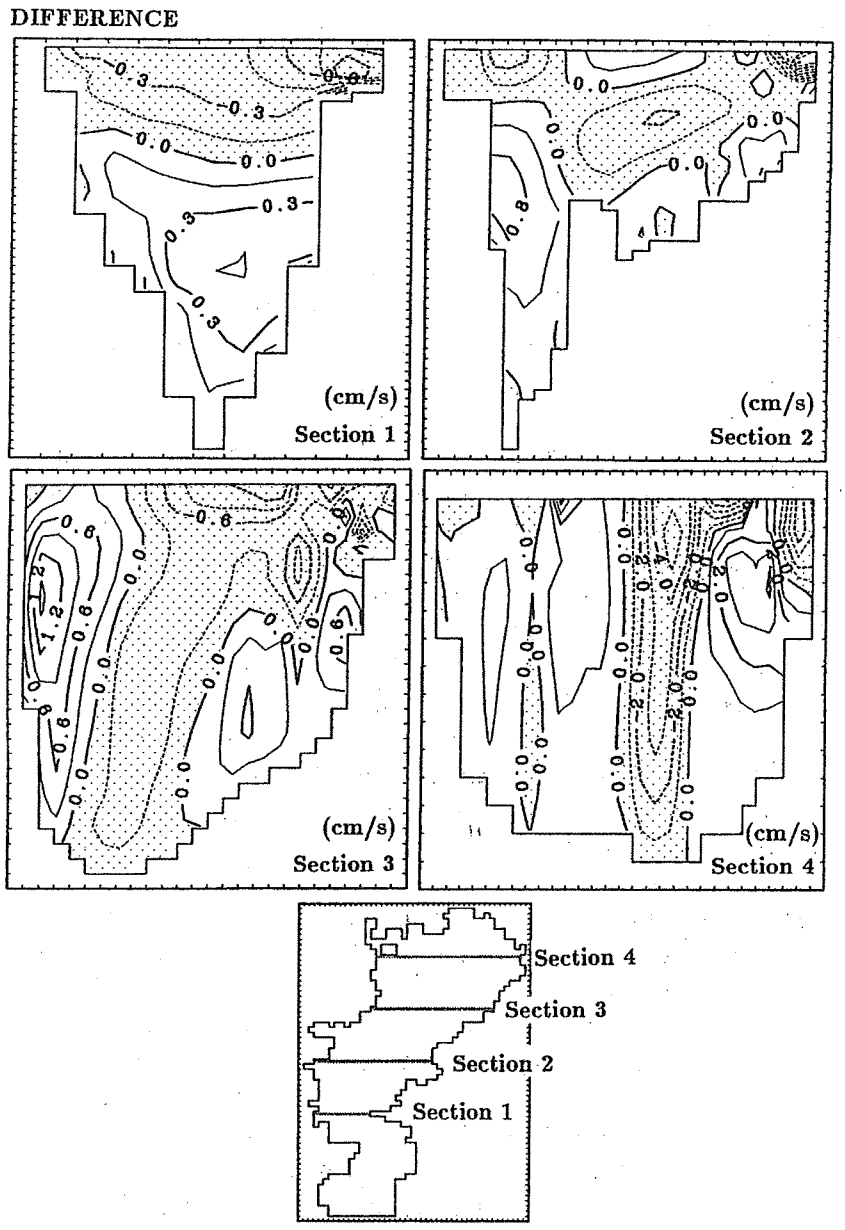

Figure 9.18 Differences of the residual current between CASE79 and CASE89 through four sections. Positive values show northward currents and negative values southward currents.

9.3 Increase of estuarine circulation due to the decrease of tidal amplitude

The estuarine circulation is intensified by the decrease of tidal amplitude because the vertical eddy viscosity is decreased as shown in Fig.9.19.

The estuarine circulation in Tokyo Bay has been intensified in recent years due to 1) the decrease of tidal amplitude and 2) the increase of water use on land and resulting increase of river discharge.

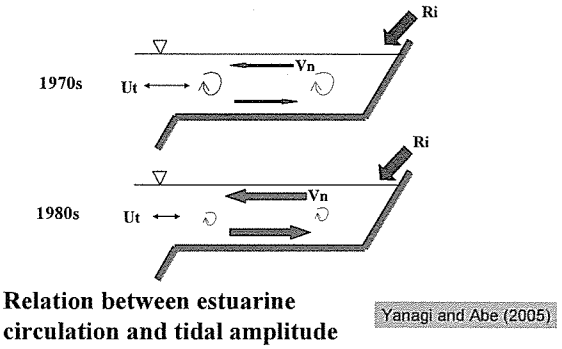

Figure 9.19 Estuarine circulation and tidal current amplitude.

9. 4 Decrease of summer SST and increase of winter SST in Tokyo Bay

The long term trends of water temperature in Tokyo Bay were analyzed using the monitoring data, which have been measured by the related local goverments every month since 1970s (Fig.9.20). The sea water temperature in Tokyo Bay shows descending trends in summer and rising trends in winter (Fig.9.21). These trends are more obvious in the area receiving greater water intrusions from the open ocean. Comparing to the in-bay water, the outer water is cooler in summer and warmer in winter.

Therefore, the amount of ocean water entering from the Pacific Ocean must have been increasing during the last 22 years, thereby resulting in such trends of water temperature in Tokyo Bay.

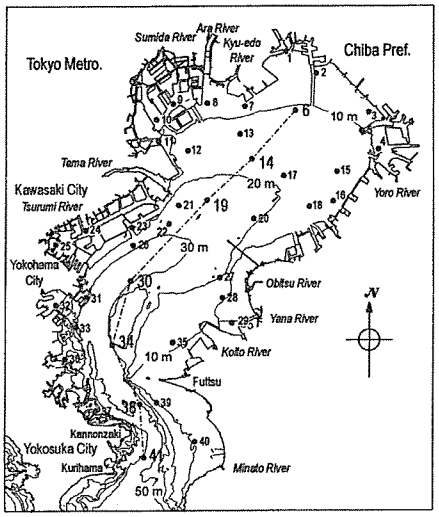

Figure 9.20 Stations for water quality monitoring in Tokyo Bay.

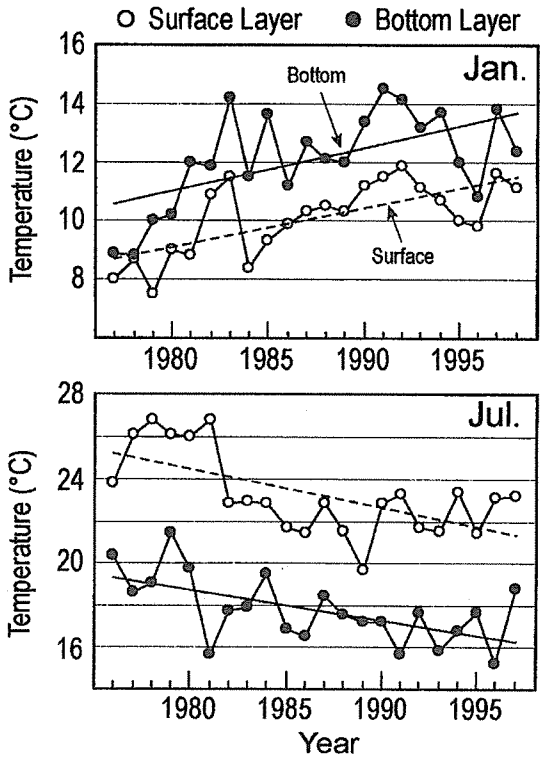

Figure 9.21 Trends of water temperature in January and July at Sta.21 of Tokyo Bay.

References

Ando,H., N.Kashiwagi, K.Ninomiya, H.Ogura and M.Yamazaki (2003) Long term trends of seawater temperature in Tokyo Bay. Oceanography in Japan, 12, 407-414.

Guo,X. and T.Yanagi (1994) Three-dimensional structure of tidal current in Tokyo Bay, Japan. La mer, 32, 173-185.

Guo,X. and T.Yanagi (1998) Variation of residual current in Tokyo Bay due to increase of fresh water discharge. Continental Shelf Research. 18, 677-694.

Saito,Y. and H.Kayane (1991) Change of bottom sediment around Futtu Point in Tokyo Bay. Scientific Journal of Sediment in Japan, 34, 135-138 (in Japanese).

Unoki,S. and T.Konishi (1998) Decrease of tide and tidal current and its sequences to material transport. Oceanography in Japan, 7, 1-9 (in Japanese with English abstract and captions).

Yanagi,T. and K.Onishi (1999) Change of tide, tidal current and sediment due to reclamation in Tokyo Bay. Oceanography in Japan, 8, 411-415 (in Japanese with English abstract and captions).

Yanagi,T. and R.Abe (2005) Increase in water exchange ratio due to decrease in tidal amplitude in Ariake Bay, Japan. Continental Shelf Research.

Chapter 10

Analysis of Satellite Ocean Color Data

Kosei Sasaoka
Frontier Research Center for Global Change,
Japan Agency for Marine-Earth Science and Technology (FRCGC/JAMSTEC)
3173-25 Showa-machi, Knazawa-ku, Yokohama, Kanagawa 236-0001, JAPAN
E-mail: sasaoka@jamstec.go.jp

10.1 Introduction

Satellite remote sensing can be an extraordinarily effective and powerful tool in biogeochemical study for global change, fisheries oceanography research, fisheries management, marine protected species research and management and so on. Biogeochemical processes in the ocean play an important role in environmental changes and climate changes by natural events but also human activities as well. These processes, including carbon cycles, are mainly contributed by primary production as a key parameter. Also primary productivity is a very important factor for controlling the distribution, abundance and availability of marine fish populations. Primary productivity in the sea accounts for ~30 percent of the total global annual production (Falkowski, 1980). The sea contains a substantial amount of carbon compared to that present in the atmosphere or in terrestrial organisms (Valiela, 1995). Measurement of the variability of the distribution of chlorophyll *a* (chl-*a*) and primary productivity in the ocean is a way of monitoring oceanic biogeochemical cycles and marine fishery resources.

Satellite oceanography has been quite advanced in last two decades (Robinson, 2004 and Martin, 2004). Especially, ocean color remote sensing is a useful new tool for continuously monitoring the temporal and spatial variability of chl-*a* concentration and primary productivity. Remote sensing of ocean color from space began in 1978 with the successful launch of NASA's Coastal Zone Color Scanner (CZCS). Despite the fact that CZCS was an experimental mission intended to last only one year, the sensor continued to generate a valuable time-series of data over selected test sites until early 1986. Ten years passed before other sources of ocean-color data became available with the launch of Ocean Color and Temperature Scanner (OCTS) in 1996 and Sea-viewing Wide Field-of-view Sensor (SeaWiFS) in 1997. Moderate Resolution Imaging Spectroradiometer

(MODIS) have recently been launched by NASA and we can obtain MODIS data near real-time from web site now (http://oceancolor.gsfc.nasa.gov/). Still more are planned for the near future by various space agencies. Current, historical and scheduled ocean color sensors are described on the IOCCG's (International Ocean Color Coordinating Group) web site (http://www.ioccg.org/sensors_ioccg.html) in detail.

To understand the basic ocean color image analysis, we will demonstrate how to display the satellite data using SeaDAS software on Linux PCs. In this practice we use three kinds of satellite data including chl-*a* (MODIS and SeaWiFS) and sea surface temperature (SST) (AVHRR). Satellite data we used for this practice was shown in Table10.1. These satellite data are HDF (Hierarchical Data Format), which is a bit complex format. SeaDAS is free software and very powerful tool, since it enables us to read HDF data and display standard ocean color data easily.

Table 10.1 List of satellite data we used for this practice

Sensor	Satellite	Product	Temporal/Spatial Resolution	Data period	Parameter
MODIS	Aqua	Level 3 SMI (Standard Mapped Image)	Monthly / 4km	July, 2002 - Current	Chl-*a*[*1]
MODIS	Aqua	Level 3 SMI	Monthly / 4km	July, 2002 - Current	SST[*2]
MODIS	Aqua	Level 3 LAC (Local Area Coverage)	Daily / 1km	1 December, 2006	Chl-*a*[*3]
SeaWiFS	Orbview-2	Level 3 SMI	Monthly / 9km	September, 1997 - Current	Chl-*a*[*4]
AVHRR	NOAA	Level 3 Pathfinder Best SST data	Monthly / 9km	January, 1985 - May, 2003	SST[*5]

Download site:

*1. Ocean Color Web (http://oceancolor.gsfc.nasa.gov/) Level 3 Browser,

*2. Ocean Color Web (http://oceancolor.gsfc.nasa.gov/) Level 3 Browser,

*3. Ocean Color Web (http://oceancolor.gsfc.nasa.gov/) Level 1 and 2 Browser,

*4. Ocean Color Web (http://oceancolor.gsfc.nasa.gov/) Level 3 Browser,

*5. NASA JPL, PO.DAAC (http://podaac.jpl.nasa.gov/sst/), AVHRR Pathfinder products,

10. 2 How to display ocean color data using SeaDAS

SeaDAS (SeaWiFS Data Analysis System) is a comprehensive image analysis package for the processing, display, analysis, and quality control of ocean color data. We can obtain program source for SeaDAS package from NASA's SeaDAS web site (http://oceancolor.gsfc.nasa.gov/seadas/). Latest version (SeaDAS 5.0) is currently available for PC Linux (Red Hat), Macintosh OS X, Sun Solaris, and SGI IRIX platforms. The Interactive Data Language (IDL) from Research System Inc. (RSI) is used to build all the GUI and display-related programs in SeaDAS. Purchasing an IDL license is no longer required in order to run SeaDAS. Instead, users may choose to use "runtime" SeaDAS, which makes use of an IDL embedded license that is provided with the SeaDAS package. If you'd like to know how to install SeaDAS on your PC in detail, please check SeaDAS web site described above.

10.2.1 How to display a MODIS, SeaWiFS or AVHRR product with coastlines, gridlines and color bar using SeaDAS

- Start up the 'SeaDAS main menu' on terminal window:

- Select Display
- Select a file:

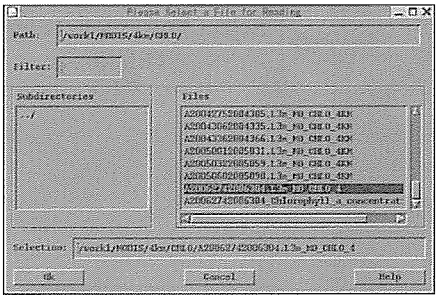

Press the Okay button to view all available products in the file.

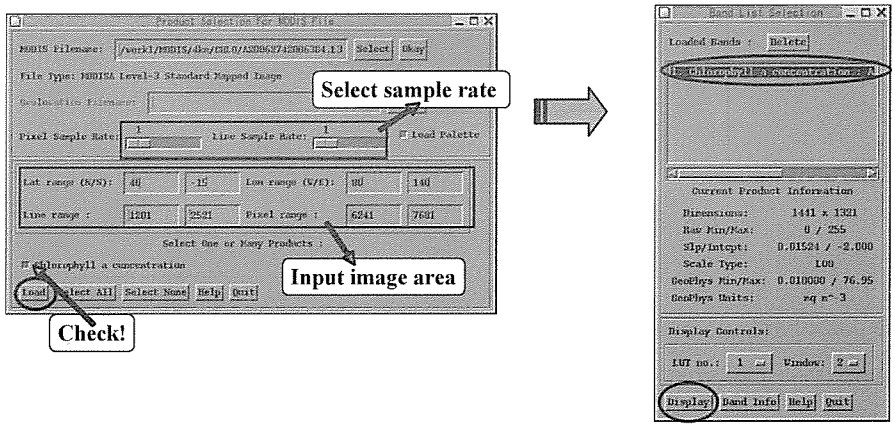

Select the product to be loaded and press the Load button. After the product loaded, you will see it is added to the Band List Widget.

- Display the satellite image:

  From the Band List Widget, select the product you would like to display.

  Select the window number for display.

  Press the Display button to display the product on the Display Window Widget.

- Display the coastlines and gridlines:

  From the Display

  Select Functions → Coastline

  Select Functions → Grid

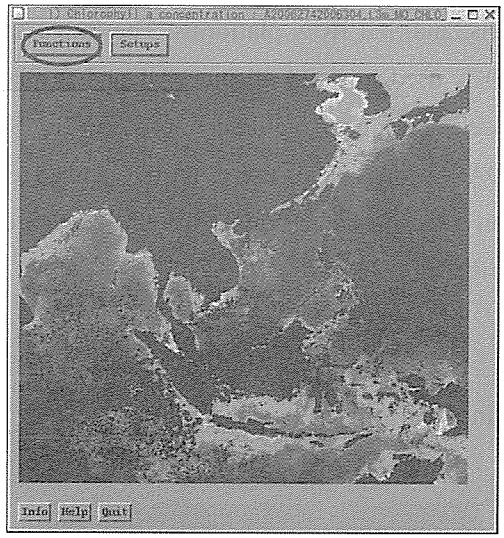

To modify the default setups for coastline and gridline functions,

Select Setups --> Coastline or Setups ---> Grid

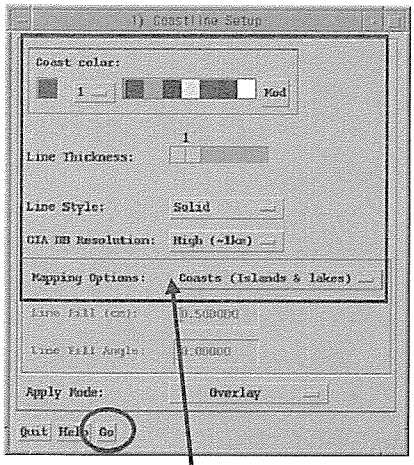

Select line type ;
Color
Thickness
Resolution

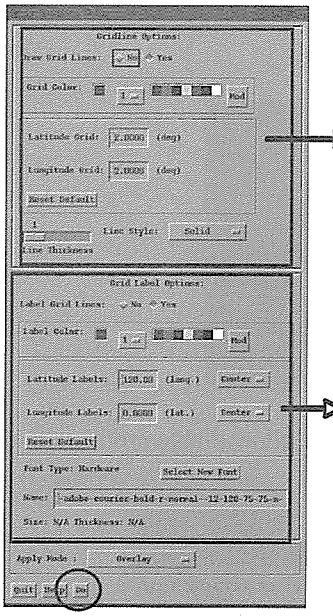

Select line color, Interval, Thickness

Select label color, position

- Display the color bar

  Select Functions --> Colorbar --> On

- How to rescale an image

  Select Functions --> Rescale

  After modifying the Scale Min/Max

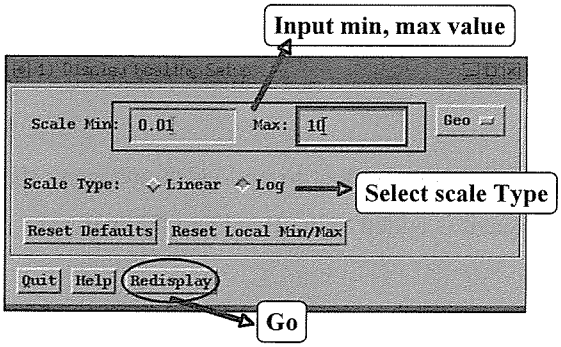

and/or the Scale Type, press Redisplay

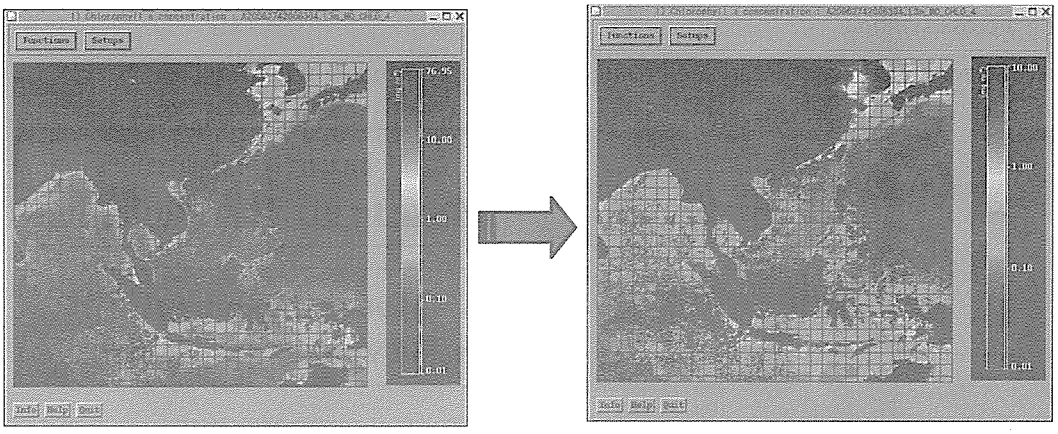

Default scale　　Scale : 0.01 - 10

10.2.2 How to save the results to a PNG or PS file

Output Display Function provides the capability of outputting PNG, Postscript or Postscript Dump image formats to an output disk file. The entire displayed window or a region may be output. A color bar may also be appended to the output image. 24 bit true color image output should select PNG 24 Bit TrueColor as output file type.

● Select Functions → Output → Display

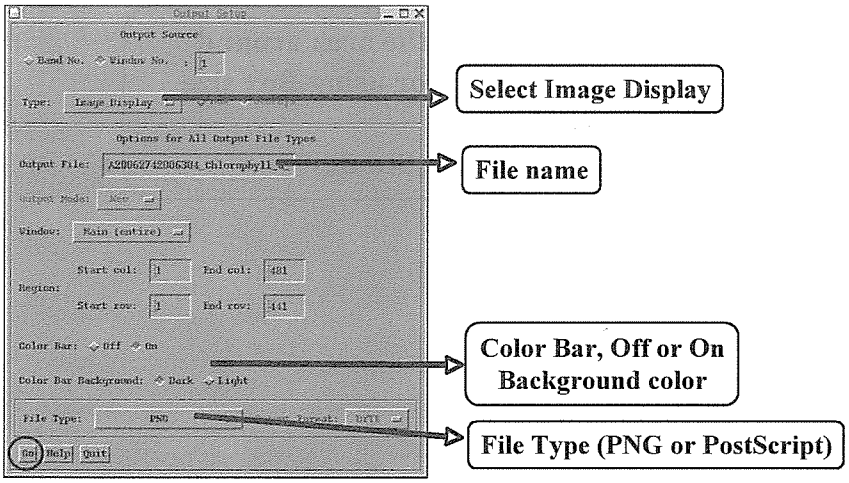

10. 3 Compare with satellite and in-situ chlorophyll a concentrations in Ise-Bay

In this chapter, we will examine the accuracy of ocean color sensor using in-situ chl-*a* data obtained from ship observation in Ise-Bay (Practice1) using SeaDAS functions. To derive chl-*a* value from ocean color satellite, we use "Read and Profile" including SeaDAS function. The Read and Profile Widget provides a bi-directional location function along with a variable-sized box-area data viewing capability. In addition, statistics are performed on the box-area selected (in terms of both raw data and geo-physical data values). This function also allows the capabilities of showing all

the bits' on/off status of the pixel data and graphically marking point locations on the graphics plane with a cross symbol.

- Select Functions → Read and Profile in the Display Window Widget

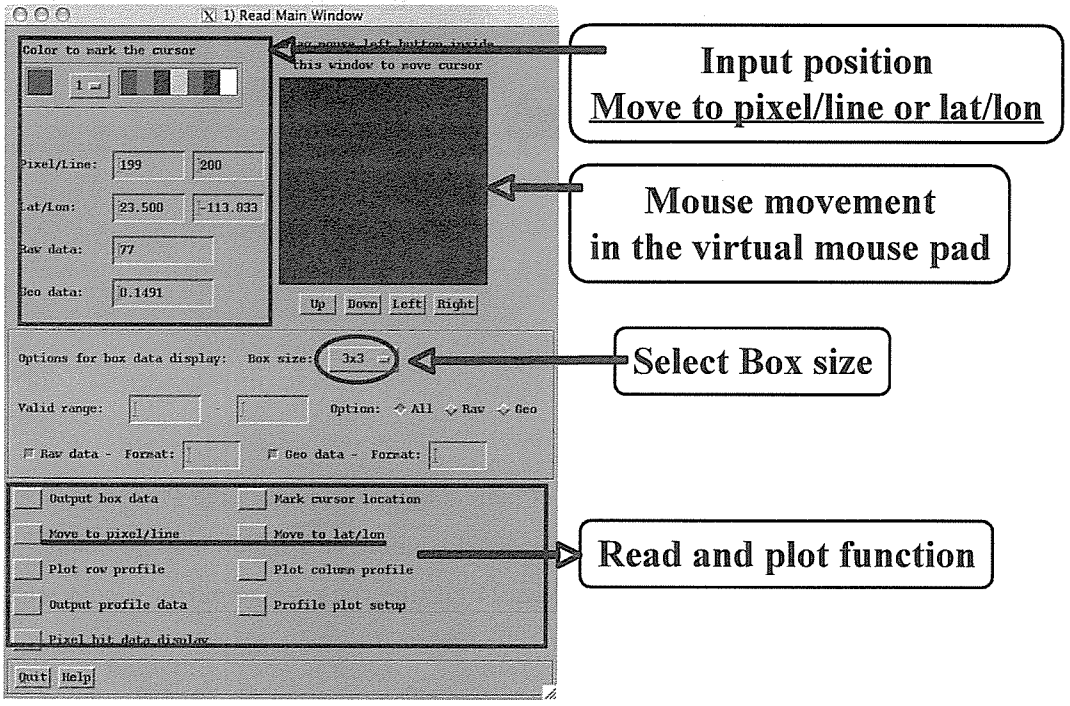

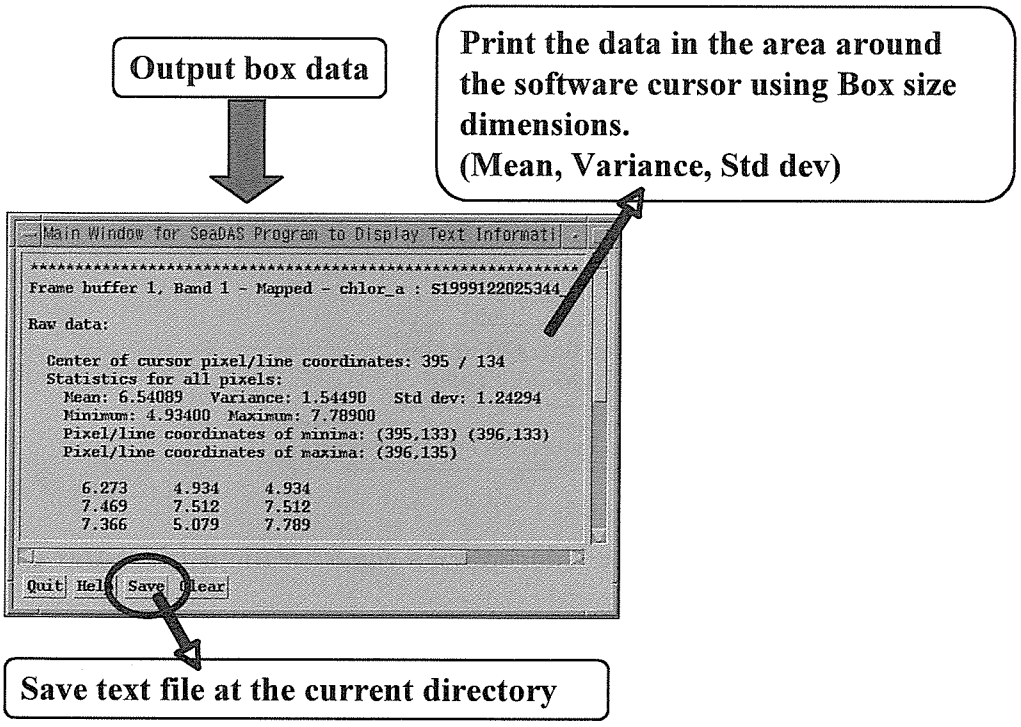

10.3.1 Ship and satellite observation in Ise-Bay on 1 December, 2006

We carried out water sampling for chl-*a* measurement by Seisui-Maru cruise on 1 December, 2006. Sampling locations were shown in Fig.10.1 and results of in-situ chl-*a* measurements were shown in

Table 10.2. Since weather condition was relatively good, we also obtained clear satellite data on the same day (Fig.10.2).

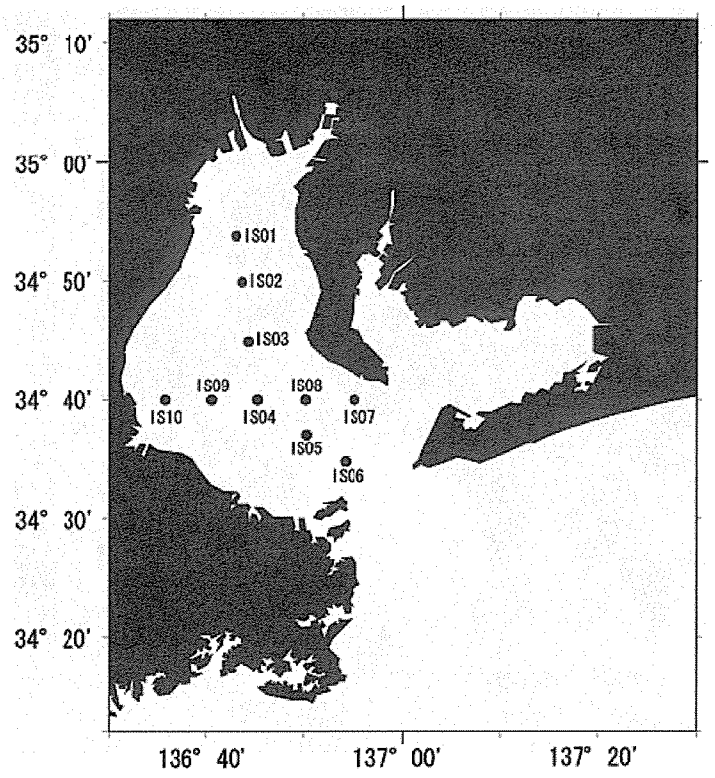

Figure 10.1 Locations of water sampling in Ise-Bay on 1 December 2006.

Table 10.2. Result of in-situ chl-*a* measurements (Depth = 0m) in Ise-Bay.

Station	Time (JST)	Lat.(N)	Long.(E)	*In-situ* Chl-*a* (mgm^{-3})
IS01	7:50-7:57	34.90	136.72	3.8
IS02	8:27-8:36	34.83	136.73	3.5
IS03	9:07-9:14	34.75	136.74	3.2
IS04	9:45-9:52	34.67	136.75	2.4
IS05	14:14-14:22	34.61	136.85	2.6
IS06	11:32-11:42	34.58	136.90	2.3
IS07	10:56-11:00	34.67	136.92	2.0
IS08	10:23-10:29	34.67	136.84	2.5
IS09	16:02-16:11	34.67	136.68	3.4
IS10	16:39-16:47	34.67	136.60	2.6

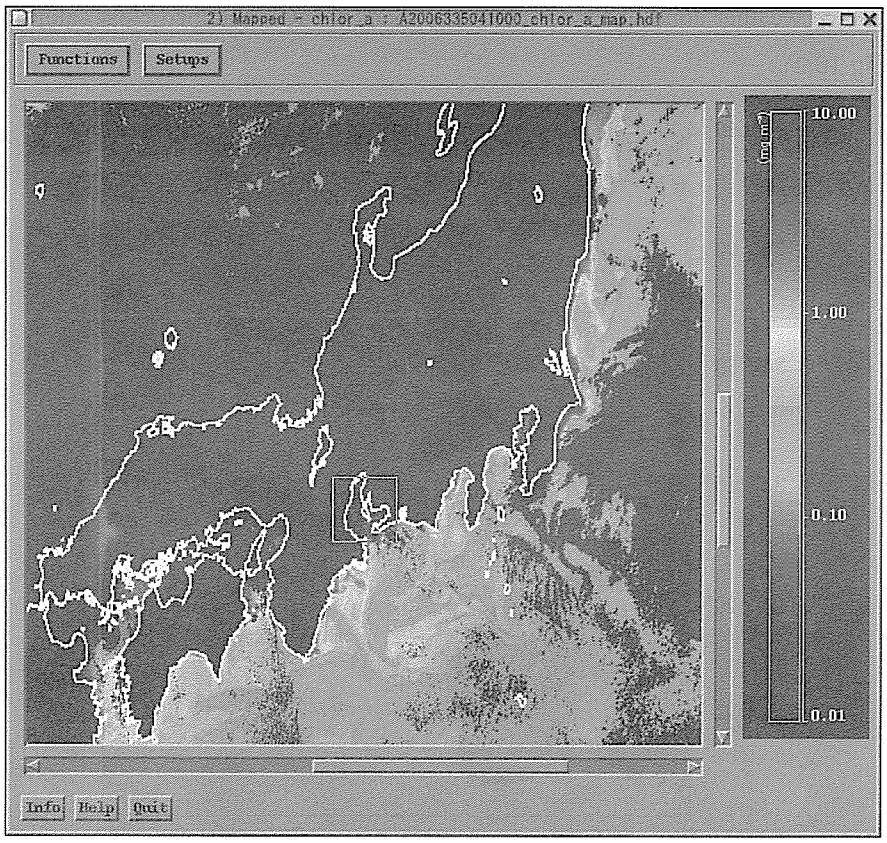

Figure 10.2 MODIS daily chl-*a* image on 1 December, 2006.Observation time = 4:10(GMT), Spatial resolution = 1km

10.3.2 Relationships between satellite chl-*a* and in-situ chl-*a*

We examined the accuracy of MODIS chl-*a* data in the Ise-Bay using "Read and Profile" function of SeaDAS. Satellite values were used mean value within 5 by 5-squared box. Figure 10.3 shows relationships between MODIS chl-*a* and in-situ chl-*a* concentrations in Ise-Bay. We understood satellite observations tend to be overestimate in Ise-Bay. Satellite chl-*a* data is being derived as a standard algorithm using the empirical relationship between the radiance ratio of blue-green bands and chl-*a* concentrations (Gordon *et al.*, 1983 and O'Reilly *et al.*, 1998). The radiance in the blue-green region is sensitive to phytoplankton absorption, and the algorithm can detect low chl-*a* concentrations from 0.01 mg m^{-3} upward. However, the radiance at the blue wavelength is closer to the lower limit of detection in the very high chlorophyll concentrations because of the strong absorption of phytoplankton pigment. This spectral region is highly affected by non-phytoplankton particles and colored dissolved organic matter (CDOM), which also strongly absorbs blue-green light. Accordingly, in highly turbid waters such as coastal regions, estimation errors become a serious factor. We suggested that large errors between satellite and in-situ observations in Ise-Bay was caused by high turbid waters including non-phytoplankton particles and CDOM due to river inflow.

Many researchers have reported there are still some problems in chl-*a* estimates for ocean color sensor especially in coastal regions (*e.g.*, Murakami *et al.*, 2006 and IOCCG, 2000). We have to be careful for using ocean color data in the coastal regions such as Ise-Bay. Now many investigators try to develop the coastal algorithms for ocean color sensor by various approaches (*e.g.*, Tanaka *et al.*, 2004, Hu *et al.*, 2005 and IOCCG, 2006).

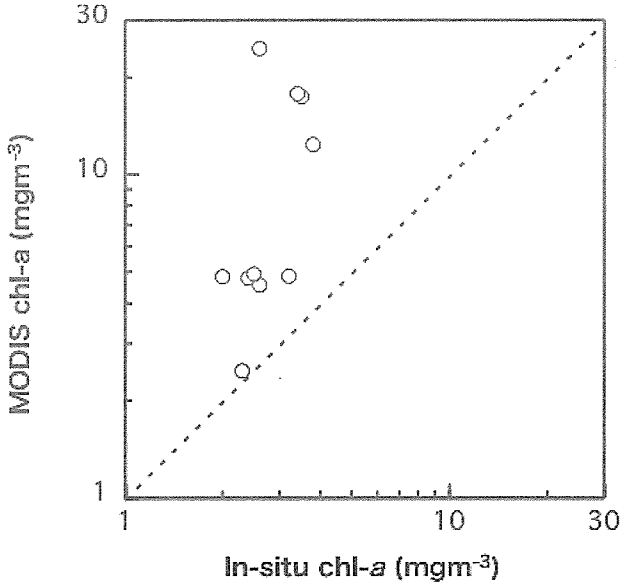

Figure 10.3 Relationships between MODIS chl-*a* and in-situ chl-*a* concentrations in Ise-Bay.

References

Falkowski, P. G. (1980): Primary productivity in the sea, P. G. Falkowski (ed.), Plenum, New York.

Gordon, H.R., D.K. Clark, J.W. Brown, O.B. Brown, R. H. Evans and W. W. Broenkow (1983): Phytoplankton pigment concentrations in the Middle Atlantic Bight: comparison of ship determinations and CZCS estimates, *Appl. Opt.*, 22, 20.

Hu C., F. E. Muller-Karger, C. Taylor, K. L. Carder, C. Kelble, E. Johns and C. A. Heil (2005): Red tide detection and tracing using MODIS fluorescence data: A regional example in SW Florida coastal waters, *Remote Sensing of Environment*, 97, 311-321.

International Ocean-Color Coordinating Group (IOCCG) (2000): Remote Sensing of Ocean Color in Coastal, and Other Optically-Complex, Waters, Sathyendranath, S. (ed.), Reports of the International Ocean-Color Coordinating Group, No. 3, IOCCG, Dartmouth, Canada.

International Ocean-Colour Coordinating Group (IOCCG) (2006): Remote Sensing of Inherent Optical Properties: Fundamentals, Tests of Algorithms, and Applications., Lee, Z.P. (ed.), Reports of the International Ocean-Colour Coordinating Group, No5, IOCCG, Dartmouth, Canada.

Martin, S. (2004): An Introduction to Ocean Remote Sensing, Cambridge University Press, Cambridge.

Murakami, H., K. Sasaoka, K. Hosoda, H. Fukushima, M. Toratani, R. Frouin, B. G., Mitchell, M. Kahru, P. Deschamps, D. Clark, S. Flora, M. Kishino, S. Saitoh, I. Asanuma, A. Tanaka, H. Sasaki, K. Yokouchi, Y. Kiyomoto, H. Saito, C. Dupouy, A. Siripong and J. Ishizaka (2006): Validation of ADEOS-2 GLI ocean-color products using in-situ observations, *J. Oceanogr.*, 62, 373-393.

O'Reilly, J. E., S. Maritorena, B. G. Mitchell, D. A. Siegel, K. L. Carder, S. A. Garver, M. Kahru, C. McClain (1998): Ocean color chlorophyll algorithms for SeaWiFS, *J. Geophys. Res.*, 103, C11, 24937.

Robinson, I.S. (2004): Measuring the Oceans from Space, Springer, New York.

Tanaka, A., M. Kishino, R. Doerffer, H. Schiller, T. Oishi and T. Kubota (2004): Development of a Neural Network Algorithm for Retrieving Concentrations of Chlorophyll, Suspended Matter and Yellow Substance from Radiance Data of the Ocean Color and Temperature Scanner, *J. Oceanogr.*, 60, 519-530.

Valiela, I. (1995): Marine Ecological Processes, Springer, New York.

Part II

Outline of the Training Course in 2006

Outline

As a part of the Japanese contribution to the International Hydrological Programme (IHP) of UNESCO, a short course for participants from the Asia-Pacific region is going to be conducted with a theme ***Oceanography Basics***, from 26 November to 9 December 2006, at the Hydrospheric Atmospheric Research Center (HyARC), Nagoya University, Nagoya, Japan. The course comprises a series of lectures and practice sessions in English. It also includes an overnight field observation cruise in Ise Bay on a training vessel Sei-Sui Maru of Mie University, and a technical tour to the Center for Marine Environmental Studies, Ehime University.

Objectives

The general aim of the 16th IHP short course is to help participants to develop their basic knowledge of oceanography. Being the largest reservoir of water and carbon dioxide on the earth surface, the oceans have profound influence on the water and material cycles in the earth system. A series of lectures are organized to show how land, oceans, and atmosphere are interacting, how water and materials cycles are coupled, what are the driving forces of materials cycling in the ocean, and what are the causes of its variation. Special emphasis will be placed on the coastal regions where the land-ocean interaction is most intense and moreover influence of human activities is most significant. We are expecting, through the lectures, to demonstrate that the ocean is highly dynamic in response to atmospheric forcing as well as land driven materials, and it is highly likely that the oceans in turn affect hydrological cycles on land surface. We hope the participants will acquire new view from this short course, as even local environmental problems, which relate to hydrological cycle change on a regional scale, are resulting from a part of global cycles of water and materials including oceans

Course Contents (convener: A. Morimoto)

Lecturers

Y. Fukushima (Research Institute for Humanity and Nature)
J. Ishizaka (Faculty of Fisheries, Nagasaki University)
A. Kaneda (Center for Marine Environmental Studies, Ehime University)
Y. Koizumi (Ehime Prefectural Fisheries Experimental Station)
A. Morimoto (Hydrospheric Atmospheric Research Center, Nagoya University)
T. Saino (Hydrospheric Atmospheric Research Center, Nagoya University)
K. Sasaoka (Japan Agency for Marine-Earth Science and Technology)
T. Suga (Graduate School of Science, Tohoku University)
H. Sugisaki (National Research Institute of Fisheries Science)
H. Takeoka (Center for Marine Environmental Studies, Ehime University)
Y. Tanimoto (Graduate School of Environmental Science, Hokkaido University)
S. Uye (Graduate School of Biosphere Science, Hiroshima University)
T. Yanagi (Research Institute for Applied Mechanics, Kyushu University)

List of Participants

1) UNESCO-IHP Participants

Ms. Subagio Widitya (Indonesia)

Affiliation: Agency For Marine And Fisheries Research

Address: Jl. Cipunegara I Blok A2 No. 11 Komplek Kejaksaan Agung R.I Ciputat - Tangerang, Indonesia 154311

Mr. Suwedi Nawa (Indonesia)

Affiliation: Center for Environmental Technology Institutio

Address: Tamansari Persada Blok G5-4 Bogor, 16166

Ms. Myint Thida (Myanmar)

Affiliation: Department of Meteorology and Hydrology

Address: Department of Meteorology and Hydrology, Mayangon, 11061, Kaba Aye Pagoda Road, Yangon, Myanmar

Mr. Tom Eric Kupu (PNG)

Affiliation: Department of Transport

Address: Department of Transport Enga Haus 2, 7Mile P.O.Box1489 Port Moresby, National Capital District, Papua New Guinea

Ms. Tanchuling Maria Antonia (Philippines)

Affiliation: Department of Civil Engineering, College of Engineering University of the Philippines

Address: 1 Comfrey Lane, Dreamhomes Subdivision, Pasig City, Metro Manila, Philippines

Mr. Dissanayake Konara M.D.B. (Srilanka)

Affiliation: Coast Conservation Department

Address: Coast Conservation Department 4th Floor, New Secretariat Building Maligawatte, Colombo 10, Sri lanka

Mr. Tran Hoang Tuan (Vietnam)

Affiliation: Institute of Meteorology and Hydrology in Vietnam.
Sub-Institute of Hydrometeorology and Environment in South of Vietnam

Address: 19th Nguyen Thi Minh Khai St., District 1. Ho Chi Minh City, Viet Nam.

2) Participants from Graduate School of Environmental Studies, Nagoya University

Mr. Vu Hai Dang (Vietnam)

Affiliation: Graduate School of Environmental Studies, Nagoya University, Japan

Address: Furo-cho, Chikusa-ku, Nagoya, Aichi 464-8601, Japan

Mr. Andreas Albertino Hutahaean (Indonesia)

Affiliation: Graduate School of Environmental Studies, Nagoya University, Japan

Address: Furo-cho, Chikusa-ku, Nagoya, Aichi 464-8601, Japan

Lectures

L0 Introduction ..... **A. Morimoto**
- Guidance and outline of this IHP short course

L1 Land and Oceans .....**Y. Fukushima**
- Water and Material cycles on land, and transport of materials to coastal seas
- Linkage of changes in land and oceans

L2 Oceans and Atmosphere .....**Y. Tanimoto**
- Heat balance of the earth system
- Energy exchange between ocean and atmosphere

L3 Ocean Circulation .....**T. Suga**
- Large scale ocean circulation
- Water mass formation in the Pacific Ocean

L4 Phytoplankton in the ocean ..... **J. Ishizaka**
- Production of food for marine life, and uptake of carbon dioxide in seawater
- Control mechanism and causes of variation

L5 Zooplankton in the ocean .....**S. Uye**
- Linking primary production to higher trophic levels
- Control mechanism and causes of variation

L6 Materials dynamics in the coastal seas .....**A. Morimoto**
- Advection, diffusion and dispersion of materials in coastal seas
- Interactions between coastal and open seas

L7 Biogeochemical cycles in the ocean .....**T. Saino**
- Carbon and nitrogen cycles in the ocean
- Biogeochemical cycles and climate system

L8 Changes in biogeochemical cycles in the ocean .....**H. Sugisaki**
- Long-term ecosystem change in the oceans
- Possible causes of ecosystem change

L9 Role of coastal seas in climate system .....**T. Yanagi**
- Material cycles in coastal seas,
- Possible feedback to climate system

Practices

P1 Field observation in Ise Bay .....Y. Sekine & A. Morimoto
- Transect observation of water temperature and salinity
- Analysis of chlorophyll a concentration

P2 Analysis of satellite ocean color data ..... K. Sasaoka
- Visualization of satellite remote sensing data
- Calibration of chlorophyll a concentration

Technical Tours

T1 Auto-Monitoring system of water quality in the Bungo Channel, Ehime University .....H. Takeoka & A. Kaneda

T2 Aquaculture and monitoring system in the Bungo channel, Ehime Prefectural Fisheries Experimental Station .....Y. Koizumi

Schedule (26 November – 9 December, 2006)

26 (Sunday) Nov., 2006	Arrival at Nagoya	Stay in Nagoya
27 (Monday)	Guidance (Lecture 0), Lectures 1, 2 & 3 Reception at Nagoya University	Stay in Nagoya
28 (Tuesday)	Lecture 4, 5 & 6	Stay in Nagoya
29 (Wednesday)	Lecture 7, 8 & 9	Stay in Nagoya
30 (Thursday)	Practice 1 (Move to Mie)	Ship
01 (Friday) Dec., 2006	Practice 1	Ship
02 (Saturday)	Practice 1 (Move to Nagoya)	Stay in Nagoya
03 (Sunday)	Japanese Culture Introduction and Free Time (Move to Ehime)	Stay in Ehime
04 (Monday)	Technical Tour 1	Stay in Ehime
05 (Tuesday)	Technical Tour 2	Stay in Ehime
06 (Wednesday)	Practice 2 (Move to Nagoya)	Stay in Nagoya
07 (Thursday)	Practice 2, Report	Stay in Nagoya
08 (Friday)	Closing Ceremony	Stay in Nagoya
09 (Saturday)	Departure from Nagoya Airport	

ISBN: 4-9980619-6-8